Università degli Studi di Padova

Dipartimento di Fisica

SCUOLA DI DOTTORATO DI RICERCA IN FISICA

CICLO XXV

Nuclear structure evolution far from stability: study of ^{74}Ni collectivity by Coulomb excitation

Direttore della Scuola: Ch.mo Prof. Andrea Vitturi

Supervisori: Prof.ssa G. Montagnoli

Dott.ssa F. Gramegna

Dott. G. De Angelis

Dottorando: Tommaso Marchi

Abstract

In recent years the availability of neutron-rich radioactive ion beams has allowed to explore new regions of the nuclear chart. Despite the most exotic nuclei have been produced with quite low intensities, new interesting results have revealed an evolution of the nuclear structure far from the valley of β stability. Some of the well established fundamental properties of the nuclear models, like the magic numbers, had to be reviewed in the light of new experimental observations: new features have been included in nuclear models in order to reproduce experimental data. It was recently shown, indeed, that tensor and three-body forces play an important role in breaking and creating magic numbers.

One region of particular interest is the neutron-rich tail of the Ni isotopic chain. For instance the ^{78}Ni nucleus corresponds to a double shell closure and is characterized by a large neutron excess. Some models predict that at this N/Z ratio one could expect an increase of the proton-neutron interaction strength that would modify the relative energies of the single particle states, thus reducing the $Z = 28$ energy gap. In such a scenario, particle-hole excitations should be strongly increased, driving to enhanced collectivity. The determination of the $B(E2)$ values of the low-lying transitions is therefore very important to measure these features and to constrain the interaction used for the shell model calculations.

In this thesis we present the measurement of the $B(E2; 0^+ \rightarrow 2^+)$ transition matrix element for the first 2^+ state of the ^{74}Ni nucleus.

This was done in an intermediate-energy Coulomb excitation experiment performed at NSCL (MSU) where the Coulomb excitation cross section $\sigma_{0^+ \rightarrow 2^+}$ was measured, allowing to extract the $B(E2 \uparrow)$ value. To date, ^{74}Ni is the most exotic Ni isotope produced with enough intensity to be used as a beam for spectroscopic studies. The ^{74}Ni beam has been produced by fragmentation of a primary ^{86}Kr beam at 140 AMeV

on a ^{9}Be target. The primary beam was provided by the Coupled Cyclotron Facility of the NSCL and the production reaction fragments were analyzed using the A1900 fragment separator. As a matter of fact, this setup produced a secondary "cocktail-beam" containing ^{74}Ni ions with an intensity of $\approx$ 1 pps as well as higher intensity ^{77}Zn and ^{75}Cu fragments. An ^{197}Au foil was used as secondary target. The scattered ions were identified by the focal plane detectors of the S800 spectrograph and coincidence γ-rays emitted by Coulomb excited ions were detected by the 4π CAESAR array.

The results emerging from the data analysis show a different behavior with respect to the expectations. This finding opens new scenarios in the interpretation of the shell evolution of the Z=28 isotopes.

The thesis has been organized as follows: the basic concepts concerning Nuclear Structure studies far from stability and the radioactive ion beams production are introduced in chapter 1. In chapter 2 the fundamental theoretical models of Coulomb excitation are presented. In chapters 3 and 4 are respectively described the experimental setup and the data analysis of the Coulomb excitation experiment. The final results are discussed in the last section. Considerations on possible interpretation of Ni shell evolution will be presented together with some outlooks.

Riassunto

Negli ultimi anni lo sviluppo di infrastrutture per la produzione di fasci di nuclei instabili (radioattivi) ha permesso di esplorare nuove regioni della carta dei nuclidi, lontano dalla valle di stabilità. Nonostante le tecnologie attuali non permettano di produrre fasci esotici di intensità paragonabili a quelle dei fasci stabili, varie informazioni sulla struttura nucleare lontano dalla valle di stabilità sono già state ottenute. Si è osservato, ad esempio, che proprietà ben assodate come la chiusura di shell in corrispondenza di determinati numeri magici e l'ordinamento delle shell previsto dai modelli tradizionali, non sono più valide in presenza di una forte asimemtria di isospin. La formazione di aloni neutronici e la comparsa di nuovi numeri magici a discapito di quelli tradizionali sono due esempi del nuovo panorama che sta emergendo. Quando ci si allontana dalle regioni per le quali sono stati sviluppati ed ottimizzati, i modelli tradizionali non riescono più a descrivere in maniera appropriata la struttura nucleare. In questo contesto si rendono necessari termini correttivi tra i quali le interazioni di tipo tensoriale e le forze a tre corpi si sono dimostrate di particolare efficacia.
Una regione interessante è rappresentata dalla parte ricca di neutroni della catena isotopica del Nichel, in particolare nelle vicinanze del ^{78}Ni. Secondo lo sviluppo tradizionale delle shell nucleari, questo nucleo presenta una doppia chisura di shell (Z=28, N=50). Tuttavia, alcuni nuovi modelli prevedono che con questo rapporto N/Z ci si debba attendere un incremento dell'interazione neutrone-protone tale da modificare le energie relative dei livelli di particella singola, riducendo il gap della shell protonica. In questa situazione le eccitazioni particella-buco dovrebbero essere maggiormente favorite e presentare un comportamento fortemente collettivo. L'andamento degli elementi di matrice ridotti ($B(E2)$) delle transizioni dei livelli eccitati più bassi di questi nuclei rappresenta uno degli indicatori più importanti per validare le ipotesi fatte e fornire informazioni quantitative per lo sviluppo di modelli

nucleari appropriati.
In questo lavoro di tesi verrà descritto l'esperimento per la misura della $B(E2; 0^+ \rightarrow 2^+)$ del primo livello eccitato (2^+) del nucleo ^{74}Ni tramite la misura della sezione d'urto di eccitazione coulombiana ad energie intermedie. Tale nucleo risulta, ad oggi, l'isotopo del Nichel più esotico ad essere stato prodotto con intensità di fascio sufficienti da consentire studi di tipo spettroscopico. L'esperimento è stato realizzato presso il *National Superconducting Cyclotron Laboratory* (NSCL) della Michigan State University. Il fascio di ^{74}Ni è stato prodotto per frammentazione di un fascio primario (stabile) di ^{86}Kr accelerato dalla *Coupled Cyclotron Facility* ad un'energia di 140 AMeV e diretto su un bersaglio di ^{9}Be. Qui, principalmente in seguito a reazioni di frammentazione del proiettile, sono state prodotte numerose specie nucleari. La selezione degli isotopi di interesse, realizzata dal separatore elettromagnetico A1900, ha consentito di isolare un fascio secondario ("cocktail-beam") contenente ioni di ^{74}Ni con un'intensità di circa 1 pps assieme ai più intensi fasci di ^{77}Zn e ^{75}Cu. Per l'eccitazione culombiana è stato usato un foglio di ^{197}Au spesso 640 mg/cm^2. Gli ioni in uscita dal bersaglio secondario sono stati identificati dai rivelatori di piano focale dello spettrometro S800 ed i fotoni di diseccitazione emessi in coincidenza sono stati misurati utilizzando il rivelatore a 4π CAESAR.
Dall'analisi dei dati realizzata in questo lavoro è emerso che, entro gli errori sperimentali, il valore della B(E2) è diverso da quanto osservato precedentemente utilizzando tecniche differenti. Questo risultato potrebbe pertanto aprire la strada a nuove interpetazioni sull'evoluzione delle shell all'interno della catena isotopica del Ni. Questo elaborato è organizzato nel modo seguente: nel primo capitolo verranno introdotti i concetti principali riguardanti lo studio della struttura nucleare lontano dalla valle di stabilità e la produzione di fasci radioattivi. Nel capitolo 2 verrano illustrati gli aspetti fondamentali della teoria dell'eccitazione culombiana in diversi regimi energetici. I capitoli 3 e 4 saranno dedicati, rispettivamente, alla descrizione dell'apparato e dell'analisi dei dati. I risultati ottenuti verranno infine commentati nell'ultima sezione. Verranno quindi discusse alcune possibili interpretazioni sull'evoluzione della struttura nucleare nella catena isotopica del Nichel e presentate le prospettive sperimentali necessarie per una migliore comprensione della tematica discussa.

Contents

1

Nuclear Structure studies with radioactive ion beams

The development of new instrumentation and acceleration techniques has always been crucial for nuclear structure studies. Whenever new experimental tools for accelerating and detecting particles and nuclear radiation have been developed, new and quite often unexpected features have shown up.

In particular, the development of techniques to produce and accelerate unstable nuclei (the so-called *Radioactive Ion Beams*) opens up new possibilities to access and study nuclei with large neutron excess (*neutron-rich nuclei*). This is one of the "hot" topics of contemporary Nuclear Structure studies because it allows to explore regions of the nuclear chart that are not commonly accessible. Beyond the possibility of discovering new isotopes, researchers have the opportunity to test the validity of nuclear structure and nuclear reaction models while moving far from the conditions where they have been developed and tested. New scenarios arose in recent years thanks to the availability of radioactive beams with increasing neutron/proton ratio. For instance, the rearrangement of the nuclear shells and the related appearance of

new magic numbers shows that the global features of the nuclear force change while increasing the number of neutrons in the nuclear system.
In this chapter, some of the current topics in Nuclear Structure will be reviewed. We will describe how the availability of radioactive ion beams allows to probe the behavior of nuclear shells far from the stability line and which are the current limits in the study of very neutron-rich nuclei. Particular care will be put on the structure of the Ni isotopic chain. The nuclear shell evolution in the region close to the doubly magic ^{78}Ni will be described in order to better understand the relevance of the measurement of the reduced matrix element $B(E2)\uparrow$ of the ^{74}Ni isotope, which is the main subject of the present Thesis.

1.1 The Nuclear Chart, a wide landscape

"Atomic nuclei comprise 99.9% of all baryonic matter in the Universe and are the fuel that burns in stars. The rather complex nature of the nuclear forces among protons and neutrons generates a broad range and diversity in the nuclear phenomena that can be observed" [1]. The atomic nucleus is indeed a quantum-mechanical system where a number of Z protons and of N neutrons (the *nucleons*) are held bound by the strong force. The proton carries electric charge while the neutron does not. For this reason, protons in nuclei also feel their mutual Coulomb repulsion. To obtain a bound system the two forces have to counterbalance. The net result is a system with a degree of complexity that increases with the number of nucleons $A = N + Z$ (i.e. the nuclear mass). There are many combinations of neutrons and protons which can form a nucleus of a given mass. The wide landscape of nuclei offered by Nature is usually summarized in the so-called *Nuclear Chart* shown in figure 1.1.

To date, around 3000 nuclei have been observed. About 250 nuclides, corresponding to the black squares of figure 1.1, are stable and can be found naturally. The remaining observed nuclei, corresponding to the yellow boxes of figure 1.1, are unstable and they ultimately convert to a stable isotope via a chain of radioactive decays, the lifetimes of which might range from nanoseconds to millions of years. Most of the observed unstable nuclei have been artificially produced in a laboratory, though some of them can be found in Nature as part of the decay chain of extremely long-lived isotopes. Theoretical models predict the existence of more than 6000 nuclear

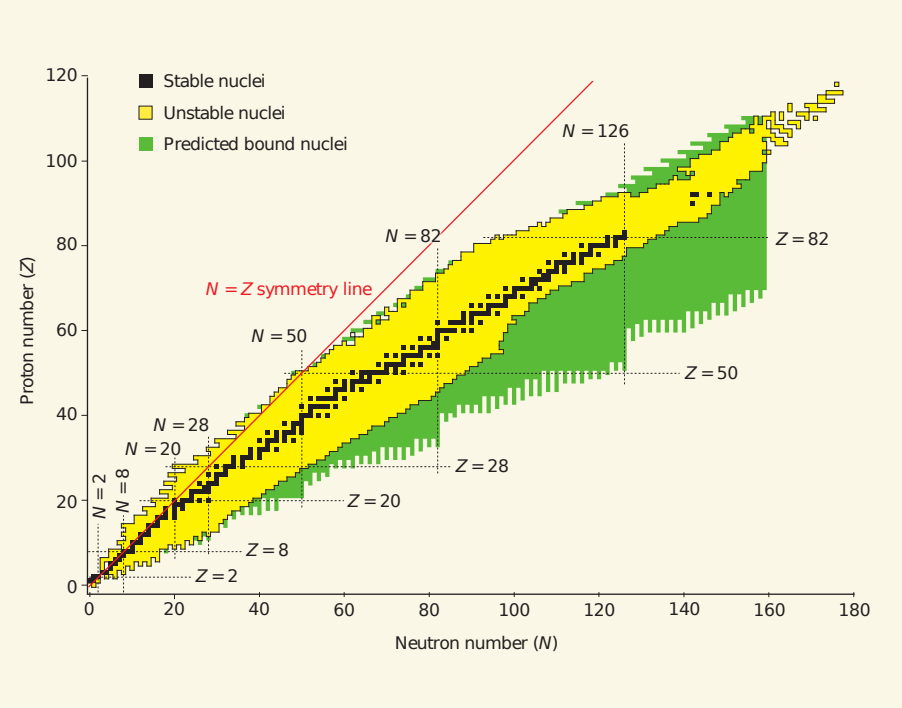

Figure 1.1: Nuclear Chart. Colors are used to group nuclei according to the type of decay. Black dots represent stable nuclei accumulating along the valley of nuclear stability. The yellow area corresponds to experimentally observed unstable isotopes while the green area shows unstable nuclei which are predicted to be bound but which have not yet been observed. Adapted from [2].

bound systems (the green squares of figure 1.1), meaning that only half of the global panorama has been explored to date.

More generally speaking, the limits of nuclear stability provide a key benchmark of nuclear models. These limits also highlight the emergence of new phenomena leading to extra binding and to an extension of the expected limits of stability, as it has been discovered for halo nuclei [3]. The boundary limits for extremely neutron-deficient nuclei and the location of the proton drip-line are fairly well defined, but very little is known about the limits of binding of very neutron-rich nuclei and the location of the neutron drip-line, which are established experimentally only for the eight lightest elements [4]. The neutron deficient part of the nuclear chart can be accessed experimentally using fusion evaporation reactions. On the contrary, in order to study the neutron-rich side of the nuclear chart, new tools should be developed such as the production of beams of (unstable) neutron-rich nuclides, namely the *radioactive ion beams*. Those beams will provide experimental access to the nuclear properties

of heavy neutron-rich nuclei that will drive the development of nuclear models with greatly improved predictive power. Indeed, there is a broad agreement in the nuclear-science community that the critical path to improvements in nuclear modeling passes through neutron-rich nuclei far from the line of β-stability. Their properties must be known to determine the actual degrees of freedom and to constrain the effective interactions such as the tensor force [5], the symmetry energy [6], and the isospin dependent three-body forces [7] which are, so far, only poorly determined.
From the theoretical point of view, even assuming a very simple parametrization of the nuclear potential, the solution of the quantum-mechanical many body problem becomes almost impossible already at very low mass numbers. Modern *ab-initio* calculations use a realistic expression of the nucleon nucleon interaction to calculate nuclear properties in computational frameworks like Green's function Monte Carlo, no-core shell model or coupled cluster method. They are successful when the nuclear mass is small (i.e. up to $A = 8$ or so) but, when the number of nucleons increases, computational times diverge. For this reason, several macroscopic approaches are used for medium-mass or heavier nuclei where the great success of the shell model is evident. In this field, modern configuration interaction techniques are used. For very heavy nuclei, the density functional theory based on self-consistent/mean field approaches is the tool of choice. By investigating the intersections between these theoretical strategies, theorists aims at developing a unified description of the nucleus. Figure 1.2 shows how theoretical models match the nuclear chart and how different approaches overlap in boundary regions.
In this work we will focus on the neutron-rich side of the Ni isotopic chain, that is studied with details from the theoretical point of view using mean field and shell model calculations. We will introduce in the next paragraph some interesting phenomena that arise while moving far from the stability line, increasing the number of neutrons in the nucleus.

1.1.1 Nuclear shells far from stability

Ideally, as mentioned in section 1.1, one could think of deriving the nuclear properties starting from a more or less detailed knowledge of the nucleon-nucleon interaction (the so-called *ab-initio* approach). As already mentioned in the previous paragraph, the solution of the quantum-mechanical many body problem becomes almost impos-

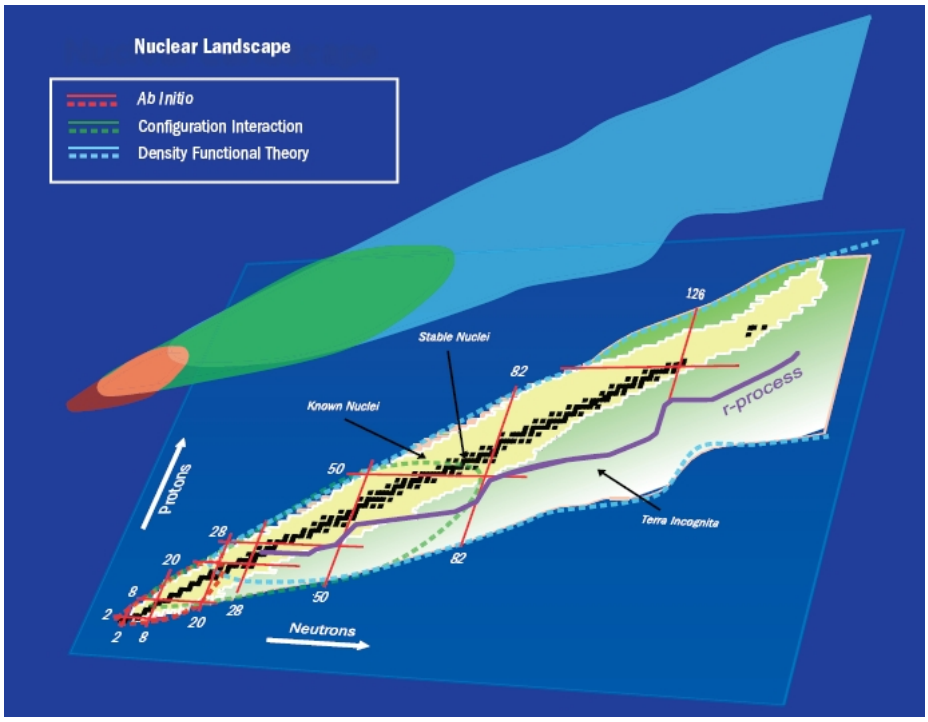

Figure 1.2: Theoretical approaches used in the various regions of the chart of nuclides. In the low-mass region ab-initio calculations are possible. Moving to higher masses, extended shell model approaches (here stated as *configuration interaction*) are widely exploited. For the heaviest part of the diagram only mean field calculations can be used (i.e. *density functional theories*). Adapted from [8].

sible already at very low mass numbers. For larger masses, presently up to $A \approx 80$, the complementary approach of the Nuclear Shell Model is highly successful. The Nuclear Shell Model is indeed one of the earliest models developed to describe the properties of the known nuclides and, incidentally, it is one of the most successful models developed so far. It relies ultimately on the concept of single-particle motion in an average mean field. This can be explained considering the nuclear hamiltonian:

$$H = \sum_{i=1}^{A} \left[\frac{\mathbf{p}_i^2}{2\ m_i} \right] + \sum_{i,k}^{A} V_{ik}(\mathbf{r}_i - \mathbf{r}_k). \tag{1.1}$$

Here A is the number of nucleons, the first term is their kinetic energy and the second one is the two-body interaction potential. For the moment, third or higher orders interaction terms are neglected. In the mean-field hypothesis, one assumes the existence of a single-particle potential $V(\mathbf{r})$ that absorbs most of the $V_{ik}(\mathbf{r}_i - \mathbf{r}_k)$

potential. In other words, one assumes that each nucleon moves independently from the others in a potential generated by the other nucleons themselves. This results in the separation of the hamiltonian in two components:

$$H_i = \sum_{i=1}^{A} \left[\frac{\mathbf{p}_i^2}{2\ m_i} \right] + \sum_{i=1}^{A} V_i. \tag{1.2}$$

$$H_{i,k}^{res} = \sum_{i,k}^{A} V_{ik} - \sum_{i=1}^{A} V_i. \tag{1.3}$$

where

$$H = H_i + H_{i,k}^{res}. \tag{1.4}$$

The H_i part is the one describing the motion of the nucleon in the nucleus (also called the *single-particle* hamiltonian), while $H_{i,k}^{res}$ is the residual interaction between nucleons that is not considered by the mean-field. This component has to be small compared to the single-particle one. Under these assumptions, a shell structure, similar to the atomic shell structure appears in a quite natural way. The mean potential can be described, to a good approximation, in terms of the so called Wood-Saxon potential. This is specified by the parameters depth (V_0), radius (R_0) and diffuseness (a):

$$V(r) = -\frac{V_0}{1 + \exp\frac{r - R_0}{a}}. \tag{1.5}$$

The eigenstates of this potential can be obtained only numerically, thus the Harmonic Oscillator potential is often used as a convenient approximation since it can be treated analytically. The expression of this potential is:

$$V_i = \frac{1}{2} m_i \omega^2 r_i^2 \tag{1.6}$$

where m_i is the mass of the i^{th} nucleon, ω is the oscillator frequency and r stands for the distance from the center of the nucleus. The eigenvalues of the harmonic oscillator are shown in the left part of figure 1.3 and are evenly spaced in energy. Since the early studies of Mayer [9] and Jensen [10] in 1949, it has been clear that this simple model does not reproduce well the observed behavior of nuclear shell gaps.

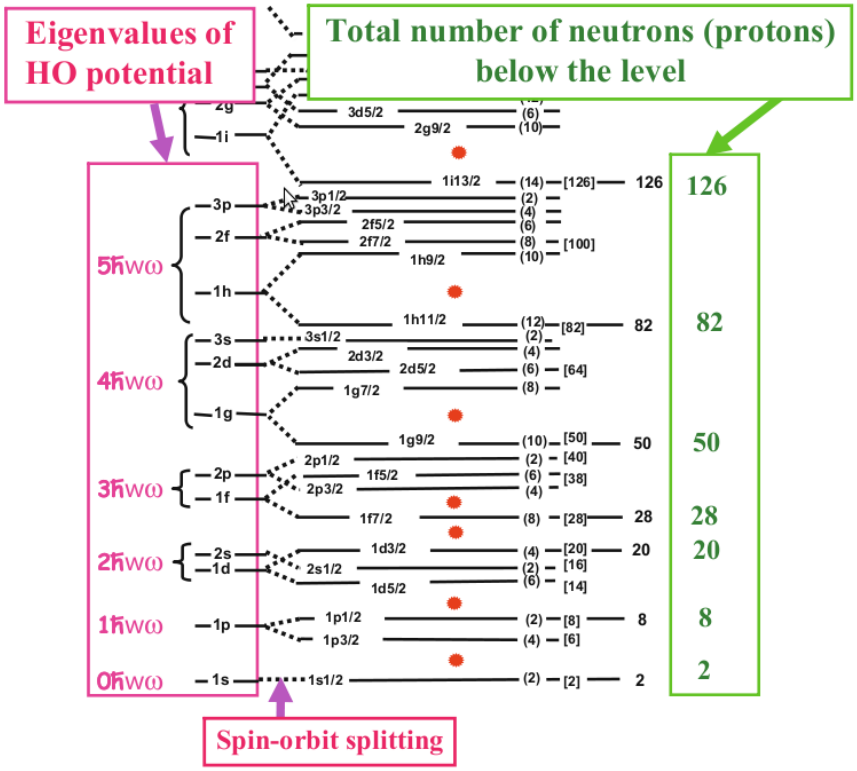

Figure 1.3: Energy eigenvalues of the harmonic oscillator with and without the spin-orbit splitting. The right panel shows the magic numbers introduced by Mayer and Jensen. Adapted from [11].

Indeed, the *orbitals* which nucleons can occupy, are not evenly spaced and the orbitals corresponding to a given principal quantum number (N) of the harmonic oscillator are degenerate in energy. Thus one can identify groups of levels (*shells*) with "large" separation between the groups. This explains why some nuclides, corresponding to the cases in which the major shells are filled, are particularly stable, as pointed out by the early experimental findings. In order to reproduce all of the observed *magic numbers*, however, it is necessary to take a further spin-orbit term into account, describing the interaction between the spin of the nucleon and its orbital angular momentum:

$$V_{ls}(\vec{r}) = f(\vec{r})(\vec{l} \cdot \vec{s}) \tag{1.7}$$

This was done in the independent works of Mayer and Jensen who added a spin orbit coupling term to the Harmonic Oscillator potential, succeeding in the interpre-

tation of the experimental data available at that time. This calculation leads to the splitting of the single particle levels that re-arrange in terms of energy as shown in figure 1.3.

From the above description, it should be clear that the location and size of shell gaps depend on the specific details of the mean field and the residual interaction between the valence nucleons considered. It is worth to underline that most of the nuclear models have been developed and tested with the available data about nuclei very close to stability. Therefore, the "traditional" magic numbers discovered for stable nuclei and the shells ordering should not be expected to remain the same throughout the whole chart of nuclides. The question of the shell evolution moving towards the neutron-rich regions is indeed one of the most actual topics of modern Nuclear Structure. Extrapolating towards exotic nuclei the models developed and tested for the isotopes near the stability line is a quite delicate question.

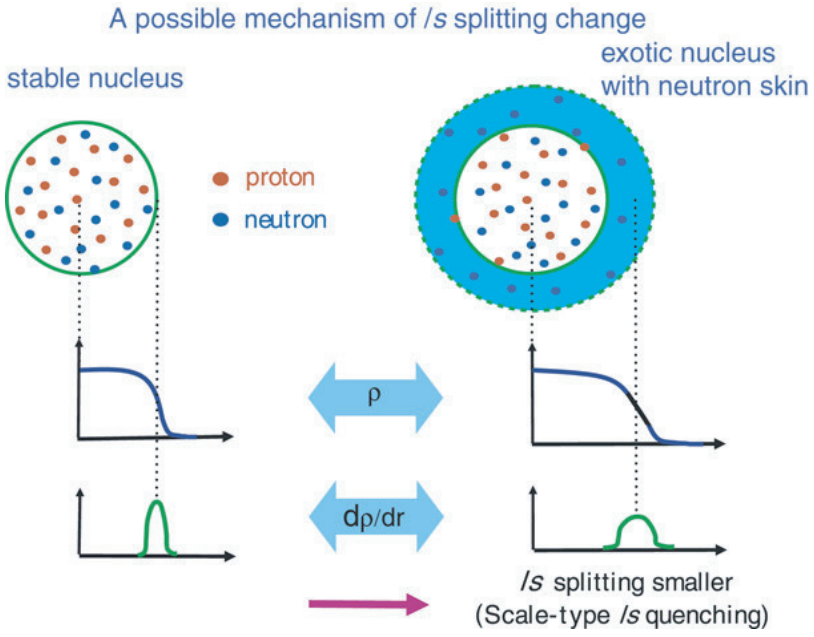

Figure 1.4: Scale-type *ls* quenching. In neutron-rich nuclei the spin-orbit force should be weaker as a consequence of the diffuseness of nuclear surface. [12]

Scale-type ls quenching

The availability of the very first generation of radioactive ion beams already triggered the development of many theoretical schemes, trying to explain some of the newly observed features and to develop some more general frameworks. One of these is the so-called *scale-type ls quenching* [13]. Since the spin-orbit force is proportional to the radial derivative of the potential, its strength may be weakened with a diffuse surface region (see figure 1.4) where the neutron excess causes a softer decrease of the nuclear density (or neutron *skin*) [13]. Thus, the magic numbers identified near stability could change for neutron-rich nuclei (fig. 1.5) revealing a more harmonic-oscillator like behavior. Some calculations indicate that, near the neutron drip line, one may encounter quenching of existing shell gaps leading to the emergence of new magic numbers. It is clear that these effects have to be expected very close to the neutron drip-line, where the appearance of a neutron skin becomes an appreciable phenomenon. As it can be seen in the nuclear chart (fig. 1.1), the neutron drip-line is experimentally accessible only for the lightest elements and it is increasingly far from the most exotic isotope observed as one moves towards heavier nuclei. For this reason scale-type ls quenching cannot be considered the only reason of the observed evolution of the nuclear shells.

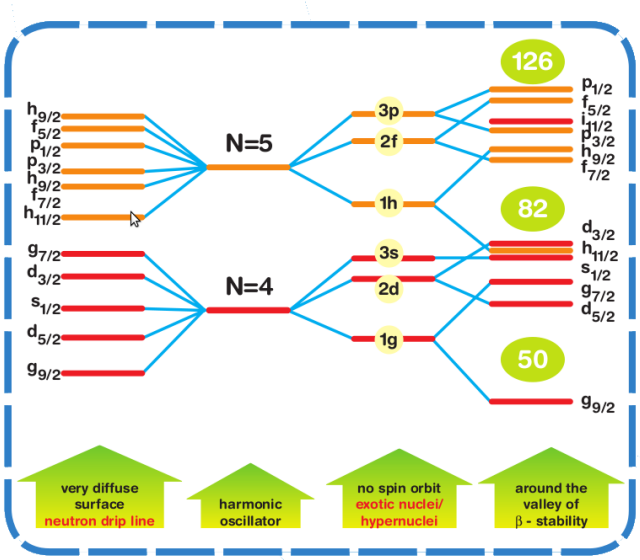

Figure 1.5: Possible evolution of the nuclear shells due to surface diffuseness moving towards the neutron drip-line. Adapted from [14].

The tensor force

T. Otsuka and co-workers recently pointed out the importance of the tensor force component in the parametrization of the nuclear potential [15, 16]. As introduced by Yukawa in 1938, the nucleon-nucleon interaction can be explained in terms of meson exchange. In this framework, the $\pi + \rho$ meson exchange term is essentially the tensor force that can be parametrized in the mean field approach considering a potential term like [17]:

$$V_T = (\vec{\tau}_1 \cdot \vec{\tau}_1)\ S_{12}\ V(r) \tag{1.8}$$

where $\vec{\tau}_{1,2}$ denotes the isospin of the nucleons 1 and 2, $V(r)$ is a function of the relative distance of the nucleons (r) and S_{12} denotes the spin coupling, as explained with details in reference [18].

As shown in figure 1.6, this neutron-proton interaction has the effect to change the single particle energies as a function of the N/Z ratio. For instance, if $j_> = l+1/2$ and $j_< = l-1/2$, neutrons in $j'_>$ orbit lower the proton orbit with $j_<$ but raise the proton orbit $j_>$. Using this parametrization, it was shown that this term affects the shell structure in a robust way when considering exotic nuclei. A schematic overview of the possible effects was obtained in the work of Otsuka and collaboratos [5], which was focused on the evolution of the proton and neutron single particle energies calculated adding the tensor term into a Gogny-type mean field calculation (called GT2). More recently [16] the results obtained by successful shell-model effective interactions like GXPF1 [19] have been compared to what can be described using the tensor force added to a Gaussian central potential. Given the good agreement with the existing theories, the *monopole based universal interaction* (V_{MU}) was introduced. As shown in figure 1.7 (left panel), this potential consists of two terms: the first term is a Gaussian central force representing the bulk nuclear properties and re-normalized to experimental observations, while the second one is due to the tensor force. Using this parametrization, the shell evolution of neutron and protons single particle energies has been studied. Some results for the Ni isotopic chain are shown in the right panel of figure 1.7.

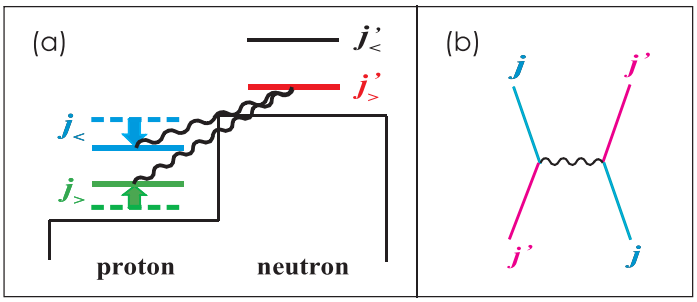

Figure 1.6: Panel (a) is a schematic picture of the monopole interaction produced by the tensor force between a proton in $j_{>,<} = l \pm 1/2$ and a neutron in $j'_{>,<} = l' \pm 1/2$. Panel (b) shows the exchange processes contributing to the monopole interaction of the tensor force. Adapted from [17].

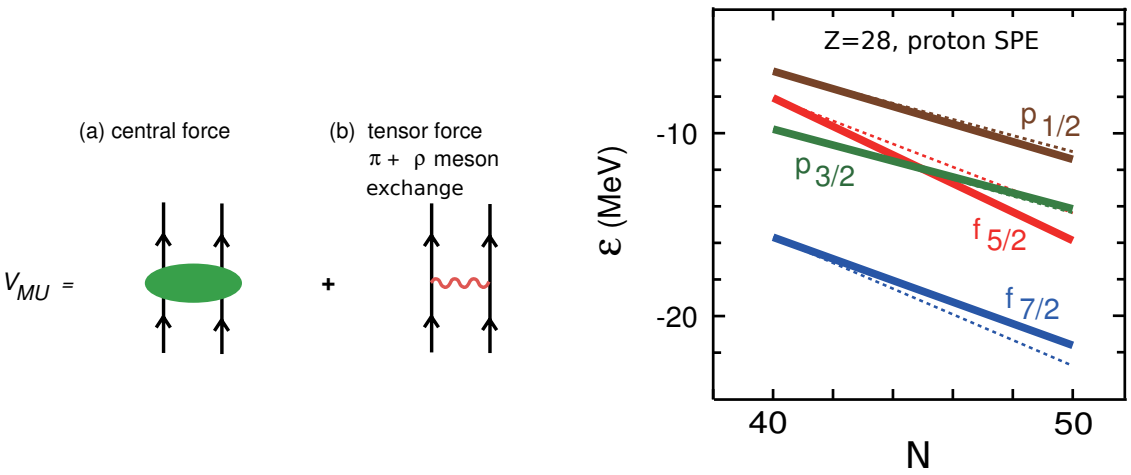

Figure 1.7: Left panel. Diagrams for the V_{MU} interaction. a) Central force comprehensive of experimental renormalization. b) Tensor force term (the same as 1.6 b). **Right panel**. Single particle energies for the Ni isotopes as calculated by V_{MU}. The attraction between $f_{7/2}$ and $f_{5/2}$ causes the inversion of the $p_{3/2}$ shell and the $f_{5/2}$ itself. Adapted from [16].

Three body forces

Another topic under discussion, needed to explain the properties of the nuclear potential far from stability is the inclusion of three-body forces. For instance, these mechanisms are used to explain the behavior of the neutron drip-line in regions where standard shell-model calculations fail. This is the case of the Oxygen isotopes reported in [20], where experimental observations underlined that the neutron drip-line of oxygen is closer to the stability line as compared to the basic trend. Moreover, adding only one proton (the fluorine case), the drip-line is back to the trend. Oxygen isotopes can be described as a multi-neutron system on top of the ^{16}O core (closed shell). Their experimental ground-state energies are shown in figure 1.8. One can calculate the interaction between these valence neutrons in the *sd* shell by microscopic methods. Some examples are are shown in figure 1.8. One finds that, without the inclusion of the three body terms, the ground-state energy keeps going down all the way to $N = 20$. This contradicts the experimental fact that the drip-line is at $N = 16$. The problem is overcome considering the repulsive contributions to the interactions among excess neutrons, namely the three body interaction.
The importance of this mechanism is also evidenced in the work of Hagen and collaborators [21] who succeeded in performing approximate ab-initio calculation employing interactions from chiral effective field theory. The binding energies and low-lying excitations of Calcium isotopes have been computed using the coupled-cluster method and it was shown (figure 1.9) that the phenomenological inclusion of three body forces plays an essential role when comparing to experimental data.

1.1.2 Experimental probes

Some consequences of these theoretical predictions on the shell evolution have been pointed out. A change in the magic numbers is expected [22] (see figure 1.10) and indeed new ones have been discovered in the recent years (e.g. $N = 16$, $N = 32$) whereas well established ones might disappear(e.g. $N = 20$, $Z = 14$). In looking for new (sub)shell closures the most sensitive and direct signature can be derived from

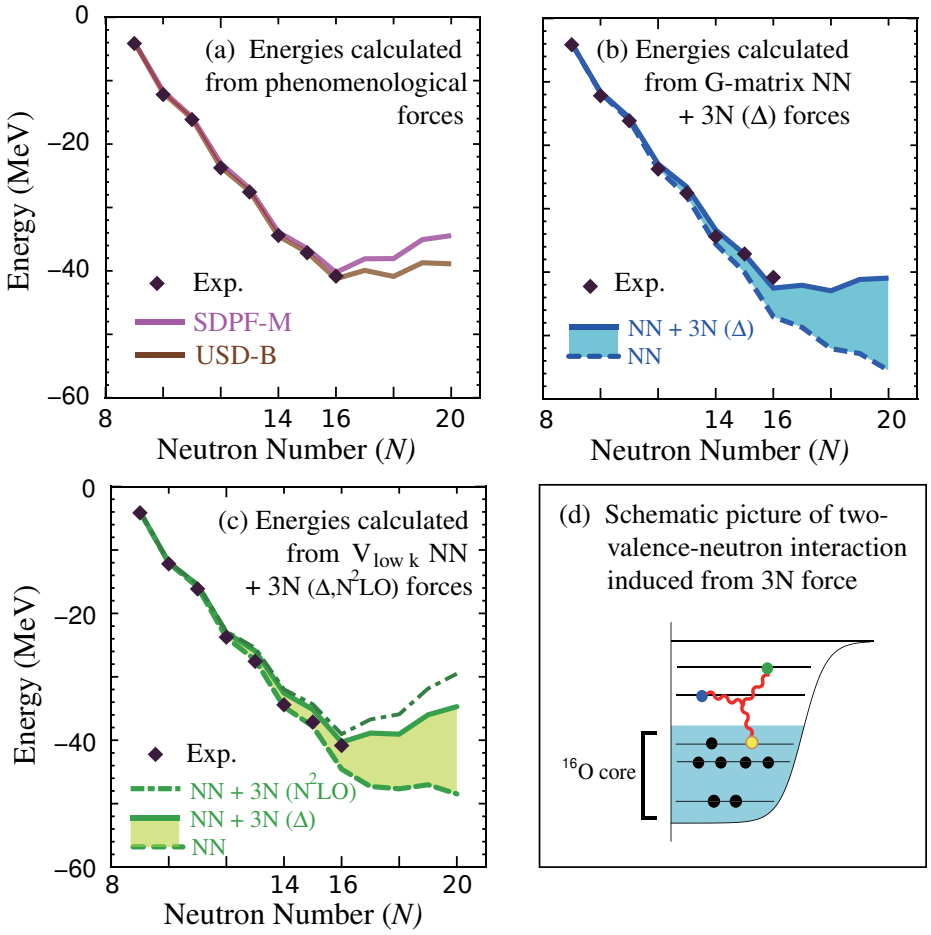

Figure 1.8: Experimental ground-state energies of the Oxygen isotopes measured from ^{16}O, including experimental values of the bound $^{16-24}$O compared to energies obtained from (a) phenomenological forces, (b) a G matrix formalism including three body forces, (c) low-momentum interactions $V_{low\ k}$ and including three body forces. (d) Schematic illustration of a two-valence-neutron interaction generated by three body forces with a nucleon in the ^{16}O core. Figure adapted from [20], see reference for details.

binding energies. The second differences:

$$\begin{aligned} \delta_{2n}(Z,N) &= S_{2n}(Z,N+2) - S_{2n}(Z,N) \\ \delta_{2p}(Z,N) &= S_{2p}(Z+2,N) - S_{2p}(Z,N) \end{aligned} \tag{1.9}$$

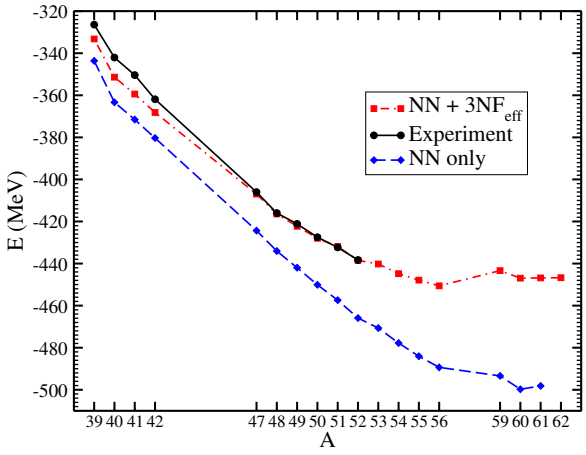

Figure 1.9: Ground-state energy of the Calcium isotopes as a function of the mass number A as calculated using the coupled cluster method. Black circles: experimental data; red squares: theoretical results including the effects of three-nucleon forces; blue diamonds: predictions from chiral NN forces alone. Figure adapted from [21].

where

$$\begin{aligned} S_{2n}(Z,N) &= BE(Z,N) - BE(Z,N-2) \\ S_{2p}(Z,N) &= BE(Z,N) - BE(Z-2,N) \end{aligned} \tag{1.10}$$

show a distinct peak for closed-shell nuclei and its height represents the shell gap. However, a basic change of the underlying nuclear structure, as, e.g., quadrupole correlations, can severely distort δ, since the binding energies of three nuclei are involved in equation 1.9. Similar indications about the underlying shell structure are given by the one-nucleon (proton or neutron) separation energies or by the difference between the same value in two consecutive nuclei as shown in figure 1.11.

More indirect measures for shell closures are the excitation energies of the first excited 2^+ states, $E(2^+)$ and the reduced transition strength, B(E2;$2^+ \rightarrow 0^+$). The particular stability of magic and doubly magic nuclei is expected to result in high excitation values for the first excited state ($E(2^+)$). Concerning the B(E2) values, transitions in nuclei close to a shell closure are mostly due to the contribution of a single particle, therefore these nuclei are expected to have low reduced transition

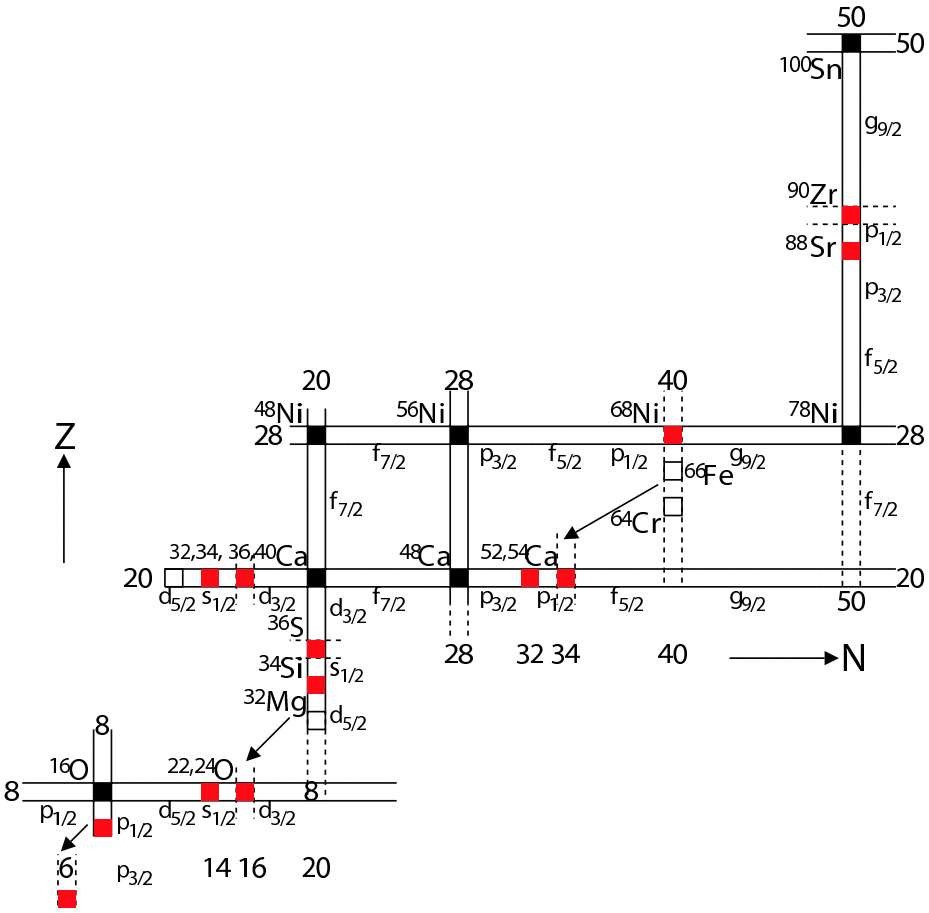

Figure 1.10: Schematic chart of known and expected new shell structure in $N \gg Z$ nuclei. Known and new closed shell nuclei are indicated respectively as full and hatched squares [22].

probabilities, close to the single particle estimate (see 2.1). In the opposite situation, at mid-shell, several particles can contribute coherently to the transition, resulting in high B(E2) values. This is what is typically described as a "collective" behavior. For instance, in figures 1.12 and 1.13 [24, 25] the $\delta_{2n/2p}$, B(E2) (in Weisskopf units) and $E(2^+)$ are shown for the closed shells $Z = 8$, $Z = 20$ and $Z = 28$. To demonstrate the isospin symmetry and to integrate the scarce data, the mirror nuclei with $N = 8,\ 20,\ 28$ are overlapped. The known magic nuclei, such as ^{16}O and ^{40}Ca, clearly stand out in these plots, and evidence for semimagicity of others, e.g. ^{34}Si, can be found. In recent years these studies have been pursued in several facilities, both using stable and unstable beams. For instance, one such campaign of experiments has been

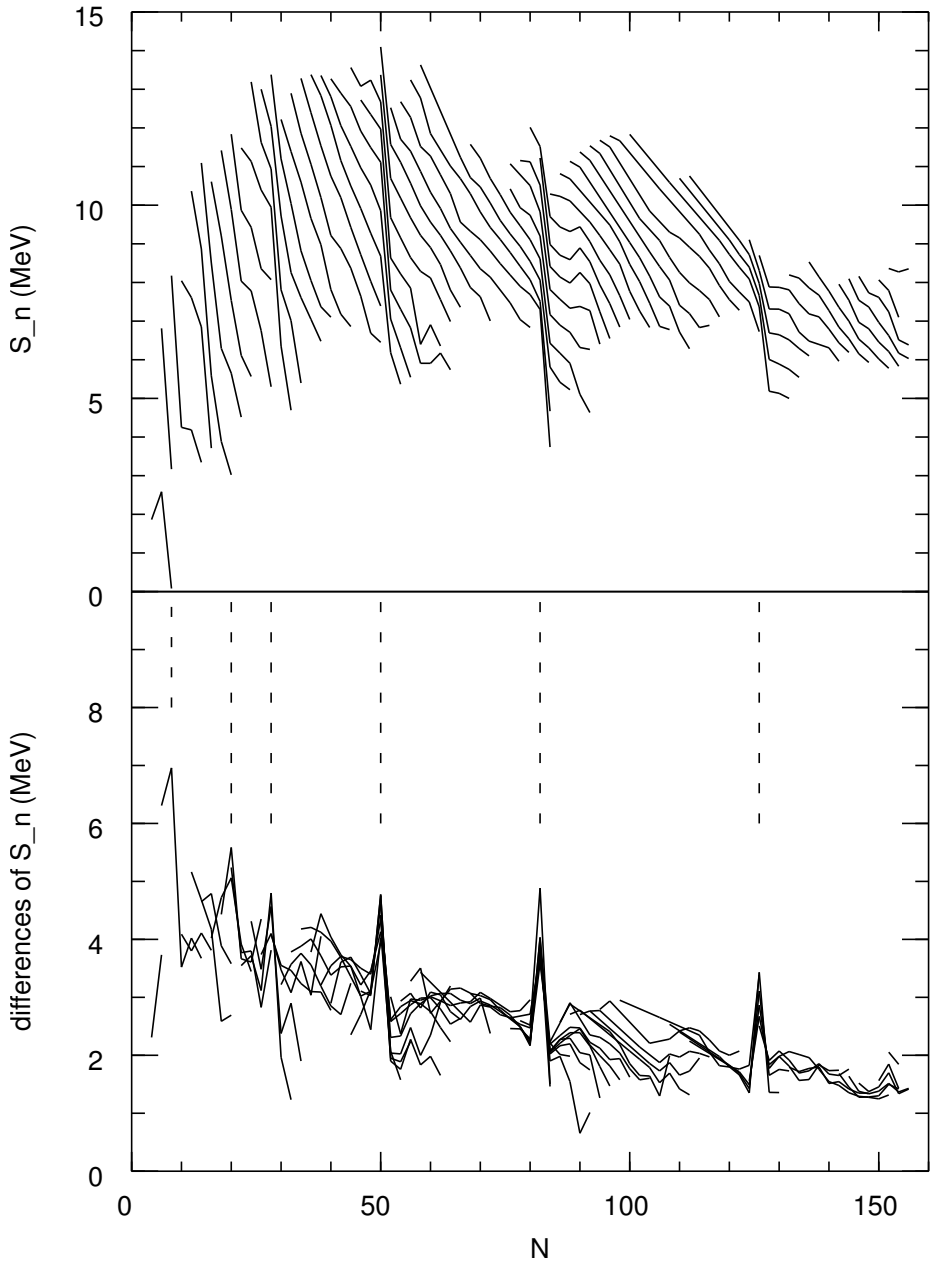

Figure 1.11: Top panel: one-neutron separation energies as a function of neutron number for even-even nuclei with N > Z. The lines connect nuclei with the same Z value. Bottom panel: difference between one-neutron separation energy for the same set of even-even nuclei. The dashed lines show the magic numbers 8, 20, 28, 50, 82 and 126. Adapted from [23].

carried out at the Laboratori Nazionali di Legnaro using the CLARA array of Clover detectors [26] in coupled operation with the PRISMA magnetic spectrometer [27].

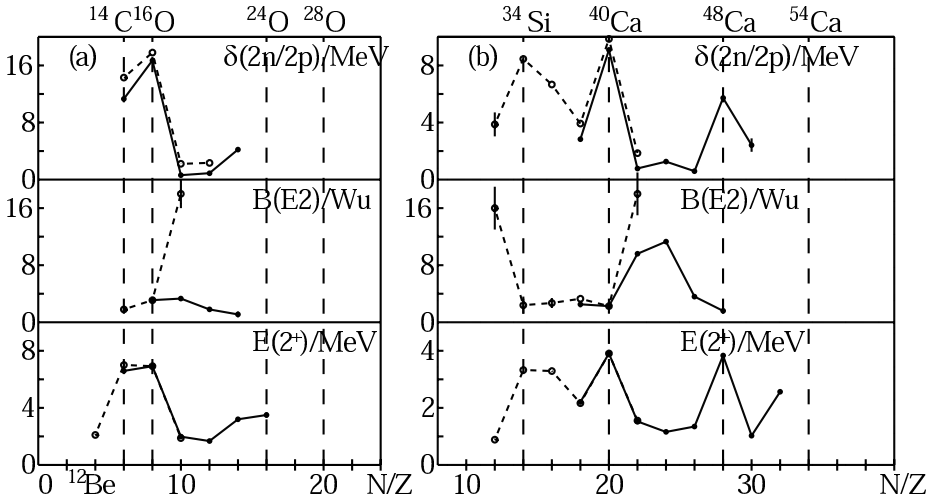

Figure 1.12: Shell signatures $\delta_{2n/2p}$, B(E2;$2^+ \rightarrow 0^+$) and $E(2^+)$ for shell evolution of nuclei (a) $Z = 8$ oxygen isotopes (full-line) and $N = 8$ isotones (dashed); (b) $Z = 20$ calcium isotopes (full-line) and $N = 20$ isotones (dashed). [24]

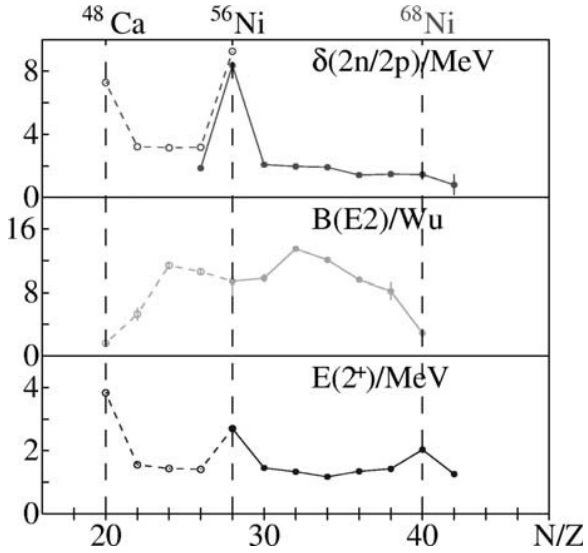

Figure 1.13: Shell signatures $\delta_{2n/2p}$, B(E2;$2^+ \rightarrow 0^+$) and $E(2^+)$ for shell evolution of nuclei $Z = 28$ nickel isotopes (full-line) and $N = 28$ isotones (dashed). [25]

A similar campaign of measurements has been later carried out using the AGATA Demonstrator Array [28] coupled to the PRISMA spectrometer. Even if a lot of work has been done, only the use of highly exotic projectiles will allow to explore the extreme limits of the nuclear chart. Therefore it is clear to the Nuclear Physics

community that the future developments in this field of research will depend strongly on the availability of intense radioactive ion beams produced in dedicated facilities.

1.2 Radioactive ion beam facilities

Studies have been carried out in the last decade at the first generation radioactive beam facilities (RIB). A brief summary of the working principles of a RIB facility will be given, together with a description aimed at explaining what is expected to upgrade their technical properties in the near future.
There are two different methods for the production of a radioactive ion beam: the Isotope Separation On-Line (ISOL) and the In-Flight technique (IF). Both have advantages and disadvantages and can be somehow considered complementary.
The ISOL method is the oldest one and can be attributed to the pioneering work of O.Kofoed-Hansen and K.O.Nielsen in 1951. Their technique consisted in bombarding an Uranium target with fast neutrons coming from the break-up of a 11 MeV deuteron beam. Neutron-rich, noble gas isotopes produced through fission were swept into the ion source of an electromagnetic isotope separator after thermalization in the target. The whole process of production, ionization, mass-separation, implantation into a detector set-up and subsequent detection of the emitted decay radiation was performed in a continuous way, hence the name: "Isotope Separation On Line". The ISOL method, schematically drawn in figure 1.14, is based on the production of radioactive species by spallation, fission or other nuclear reactions in a thick target at rest. These reactions can be induced by neutrons or photons as well as by intense beams of light charged particles. Neutrons are available as a by product of nuclear reactors or can be produced by a converter. High fluxes of photons can be obtained by the bremsstrahlung of intense energetic electron beams impinging on Tungsten targets. The more straightforward approach to directly use an intense beam of charged particles on a thick target has the drawback of the heat load of the target itself, which can limit the power on target that can be dissipated. This problem has been studied in detail and interesting solutions have been proposed [29, 30]. The isotopes produced in the thick target are then extracted and ionized to a certain charge state in an ion source. However, the diffusion in the target material depends on the chemical properties of the reaction products and may be quite long (of the order of seconds).

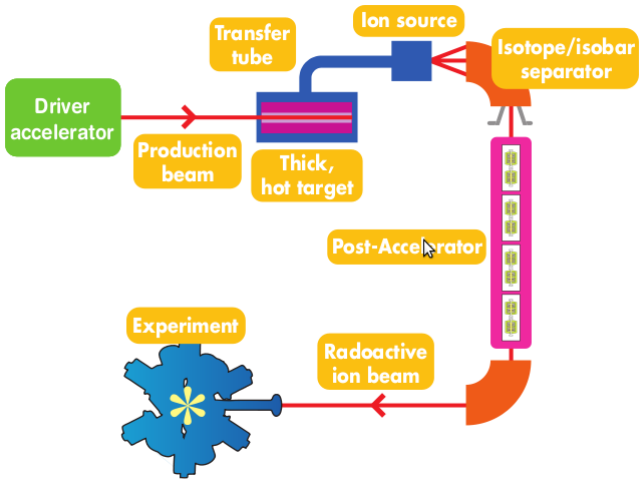

Figure 1.14: Schematic view of the ISOL technique. The high intensity primary beam impinges on a high temperature thick target. The reaction products are then extracted and ionized to produce the radioactive beam. This beam is then post-accelerated and used in nuclear physics experiments. Figure adapted from [14].

Moreover, the effusion and ionization are also quite slow processes characterized by times up to several ms. The total process can be quite longer than the average lifetimes of the shortest lived isotopes. This means that there is an a-priori limit in the region of the nuclear chart accessible with this technique. After the extraction from the target, the selected elements have to be ionized for a later magnetic separation and pre-acceleration. Depending on the requirements, several different ionization sources are used. For the RIB production, the source must operate steadily for extended periods of time at high temperatures (up to 2000°C). The selection of the target/ion-source system is very important since it determines the intensity, beam quality and number of RIBs that can be provided for the experiment. The worldwide spread RIB facilities make use of a large variety of solutions. Among the ion sources: surface ionization (SIS), plasma (FEBIAD), electron cyclotron resonance (ECR) and resonant laser ion (RILIS) techniques are used. The first mechanism is based on surface ionization: when an atom interacts with a heated surface, it can lose or gain one electron before leaving the surface. This technique is used for elements with very low ionization potentials to generate positive and negative ions, respectively. The surface ionization method is extremely selective when the elements produced in the same re-

actions present different ionization potentials. The plasma ion source is based on the Forced Electron Beam Induced Arc Discharge. It exploits the capabilities of the electrons produced from an indirectly heated disc-shaped cathode and accelerated into an anodic chamber, to ionize any atom entering the chamber volume which have an ionization potential smaller than the incident electron energy. It is working properly in conjunction with high temperature target material in a pressure range of $10^{-4} - 10^{-5}$ torr. Electron Cyclotron Resonance (ECR) sources are used for isotopes of elements with ionization potentials higher than 7 eV and for the creation of multiple-charged ions. The atoms of the ions are bombarded by energetic electrons and lose one or more of their outer electrons. This method is not very chemical selective, due to the non-selective nature of the ionization process. The resonance ionization ion source is based on the Laser ionization process: atoms are stepwise excited by laser photons injected in the extraction beam-line. This ionization process is usually done in two or three steps exploiting the atomic structure of the species of interest. For this reason, it allows for a very efficient elemental selection. After the ions are created in the ion source, they are extracted and accelerated in a DC electrical field. This energy is necessary for the transport and injection into an analyzing magnet where a first mass separation occurs. Since the selection process ends with a beam of very low energy, a further post acceleration is usually needed. As a result of this process, the quality of the secondary beam, in terms of energy and emittance, will be comparable to that of a stable beam from an existing facility.

Several ISOL facilities have been and are currently operating worldwide. Among them we underline the following: ISOLDE [31] at CERN, ISAC at TRIUMF (Canada) [32], HRIBF at ORNL (USA) [33]. It should be remarked that new projects to build ISOL facilities are available at the Laboratori Nazionali di Legnaro (SPES) [34] and at GANIL (SPIRAL II) [35]. The SPIRAL II project is based on a double step system where a 40 MeV deuteron beam impinges on a converter to produce neutrons. The latter are used to induce fission on a very thick UCx target aiming at the production of $10^{13} - 10^{14}$ fissions per second. The *Selective Production of Exotic Species* (SPES) project is concentrating on the production of neutron-rich radioactive nuclei with masses in the 80-160 range, by Uranium fission at a rate of 10^{13} fission/s. The proton driver is a cyclotron with variable energy (15-70 MeV) and a maximum current of 500 μA. In this case the proton beam will directly impinge on a segmented UCx target [36]. The produced RIBs will be post-accelerated with a superconducting LINAC up

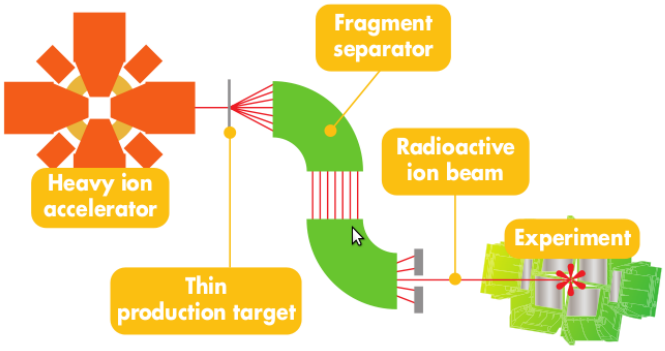

Figure 1.15: Schematic view of the In-Flight technique. A primary beam of stable heavy ions is accelerated to intermediate or high energy and impinges on the production target. Fragmentation reactions produce a wide variety of stable and unstable nuclear species among which a fragment separator is used to isolate the isotopes of interest. The radioactive beam is then sent to the experimental station. The Figure adapted from [14].

to energies of 11 AMeV for masses around 130. These energies allow to overcome the Coulomb repulsion between the radioactive beam and target nuclei in a large variety of systems. This feature, together with the increased beam intensities will allow new experimental studies employing different reaction mechanisms, such as multi-step Coulomb excitation, inelastic scattering, single and multiple nucleon transfers and fusion reactions. In the case of the In-Flight RIBs production method (see figure 1.15), a heavy-ion beam at very high energy (of the order of 40–2000 AMeV) collides with a target, inducing with high probability projectile fragmentation. After the primary target area, a complex system, composed of electric and magnetic separators and degraders, selects the desired isotopes, which can be focused to the secondary target position for the studies of interest. This technique is used, for instance, at the NSCL Laboratory of MSU where the experiment subject of this Thesis was performed.

In principle the projectile fragmentation gives rise to a large distribution of ions lighter than the projectile itself but only those reasonably close to the primary beam will be produced with high enough cross sections. Therefore only these nuclei will

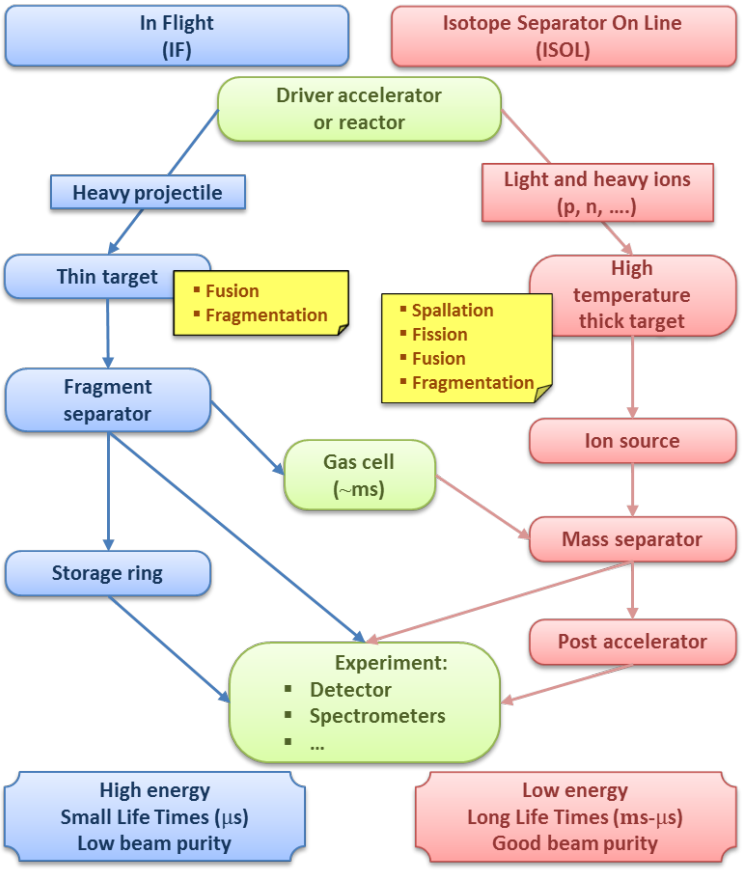

Figure 1.16: Overview of the Radioactive ion beams production methods. The interplay between the In-Flight and ISOL techniques is underlined.

be useful as secondary beams to produce further reactions for spectroscopic studies. The other products may only be used for mass measurement purposes aiming at the discovery of new isotopes [37]. One of the main features of this method is that the process is almost independent of the chemical properties, or the half-life of the isotopes of interest. The limitation of the half-life is only given by the flight time of the ions through the separator, which is generally less than 1 μs. Even though the particle identification of fast ions is relatively simple, the selection process using fragment separators results however in a lower beam purity with respect to the ISOL technique.

The existing In-Flight radioactive beam facilities in Europe at GANIL [38] and GSI [39], together with their counterparts at RIKEN[40], Japan, and MSU [41], USA,

developed methods for extracting valuable nuclear-structure information from scattering experiments with intermediate-to-high energy secondary beams of unstable nuclei, although restricted to nuclear masses up to $A = 80$ and intensities up to 10^5-10^7 pps, which should be compared with the 10^{11} pps of a stable beam. Great improvements came from their operation in the last decades. Among these: the discovery of new isotopes, the measurement of several nuclear masses and the study of nuclear spectroscopy of neutron-rich nuclei. Due to the low beam intensities available up to now, the nuclear structure information is typically obtained through direct reactions such as single nucleon transfer or Coulomb excitation. Even in the most favorable cases it is extremely difficult, if not impossible, to identify high-spin states with these techniques. In particular, using γ-spectroscopy, it is very difficult to study excited levels lying above the first excited state. Therefore, an increase in beam intensities by several orders of magnitude is aimed for, involving a large number of technological challenges.

In this framework the SPES and SPIRAL II projects are considered as a first step (second generation facilities) towards the road of new very performing third generation facilities.

For the future development of more intense radioactive ion beams, the possibility of combining the two complementary methods has been investigated as a way of overcoming their separate limitations. A general scheme is shown in figure 1.16. One of the new approaches to the production of low-energy radioactive beams involves the stopping of fast radioactive beams produced In-Flight, using a large gas catcher where the ions are thermalized in high-purity helium and extracted as singly charged ions for post-acceleration. This removes the limitation present in the standard ISOL technique for species that are difficult to extract from the target/ion source assembly. This is the case of the Facility for Rare Isotope Beams (FRIB) [42], which is a next generation facility proposed in the USA. Here, a primary heavy-ion accelerator capable of delivering intense ion beams up to uranium at 400 AMeV will be used for fission and fragmentation reactions. The produced ions will be either used as fast radioactive ion beams or thermalized by a gas-catcher and re-accelerated up to 12 AMeV.

FAIR [43] is a further next generation in-flight facility to be constructed at GSI [44]. In this facility, two synchrotron accelerators, will deliver heavy ion beams up to 1.5

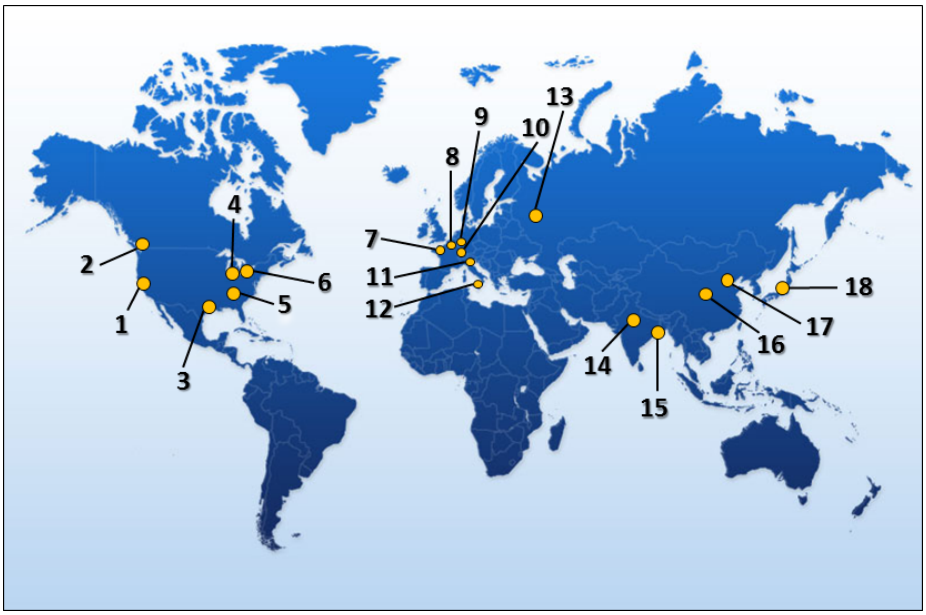

Figure 1.17: World map of the main radioactive ion beams facilities. Table 1.1 can be used as a legend.

AGeV for the production of exotic nuclei from fission and fragmentation reactions. The produced nuclei will be separated and identified using the Super-FRS magnetic spectrometer.

On the other hand, a combined ISOL/In-Flight method has been proposed. The idea is to obtain extremely neutron-rich nuclei from the fragmentation of post-accelerated radioactive ion beams produced by an high intensity ISOL target. This is the case of EURISOL [14], whose design study has been prepared aiming at the production of exotic radioactive ion beams with intensities many orders of magnitude greater than those available today. This facility will offer two different production modes depending on the target used. The first one is based on a multi-MW double-step production technique using a very high intensity proton beam on a liquid metal cooled spallation target. This will produce high fluxes of neutrons capable to induce a high rate of fission in the close-standing actinide target (10^{16} fissions/s). The second mode is the 100 kW direct target production. The driver accelerator at EURISOL will be a superconducting linear accelerator with 5 different sections, one able to accelerate protons up to 1 GeV with intensity of 5 mA for the multi-MW production mode and the other using 0.1 mA proton beam intensity for the 100 kW production mode. Fig-

ure 1.17 and table 1.1 show the world distribution of the main existing and planned Radioactive Ion Beams facilities.

	Laboratory	Facility	Reference
1	LBNL	88" cyclotron	
2	TRIUMF	ISAC I and II	[32]
3	TEXAS A&M		
4	ANL	CARIBU	
5	ORNL	HRIBF	[32]
6	NSCL	A1900	[41]
6	NSCL	FRIB	[42]
7	GANIL	SPIRAL	[38]
7	GANIL	SPIRAL II	[35]
8	Louvain-La-Neuve	ARENAS	
9	GSI	FRS	[39]
9	GSI	FAIR	[43]
10	CERN	REX-ISOLDE	[31]
10	CERN	HIE-ISOLDE	[31]
11	LNL	SPES	[34]
12	LNS	EXCYT	
13	DUBNA	DRIBS	
14	Delhi	HIRA	
15	Calcutta	VECC	
16	Lanzhou	CSR / HIARF	
17	Beijing	HI-13/BRIF	
18	RIKEN	RIBF and BigRIPS	

Table 1.1: List of the worldwide main radioactive ion beams facilities.

1.3 The Ni isotopic chain

The $_{28}$Ni isotopic chain, illustrated in figure 1.18, is one of the longest observed so far as it comprises 31 isotopes. Close to the two extremes of the proton and neutron-rich sides, there are two expected doubly-magic isotopes, ^{48}Ni [46] [47] and ^{78}Ni [48] [49]. The former is a prime candidate for the two-proton radioactivity, whereas the second is an important waiting-point in the path of the rapid-neutron-capture process. The isotopic chain comprises a third doubly-magic nucleus, namely the proton-rich

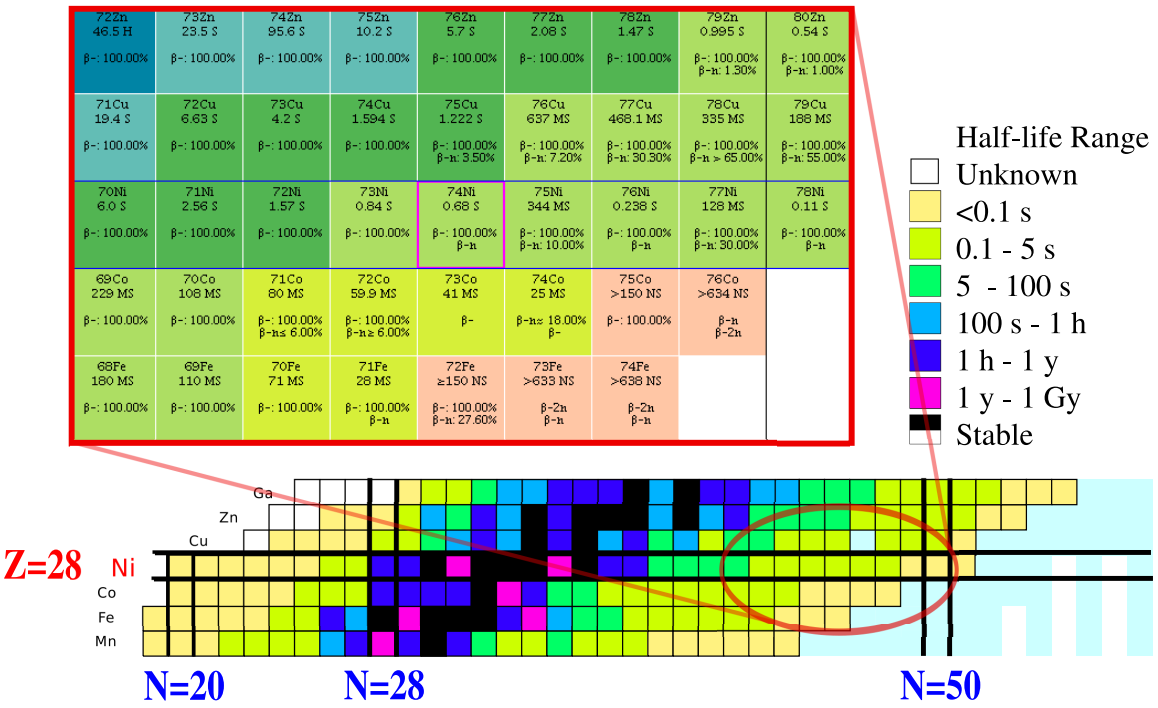

Figure 1.18: Zoom of the Ni isotopic chain from the Nuclear Chart. The region of interest for this work is highlited. Original figure is from [45], inset and updated data are taken from [8].

^{56}Ni. So far, only a few nuclei of ^{78}Ni have been produced worldwide, therefore its structure could not be studied yet and this represents one of the most interesting tasks to be achieved with the second generation radioactive ion beam facilities. The recent observation of ^{79}Ni [50] is also showing the possibility to obtain bound states beyond the doubly magic closure, validating the theoretical extrapolations that place the neutron drip line much further (N≈86) than the observed isotopes. Due to the extremely low production cross section values, also the spectroscopy of ^{79}Ni is quite far from being feasible. In the following we will limit our discussion up to mass 78.

The nuclear shells involved in the Ni isotopic chain are illustrated in figure 1.19 where the orange dots indicate the successive shell filling. The neutron valence orbitals involved in the shell model description are the following:

- the ν $f_{7/2}$ shell between ^{48}Ni and ^{56}Ni;
- the fp shells ($\nu f_{7/2}$, $\nu p_{3/2}$ and $\nu f_{5/2}$); between ^{56}Ni and ^{68}Ni

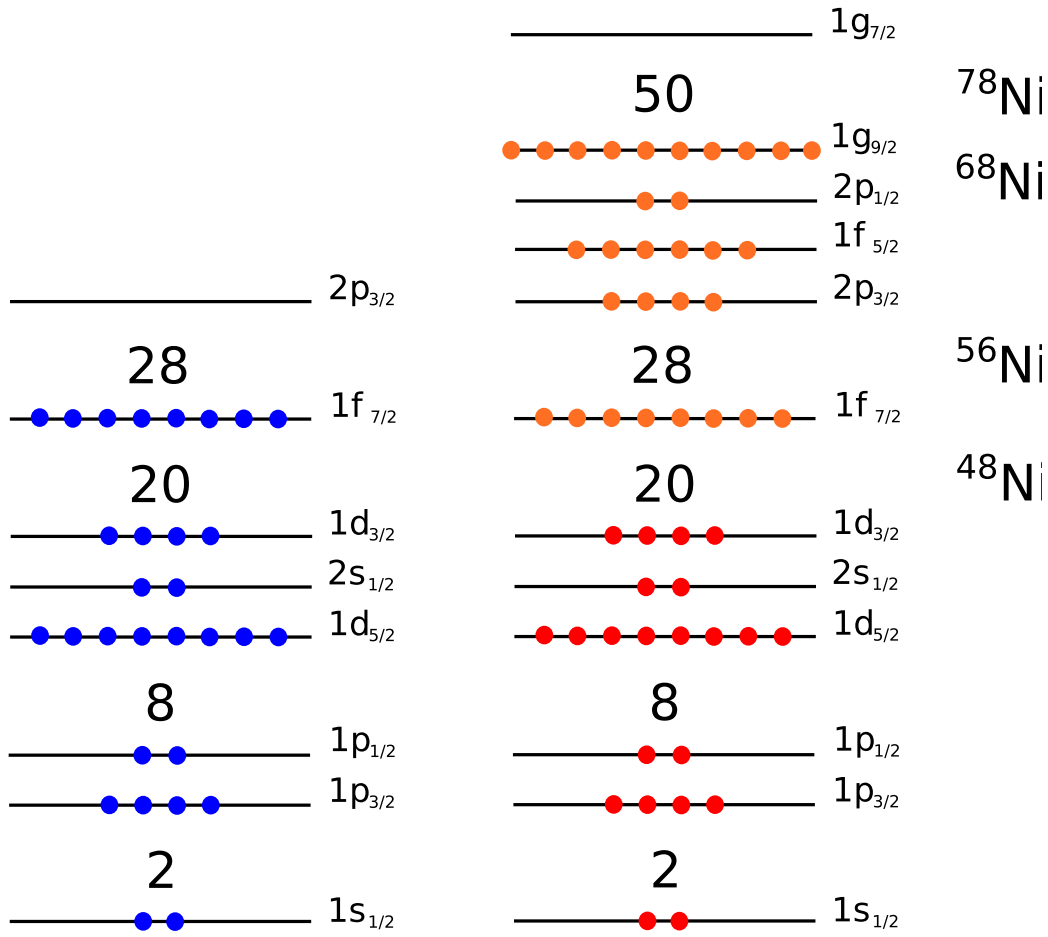

Figure 1.19: Schematic view of the shells involved in the Ni isotopic chain. Larger spacing between levels indicates the standard shells closure, other spacings have not to be intended as proportional to the levels energy. Blue dots represent the protons filling the closed shell core. Red dots are the neutrons filling the shells up to the first Ni isotope while the following neutron are depicted with orange dots rapresenting the successive shells filling along the isotopic chain. It is evident that this chain crosses N=20 and N=28 standard closures and reaches the N=50 one with ^{78}Ni.

- the $\nu g_{9/2}$ shell between ^{68}Ni and ^{78}Ni.

The existing Z=28 shell gap is formed between the occupied $\pi f_{7/2}$ and the valence $\pi p_{3/2}$ (or possibly $\pi f_{5/2}$) orbitals. On the average, its absolute value amounts to about 5 MeV, which is large enough to maintain the spherical shape of all Ni isotopes, even those located at mid-distance between N=28 and N=40 [51]. The filling of the neutron orbits going towards the heavier isotopes could polarize the proton core by specific proton-neutron interactions due to the strong neutron excess. Such effects

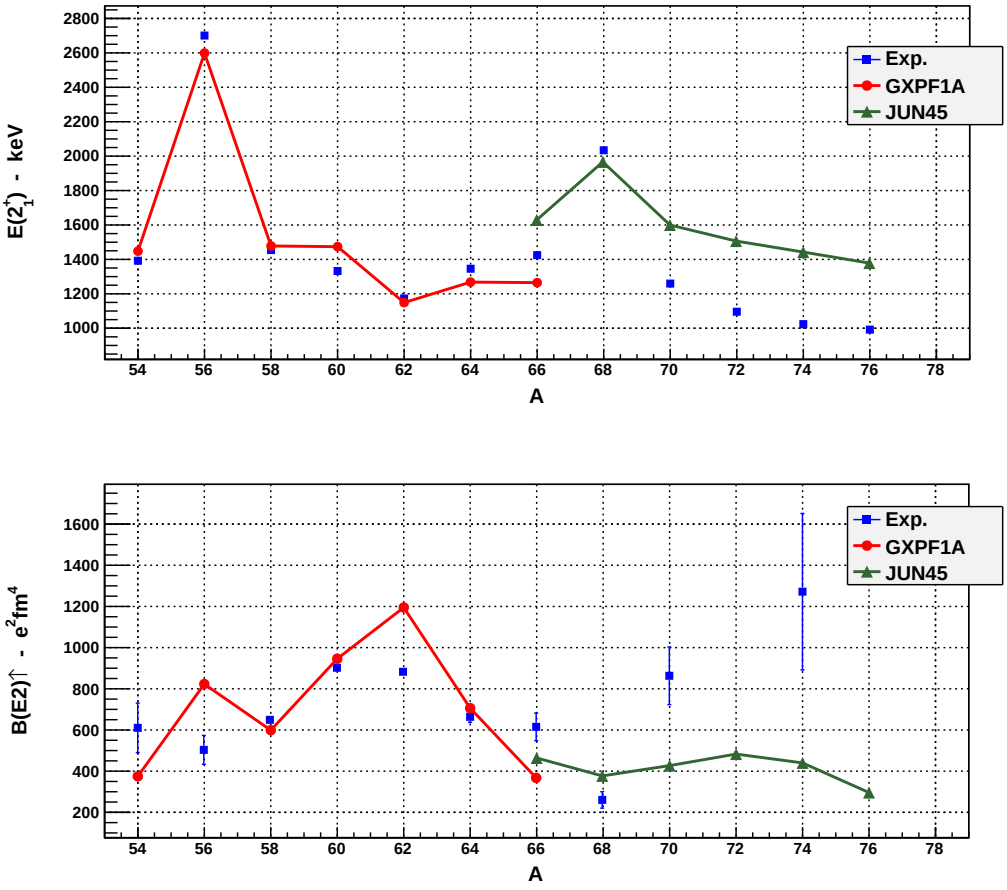

Figure 1.20: Experimental values and theoretical expectations from shell model calculations for the $E(2_1^+)$ energy (top panel) and $B(E2)\uparrow$ matrix element (bottom panel) for the known even-even Ni isotopes. Data are from [52].

can be revealed by the studies of the binding energies of the proton orbits and by the evolution of the $E(2^+)$ and B(E2) values along the Ni isotopic chain.

Trends of 2^+ energies and B(E2) values

Between the N=28 and N=50 shell closures, the Ni isotopes have been the subject of extensive experimental and theoretical studies (see [49, 53–62]). The experimental results on the 2_1^+ energies and B(E2; $0^+ \rightarrow 2^+$) values are drawn in figure 1.20. The energies of the 2_1^+ levels show distinct local maxima at N=28 and N=40, namely at the known (sub)shell closures. Going towards the heavier isotopes, the 2_1^+ energies slightly decrease up to the last measured value of ^{76}Ni. The trend of the B(E2) values

is opposite, reaching a maximum at or near mid-occupation by neutrons of the fp shell (N=34) and subsequently decreasing until N=40. Between $N_1 = 28$ and $N_2 = 40$, the B(E2) curve is well described by the generalized seniority scheme within the fp shells. In this approach [63, 64], exploiting the properties of nucleons paired to $J = 0^+$ in nearby orbits, the B(E2) values of $^{56-68}$Ni follow a parabola along the shell filling:

$$\mathrm{B(E2}; 0^+ \rightarrow 2_1^+) = c(\pi_{fp},\, \nu_{fp})\; F(1-F) \tag{1.11}$$

where $c(\pi fp,\, \nu fp)$ is representative of the strength of the proton-neutron interaction in the fp shells, and F is the fractional filling of the neutron shell, which varies between 0 at the beginning and 1 at the end of the shell. Between $N_1 = 28$ and $N_2 = 40$, F can be expressed as $F = (N - N_1)/(N_2 - N_1)$, where N is the number of neutrons. As neutrons are charge-less, their contribution to the increase of B(E2) is indirect, through the induced core polarization. The height of the parabola can be used to derive the strength of neutron-induced proton-core excitations. The proton core polarization occurs through quadrupole excitations via $(\pi \mathrm{f}_{7/2})^{-1}(\pi \mathrm{p}_{3/2})^{+1}$ configurations [53, 57]. Deviation from the parabola of eq. (1.11) are found for ^{56}Ni and ^{68}Ni for which the B(E2) values are slightly higher than expected with this simple model. For ^{56}Ni this is most likely due to the extended possibilities for creating 2^+ excitations across $N, Z = 28$ in the fp shell for protons and neutrons [65] and a consequence of a strong proton-neutron interaction expected in $N = Z$ nuclei [66]. The low B(E2) of ^{68}Ni , which is the minimum observed so far in the Ni chain, is comparable to that of other well studied doubly-magic nuclei, ^{16}O (3.3(3) W.u.), ^{40}Ca (2.3(4) W.u.) and ^{48}Ca (1.6(5) W.u.). Such a minimum has been taken as a strong indication of the existence of $N = 40$ subshell gap and of the lack of E2 excitations between the fp and the $\mathrm{g}_{9/2}$ orbitals of different parity values [57, 59].
Data for the heavier (beyond $N = 40$) Ni isotopes are quite scarce. As a matter of fact, the experimental information available up to recent years was limited to ^{70}Ni [61]. Despite the quite large error bars, the experimental B(E2) shows a steep increase compared to ^{68}Ni, suggesting an increased collectivity in the heavy Ni isotopes induced by the interaction of protons in the fp and neutrons in the $\mathrm{g}_{9/2}$ shell with a strength $c(\pi \mathrm{fp}, \nu \mathrm{g})$ (cf. eq. (1.11)) with $N_1 = 40$ and $N_2 = 50$). As a matter of comparison, the steep rise of the B(E2) between ^{68}Ni and ^{70}Ni could be compared to the more modest variations between ^{56}Ni [65] and ^{54}Ni or ^{58}Ni [62]. Beyond the

^{70}Ni limit, the only data available to date are from the nuclear excitation of ^{74}Ni in the proton inelastic scattering experiment recently performed by Aoi and collaborators in [67]. Results show also in this case a large B(E2) value that could indicate the validity of the enhanced collectivity hypothesis. This enhancement goes in parallel with a gradual reduction of 2_1^+ excitation energy from ^{70}Ni to ^{76}Ni [60] which cannot be understood solely from pure neutron excitations within the $g_{9/2}$ shell and requires the simultaneous reduction of the $Z = 28$ gap. This strong polarization in the Ni isotopes beyond $N = 40$ is likely to be due to the strongly attractive $\pi f_{5/2}\nu g_{9/2}$ monopole interaction [68], assigned to the tensor force of the in-medium nucleon-nucleon interaction. This force is also predicted to act through the repulsive $\pi f_{7/2}\nu g_{9/2}$ interaction.

1.4 The experiment on ^{74}Ni

From the previous discussion, it is clear that further experimental data are essential to clarify the situation of the heavy Ni isotopes and especially the observed "anomaly" of the measured B(E2) value of ^{70}Ni. Applying the generalized seniority scheme within the $g_{9/2}$ orbital, one would expect a parabolic trend for the B(E2) values going from ^{68}Ni to ^{78}Ni, with a further increase of B(E2) going from ^{70}Ni to ^{72,74}Ni, which therefore would have extremely high collectivity with consequently large B(E2). In order to shed some light on this issue, we decided to attempt measuring the reduced transition probability B(E2; $0^+ \rightarrow 2_1^+$) for the ^{74}Ni nucleus by Coulomb excitation. Available data on this nucleus come from the works by C. Mazzocchi [60], N. Aoi [67] and respective collaborators. In the former work, the energy of the 2_1^+ and 4_1^+ levels was determined measuring the β decay of ^{74}Co. The spectrum obtained in this work is shown in figure 1.21 together with the decay scheme deduced from the same data set. The latter work, as discussed in the previous paragraph, measured the $B(E2; 0^+ \rightarrow 2^+)$ probability in a proton inelastic scattering experiment. The results of these works shall be considered as the starting point for the present work.

In the experiment we are considering, the ^{74}Ni nuclei were produced in a "cocktail beam" at the NSCL radioactive ion beam facility of MSU and Coulomb-excited on a Gold target. Scattered particles have been measured using the S800 spectrometer while the γ-rays were detected with the 4π CAESAR scintillator array. The next

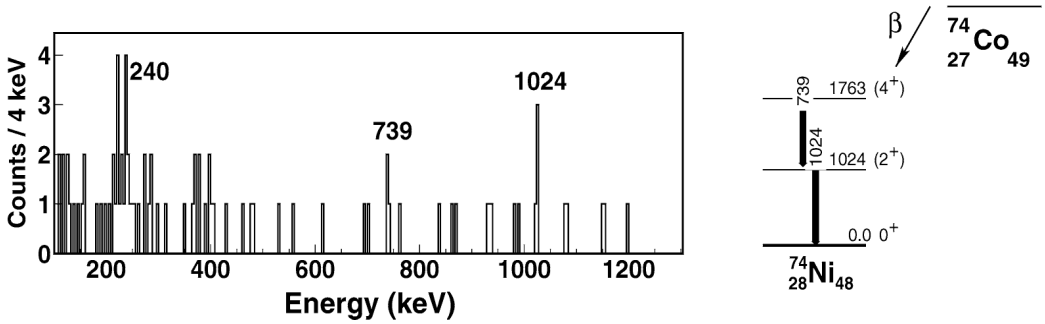

Figure 1.21: Experimental ^{74}Ni level scheme. On the left: the γ-ray spectrum as measured from the ^{74}Co β decay. On the right: level scheme as reconstructed from the systematics of even-even Ni isotopes. Adapted from [60]

chapter will be dedicated to a brief review of the main ideas concerning Coulomb excitation while the remaining chapters will be dedicated to the experimental setup and data analysis.

2

Coulomb Excitation

One of the best-known and widely-used processes to populate nuclei in excited states is the Coulomb Excitation (or *Coulex*), where the inelastic scattering of a charged projectile on a target nucleus causes the electromagnetic excitation of one or both the reaction partners.
One can name as “pure” Coulomb excitation the particular process in which the charge distributions of the two nuclei do not overlap at any time during the collision and therefore projectile and target only interact through the electromagnetic field. This is always the case if the available energy is lower than the Coulomb barrier and allows to express the reaction cross section in terms of the same electromagnetic multipole matrix elements characterizing the electromagnetic decay of nuclear states. If the available energy is above the Coulomb barrier one has to put particular care on the impact parameter selection in order to disentangle nuclear and electromagnetic forces contribution.
In this chapter, after recalling some basic features of the nuclear gamma decays, we will focus on the theoretical models describing Coulomb Excitation at low and relativistic energies. We will see how these two ”extreme“ descriptions match in the

framework of intermediate energy processes and how the reduced transition probabilities can be extracted from the measured reaction cross sections. This practice is quite common in nuclear spectroscopy, hence it is often referred as Coulomb Excitation Technique.

2.1 Gamma Decay

The formalism describing the de-excitation of nuclei via photon emission is well known and can be found in several textbooks, see for instance [69]. It is however worth recalling here the main features which will be used later in the description of the Coulomb excitation processes.
Any generic operator $\mathcal{O}$ inducing an electromagnetic transition between the initial $|i>=|E_i, J_i^{\pi_i}>$ and the final $|f>=|E_f, J_f^{\pi_f}>$ nuclear states can be expressed in terms of a sum of electric and magnetic multipole operators with tensor rank λ:

$$\mathcal{O} = \sum_{\lambda,\mu}[\mathcal{O}(E\lambda)_\mu + \mathcal{O}(M\lambda)_\mu]. \tag{2.1}$$

If more than one multipolarity is allowed, the lowest one typically dominates in the decay rate by several orders of magnitude.
Since the rank of the operator corresponds to the angular momentum carried away by the photon, the usual rules for angular momentum conservation apply:

$$|J_i - J_f| \leq \lambda \leq J_i + J_f. \tag{2.2}$$

It should be pointed out that, since the photon has an intrinsic spin of 1, transitions with $\lambda = 0$ involving photon emission are forbidden, while the competing electromagnetic process of electronic internal conversion is still allowed. As for the parity, since the parity of the radiation fields is given [70]:

$$\pi(E\lambda) = (-1)^\lambda \quad \pi(M\lambda) = (-1)^{\lambda+1} \tag{2.3}$$

other selection rules apply: states of the same parity can be only connected by electric multipoles with even λ or by magnetic multipoles with odd λ; states with opposite parity can only be connected by electric multipoles with odd λ or by magnetic

Δl	transition name	$\pi_i\pi_f = +1$	$\pi_i\pi_f = -1$
0	*forbidden*	-	-
1	*dipole*	M1	E1
2	*quadrupole*	E2	M2
3	*octupole*	M3	E3

Table 2.1: Electromagnetic transitions involving photon emission allowed by the selection rules. The list is limited to $\Delta l \leqslant 3$.

multipoles with even λ. These selection rules are summarized in table 2.1.

It can be shown that the total transition rate between the initial and the final states is given by the following expression:

$$W_{i,f,\lambda} = \frac{1}{\hbar}\left(\frac{8\pi(\lambda+1)}{\lambda[(2\lambda+1)!!]^2}\right)\left(\frac{E_\gamma}{\hbar c}\right)^{2\lambda+1}\frac{|<J_f||\mathcal{O}(\lambda)||J_i>|^2}{(2J_i+1)} \tag{2.4}$$

The last factor of this expansion is usually called the **reduced transition probability** (**B**), defined as:

$$B(i \to f) = \frac{|<J_f||\mathcal{O}(\lambda)||J_i>|^2}{(2J_i+1)} \tag{2.5}$$

As discussed in paragraph 1.1.2, this quantity is one of the most sensitive probes to characterize how well nuclear models reproduce nuclear structure properties. One important observable that can be derived immediately is the excited state *lifetime*:

$$\tau_{if} = \frac{1}{W_{if}} \propto \frac{1}{B(i \to f)E_\gamma^{2\lambda+1}} \tag{2.6}$$

It should be noted that B depends upon the direction of the transition. For the gamma decays we are talking about the usual situation is $J_i \geq J_f$, $E_i > E_f$, in other words the initial state lies above the final state. On the contrary, in the case of Coulomb excitation that we are going to discuss, the initial state lies below the final state and one often uses the notation $B(\uparrow)$ for this situation. If J_a is the lower state, J_b is the higher one and $B(\uparrow)$ is given, then the correct value for the transition $J_b \to J_a$ is:

$$B(\downarrow b \to a) = \frac{(2J_a+1)}{(2J_b+1)}B(\uparrow a \to b) \tag{2.7}$$

In general, a level may gamma decay by several multipoles to a given final state

and one has to sum all the partial transition rates (i.e. sum over multi-polarities and operators) to obtain the total transition rate:

$$W_{i,f} = \sum_{\lambda} [W_{i,f}(E\lambda) + W_{i,f}(M\lambda)] \tag{2.8}$$

Even if this is formally exact, one has to note that considering a typical de-excitation energy (E_γ ≈1 MeV) the rate for electric or magnetic transitions with the higher-order multipolarity ($\lambda' = \lambda + 2$, due to the selection rules) is reduced of about seven orders of magnitude. For this reason, in most cases only the lowest multi-pole for a given type of transition have to be considered. Only the case of the lowest order electric and magnetic transitions can lead to appreciable mixing and requires the introduction of mixing and branching ratios. Since this is out of the scope of our discussion, we will not go in further details.

Weisskopf units for gamma decay

The $B(\lambda)$ values are not dimensionless quantities: for electric transitions they are given in units of e^2 fm$^{2\lambda}$ while the magnetic ones are in units of the nuclear magneton μ_N^2 fm$^{2(\lambda-1)}$. It is common practice to express the reduced transition probability in terms of "single-particle" or "Weisskopf" units. The single-particle units, as the name suggests, correspond to the reduced transition probabilities evaluated for a transition induced by a single particle. The resulting expression for the single-particle units is the following:

$$B_W(E\lambda) = \left(\frac{1}{4\pi}\right)\left[\frac{3}{(3+\lambda)}\right]^2 (1.2A^{1/3})^{2\lambda} e^2 \ fm^{2\lambda} \tag{2.9}$$

$$B_W(M\lambda) = \left(\frac{10}{\pi}\right)\left[\frac{3}{(3+\lambda)}\right]^2 (1.2A^{1/3})^{2\lambda-2} \mu_N^2 \ fm^{2\lambda-2} \tag{2.10}$$

For the lowest multipolarities one obtains:

$$\begin{aligned} B_W(E1\downarrow) &= 0.0645A^{2/3} \ e^2 \ fm^2 \\ B_W(E2\downarrow) &= 0.0594A^{4/3} \ e^2 \ fm^4 \\ B_W(M1\downarrow) &= 1.790 \ \mu_N^2 \end{aligned} \tag{2.11}$$

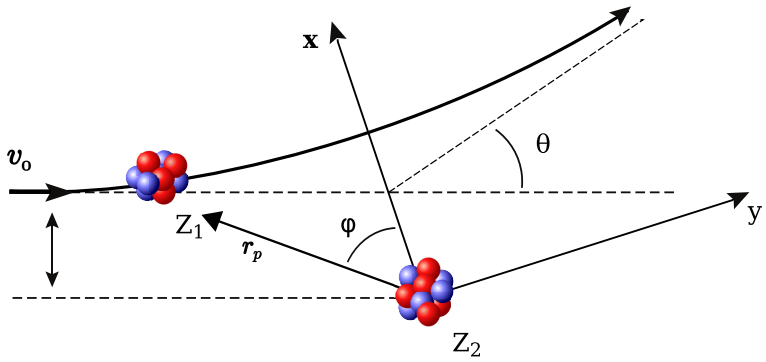

Figure 2.1: Rutherford scattering schematics. The projectile Z_1 travels towards the target nucleus Z_2 with velocity **v** and impact parameter b. The trajectory of the incident particle is described by the vector **r**. θ is the **scattering angle**.

It is important to notice that the experimental values of the nuclear transition probabilities may show strong deviations from the single particle estimate. Electric dipole transitions are usually much weaker than the estimate, while E2 transitions are often found to be strongly enhanced with respect to the single particle estimate. In these cases the transition is induced by the coherent contribution of several particles, meaning that the effects of nuclear collectivity are apparent.

2.2 Elastic Coulomb Scattering

For the continuation of our discussion, it is useful to recall the main features of the Elastic Coulomb Scattering (also called *Rutherford Scattering*).
The geometry of the process is shown in figure 2.1. Due to the $1/r^2$ dependence of the Coulomb force, the scattered particles will follow a hyperbolic path. It is common practice to assume the target nucleus to be infinitely massive to keep the scattering center fixed. The *impact parameter* b is defined as the distance between the straight line trajectory of the projectile and its parallel path crossing the target nucleus. Let Z_1 and Z_2 be the charge numbers of the projectile and the target respectively; m and v the reduced mass of the system and the relative velocity of the particles (e, as usual, is the electron charge). From total energy and momentum conservation arguments one can obtain the *classical distance of closest approach*:

$$a = 2a_0 = \frac{2Z_1 Z_2 e^2}{mv^2} \tag{2.12}$$

and the *differential cross section for Rutherford scattering*:

$$\frac{d\sigma}{d\Omega} = \left(\frac{zZe^2}{4\pi\epsilon_0}\right)^2 \left(\frac{1}{4T_a}\right)^2 \frac{1}{\sin^4(\frac{\theta}{2})} \tag{2.13}$$

where $T_a = \frac{1}{2}m_1 v_0^2$ is the incident particle kinetic energy and the impact parameter is related to the scattering angle by the formula:

$$b = a_0 \cot\left(\frac{\theta}{2}\right). \tag{2.14}$$

The semi-classical approximation used to obtain such results is justified if the value of the *Sommerfeld Parameter*

$$\eta = \frac{Z_1 Z_2 e^2}{\hbar v}. \tag{2.15}$$

is larger than unity (see, for example [71]).

2.3 Theory of Coulomb Excitation

As mentioned in the introduction, Coulomb excitation is the process of inelastic scattering where a charged particle or a nucleus transfers energy to another nucleus via the electromagnetic field. It is essentially a perturbation of the Rutherford scattering where one or both partners of the reaction gain excitation energy from their electromagnetic interaction.

At low energies, the semi-classical approximation is assumed to be valid as for the Rutherford scattering: the Coulomb interaction is computed considering the classical Rutherford trajectory and the relative energy of the particles is assumed to be much larger than the excitation one. This allows to disentangle intrinsic excitations from the relative motion. Usually the available energy is lower than the Coulomb barrier ($E_B = \frac{Z_1 Z_2 e^2}{R_1 + R_2}$) so that the distance between the two nuclei is always larger than the sum of the two nuclear radii and the strong force contribution due to direct nuclear interaction is negligible. At high energies, the situation is opposite and one has to remove the strong interaction component, limiting the experimental and theoretical attention to ”safe“ impact parameters.

The case of intermediate-energy collisions of heavy ions is the one of interest for the

present thesis ($25 < E_{\mathrm{lab}} < 300$ AMeV). Since the particles travel with relativistic velocity ($0.25 < \beta = v/c < 0.65$), one has to treat the problem as in case of high energy collisions and to account for the relativistic effect of field retardation [72]. On the other hand, low-energy features like recoil effects still play an important role weakening the validity of assuming a straight line trajectory. Therefore it becomes necessary to develop a theory able to combine both aspects. We will see how this can be done, with a good degree of approximation, introducing a scaling factor of the distance of closest approach.
Since, in the present thesis, we are interested in the excitation of the low-lying states of the nucleus ^{74}Ni at beam energy ≈ 80 AMeV, we will not enter into details about higher-order excitations or about giant resonance excitation modes. These features can be treated in the same framework we are using, but the photon decay (that is only one of the possible decay modes) gives rise to high energy gamma rays (10-30 MeV) and is characterized by very low probabilities of emission [73]. In experiments like the one discussed in this work, where highly exotic, low intensity beams are used, it becomes extremely difficult to measure this kind of processes.

2.3.1 Low Energy Coulex

Both the semi-classical and the quantum-mechanical formulations of the excitation cross sections in low energy collisions have been derived by Alder and Winther, Bohr and Mottelson and Huus in [74] and are explained within details in reference books like [75] and many others. Bertulani gave a complete review of this specific topic and, more generally, about all the aspects of Coulomb Excitation in [73].
It can be shown that a semi-classical approach to the problem leads, with a good degree of approximation, to the same results that can be obtained with a more proper but less straightforward quantum mechanical calculation. Since we are interested in higher-energy collisions, we will only recall some concepts valid in the low-energy regime that will be useful for the continuation of the discussion, concentrating on the semi-classical treatment.
At low energy ($v \ll c$) or for heavy nuclei ($Z_1 Z_2 > 137$), the Sommerfeld Parameter (2.15) can be easily larger than unity so that the condition for the semi-classical trajectory approximation is valid. This is also the reason why typical Coulomb excitation experiments with heavy ions are better performed using heavy targets such

as Au, Pb, Bi. Moreover, for the inelastic collision, in order for the trajectory to be essentially the classical one, it is necessary that the energy loss due to the excitation is negligible with respect to the bombarding energy. In this picture, the nuclear excitation is the result of the time-dependent electromagnetic field of one particle acting on the other and causing its excitation. In most cases and for low multipole orders, the effect of this field is small and may be treated by first-order perturbation theory where the excitation probability can be expressed in terms of the same nuclear matrix elements used for the radiative decay description in 2.1.
Considering a potential V describing the interaction between the incident particle and the target, the matrix element for the transition from the ground state $|i>$ to the excited state $|f>$ is:

$$V_{if} =< f|V|i >= \int \Psi_f^* V \Psi_i d\tau \tag{2.16}$$

and the transition amplitude a_{if} for the excitation is:

$$a_{if} = -\frac{i}{\hbar} \int V_{if} e^{i\omega t} dt \tag{2.17}$$

where $\omega = (E_f - E_i/\hbar)$.
The transition probability is given by $|a_{if}|^2$ and should be integrated along the projectile trajectory. This can be conventionally done factorizing the total cross section in terms of the Rutherford one:

$$\left(\frac{d\sigma}{d\Omega}\right) = \left(\frac{d\sigma}{d\Omega}\right)_{Ruth} |a_{if}|^2 \tag{2.18}$$

Electric excitations
In the low energy regime we can write the interaction potential in terms of the Coulomb interaction:

$$\phi(\mathbf{r}, t) = \frac{Z_1 e}{|\mathbf{r} - \mathbf{r}_p(t)|} - \frac{Z_1 e}{r_p(t)} \tag{2.19}$$

where, according to figure 2.1, $\mathbf{r}(t)$ is the time dependent trajectory of the projectile. The corresponding Hamiltonian can be written as:

$$H_E(t) = \int \rho_n(\mathbf{r})\ \phi(\mathbf{r}, t)\ d\tau \tag{2.20}$$

where ρ_n is the nuclear charge density. Having disentangled the mass centers interaction, which is responsible for scattering, from the excitation part in (2.19), one can perform a multipole expansion and compute the excitation amplitude. The additional assumption of considering the excitation of only one of the reaction partners (i.e. the target) is needed. It can be shown that the reciprocal case is equivalent [76]. Defining the "orbital integral" as:

$$S_{E\lambda\mu} = \int_{-\infty}^{\infty} e^{i\omega t}\ Y_{\lambda\mu}(\theta_p(t), \phi_p(t))\ [r_p(t)]^{-\lambda-1} dt \tag{2.21}$$

the calculation leads to the following expression for the excitation cross section:

$$\frac{d\sigma_{E\lambda}}{d\Omega} = \left(\frac{2\pi Z_1 e a}{\hbar \sin^2(\theta/2)}\right)^2 \frac{B(E\lambda)}{(2\lambda+1)^3} \sum_{\mu} |S_{E\lambda,\mu}|^2 \tag{2.22}$$

The excitation considered so far is produced by the electrostatic interaction and is subject to the selection rules for the electric multipole radiation. Excitations of the opposite parity can be produced by magnetic interaction (see table 2.1). The latter cross sections are usually much smaller than the electric equivalent since the bombarding energy is low and hence the projectile velocity is also small compared to the speed of light. Some mixing is however possible and where the electric excitations are forbidden it may be possible to observe pure magnetic excitations.

Inclusion of magnetic excitations

With respect to what was done before, one has to add the vector potential produced by the spinless projectile following a classical trajectory:

$$\mathbf{A}(\mathbf{r}, t) = \frac{Z_1 e}{c} \frac{\mathbf{v}_p(t)}{|\mathbf{r} - \mathbf{r}_p(t)|} \tag{2.23}$$

leading to the Hamiltonian:

$$H_M(t) = -\frac{1}{c} \int \mathbf{j}_n(\mathbf{r}) \cdot \mathbf{A}(\mathbf{r}, t) d\tau. \tag{2.24}$$

In this case the orbital integrals become:

$$S_{M\lambda,\mu} = -\frac{\hbar}{\lambda m_0 c} \mathbf{l_p} \int \nabla_p r_p^{-\lambda-1} Y_{\lambda\mu}(\theta_p, \phi_p) e^{i\omega t} dt. \tag{2.25}$$

where $\hbar\mathbf{l_p}$ is the orbital angular momentum of the relative motion.

The solution of the general problem of $H_{tot} = H_E + H_M$ can be obtained after a calculation that we are not going to discuss here. The final result is the differential cross section for the transition $i \rightarrow f$:

$$\frac{d\sigma_{i\rightarrow f}}{d\Omega} = \left(\frac{2\pi Z_1 ea}{\hbar \sin^2(\theta/2)}\right)^2 \sum_{\pi\lambda\mu} \frac{B(\pi\lambda, i \rightarrow f)}{(2\lambda+1)^3} \sum_{\mu} |S_{\pi\lambda,\mu}|^2 \tag{2.26}$$

where $\pi = E$ or M stands for the type of multipolarity. The calculation of the cross sections is now connected to the knowledge of the reduced matrix element $B(\pi\lambda)$ and the computation of the orbital integrals 2.21 and 2.25. In order to perform this calculation, the dimensionless quantity ξ called "adiabaticity parameter" is introduced. If the time of internal motion in the nucleus is $t_{nucl} = \hbar/(E_f - E_i) = 1/\omega_{fi}$ and the interaction time allowed by the projectile motion is $t_{coll} = a/v$, the adiabaticity parameter is:

$$\xi = \frac{t_{coll}}{t_{nucl}} = \omega_{fi}\frac{a}{v} \tag{2.27}$$

Naively speaking this quantity represents the time the two particles spend close to each other with respect to the time of the internal motion in the nucleus. If the two characteristic times are comparable (i.e. $\xi < 1$), the probability of excitation is enhanced and Coulomb excitation is a favorite process, otherwise the nucleus responds adiabatically to the interaction, strongly suppressing the corresponding cross section. This condition limits the possible excitation energies to be below 1-2 MeV in low energy collisions.

2.3.2 Relativistic Coulomb excitation

The original work on Relativistic Coulomb Excitation is the one by Alder and Winther in 1979 [76]. Improvements and discussions came from Bertulani and coworkers [77] [78]. As discussed in the introduction, the starting point is to restrict the field to pure Coulomb Excitations, excluding collisions where the impact parameter b is smaller than the sum of the radii of the two colliding nuclei ($b \geq b_{min}$). Connected to this and to the high energy of the projectile is the assumption of projectile's straight line trajectory: no recoils are considered. Therefore, the distance of closest approach

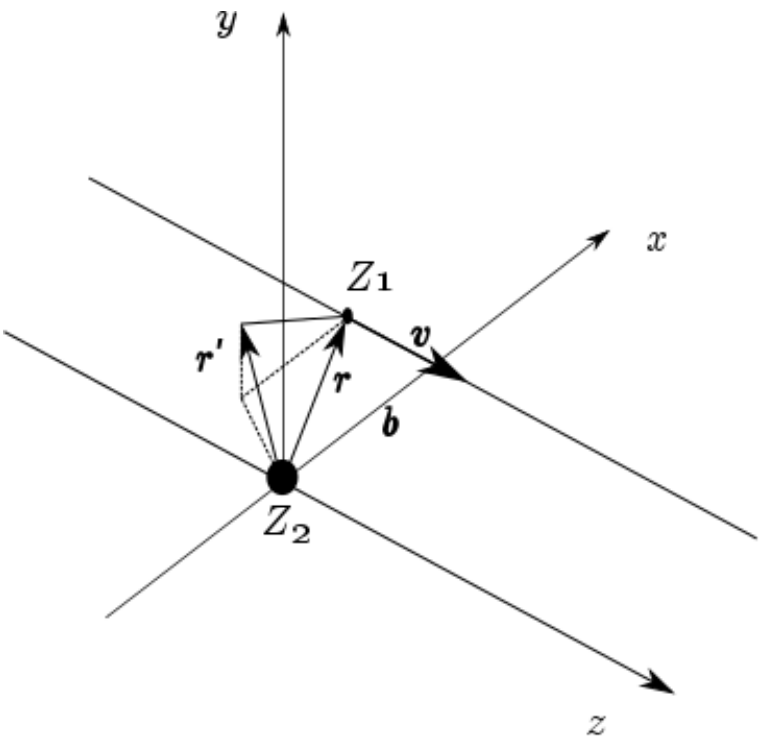

Figure 2.2: Schematics of the relativistic Coulomb excitation process notation used in the text. The projectile moves along a straight line trajectory.

can be replaced directly by the impact parameter b. Keeping the Lorentz boost into account, i.e. the factor $\gamma = \frac{1}{\sqrt{1-\beta^2}}$, the adiabaticity parameter for the relativistic case becomes:

$$\xi = \omega_{fi}\frac{b}{\gamma v} < 1 \tag{2.28}$$

Also in this case the excitation amplitudes and cross sections can be derived using a semi-classical approach. Figure 2.2 shows the notation used. The coordinate system has origin in the center of mass of the excited nucleus (again the target for historical reasons); the z axis is along the projectile velocity $\vec{v}$, which is assumed to be constant. Doing so the x-axis is in the plane of the trajectory and the x-component of the projectile path is fixed to b.
As in the low energy case, one can express the cross section for exciting a defined state $|i>$ to a state $|f>$ in terms of the Rutherford cross section multiplied by the excitation probability (equation 2.18). Assuming that the time-dependent electromagnetic field $V(\mathbf{r})$ from the projectile only excites the target weakly, one can use again per-

turbation theory to evaluate the excitation amplitudes. In the coordinate system we have chosen, the electromagnetic field produced by the projectile can be derived from a vector-potential $\mathbf{A}(\mathbf{r},t)$ obtained using the Lienard-Wiechert expression:

$$\phi(\mathbf{r},t) = \frac{\gamma Z_1 e}{\sqrt{(x-b)^2 + y^2 + \gamma^2(z-vt)^2}} \tag{2.29}$$

$$\mathbf{A}(\mathbf{r},t) = \frac{\mathbf{v}}{c}\phi(\mathbf{r},t) \tag{2.30}$$

The γ factor in the Lienard-Wiechert expression accounts for retardation effects. The multipole expansion and the separation of the relative motion from the excitation components lead to the excitation amplitudes:

$$a_{fi} = -i\frac{Z_1 e}{\hbar v\gamma}\sum_{\pi\lambda\mu} G_{\pi\lambda\mu}\left(\frac{c}{v}\right)(-1)^{\mu} K_{\mu}(\xi(b))\sqrt{2\lambda+1}\|^{\lambda} < I_f M_f|\mathcal{O}(\pi\lambda\mu)|I_i M_i > /e \tag{2.31}$$

where the notation used is the following:

- π is again the Electric or Magnetic type of excitation.
- $\xi(b)$ is the relativistic version of the adiabaticity parameter as given in 2.28
- K_{μ} are the modified Bessel functions (see, for example, figure 2 of [76])
- $G_{\pi\lambda\mu}(x)$ are analytical functions defined in [76].

The resulting expression for the cross section is:

$$\begin{aligned}\sigma_{i\to f} &= 2\pi\int_{b_{min}}^{\infty} b\ db(2J_i+1)^{-1}\sum_{M_i M_f}|a_{i\to f}|^2 \\ &= \left(\frac{Z_1 e^2}{\hbar c}\right)^2 \sum_{\pi\lambda\mu} k^{2(\lambda-1)}\frac{B(\pi\lambda; J_i\to J_f)}{e^2}\left|G_{\pi LM}\left(\frac{c}{v}\right)\right|^2 g_{\mu}(\xi(R))\end{aligned} \tag{2.32}$$

where

$$g_{\mu}(\xi(R)) = 2\pi\left(\frac{\omega}{v\gamma}\right)^2\int_{b_{min}}^{\infty} b\ db\ |K_{\mu}(\xi(b))|^2 \tag{2.33}$$

is an analytical expression that can be calculated in terms of the modified Bessel functions (see figure 3 in [76]). Here, as in the low-energy case, it is important to notice the direct relation between the excitation cross section and the transition matrix element that allows to extract the $B(\pi\lambda)$ value. Since in the relativistic limit the adiabaticity parameter (2.28) is always smaller than one, the excitation cross section 2.32 can be approximated as follows:

$$\sigma_{\pi\lambda} \approx \left(\frac{Z_1 e^2}{\hbar c}\right)^2 \frac{B(\pi\lambda, 0 \to \lambda)}{e^2} \pi b_{min}^{2(1-\lambda)} \times \begin{cases} (\lambda-1)^{-1} & \text{for } \lambda \geq 2 \\ 2\ln(\frac{b_{max}}{b_{min}}) & \text{for } \lambda = 1 \end{cases} \tag{2.34}$$

and, accounting for the possible presence of different multipolarities, the total excitation cross section becomes:

$$\sigma_{i\to f} = \sum_{\pi\lambda} \sigma_{\pi\lambda} \tag{2.35}$$

An alternative approach to Winther and Alder's semi-classical formulation is the so-called Weizsäcker–Williams method developed in the 1930s [79, 80] which describes Coulomb excitation in terms of equivalent photon numbers. The Coulomb excitation cross section $\sigma_{1\to 2}$ and the corresponding photo-absorption cross section σ_{abs} are related via the equivalent photon numbers, $n_{\pi\lambda}$, through

$$\sigma_{i\to f} = \frac{n_{\pi\lambda}}{E} \sigma_{abs}. \tag{2.36}$$

The Coulomb excitation cross section can thus be factorized into a part which depends solely on the reaction mechanism, $n_{\pi\lambda}$, and a part which depends on the structure of nucleus to be excited, σ_{abs}. It has been shown that the Weizsäcker–Williams method and Winther and Alder's approach yield the same result for the calculation of relativistic E1 excitation cross sections [81]. The equivalent photon method has been extended to all multipolarities [82]. The two approaches have been compared [77, 83] and a self-contained derivation of both formulations can be found in a review by Bertulani and Baur [78]. An interpolation between the relativistic and non-relativistic Coulomb excitation theories was suggested [84] and subsequently performed [85].

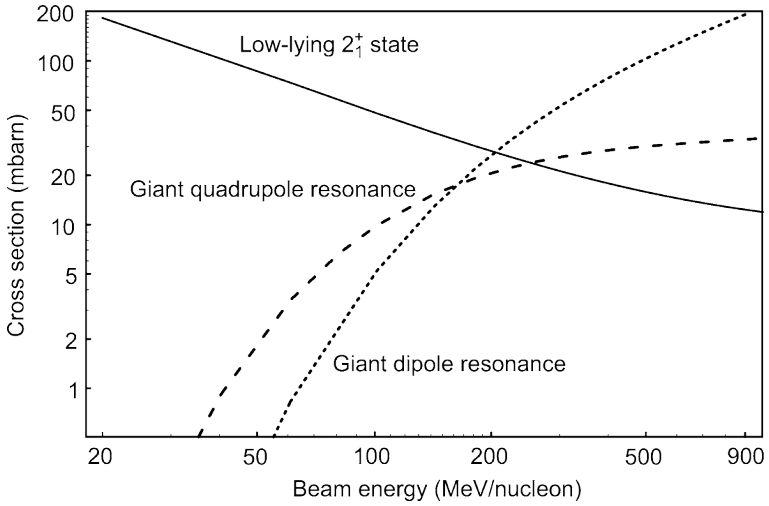

Figure 2.3: Calculated Coulomb excitation cross sections versus incident beam energy for different collective states in the ^{40}S $+^{197}$Au reaction, assuming a minimum impact parameter of $b_{min} = 16$ fm. Adapted from [86].

The beam energy dependence of the Coulomb excitation cross sections for the reaction ^{40}S+^{197}Au with a minimum impact parameter of $b_{min} = 16$ fm is shown in figure 2.3. As indicated by Eq. (6), low-lying collective states are more easily excited at low incident beam energies, while giant resonances are best studied at beam energies of several hundreds MeV. Equivalent photon numbers for multipolarities E1, M1, and E2 are plotted versus incident beam energy in figure 2.4.

2.3.3 Intermediate Energy Coulex

According to what we reported from the essential literature on Coulomb excitation, low energy collisions are well described by a semi-classical theory that considers hyperbolic trajectories and sub-barrier incident energies. In the opposite case of relativistic collisions, one assumes straight line trajectories restricting the domain of interest to high impact parameter collisions. This approach allows for a proper treatment of the relativistic effects of retardation and an approximate expression for the excitation cross section can be derived (equation 2.34).

In intermediate energy heavy ions collisions like the one subject of this work, the Lorentz factor γ is about 1.1 and relativistic effects cannot be ignored. At the same time, recoil corrections are not negligible and the straight-line parametrization is not

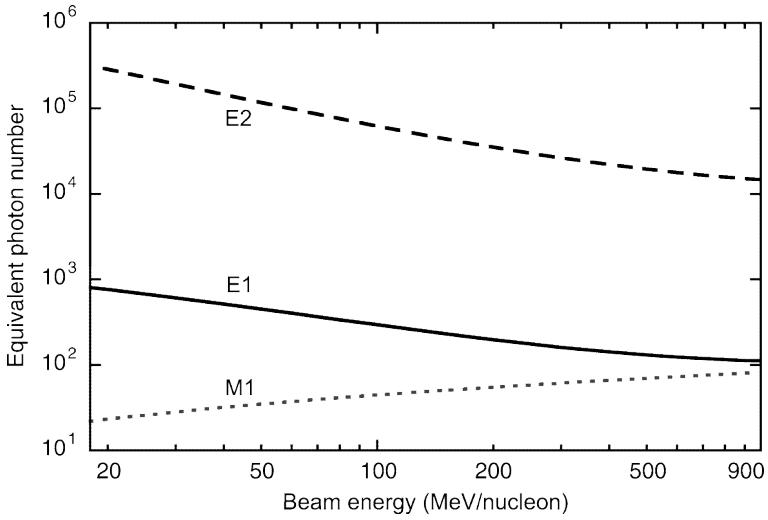

Figure 2.4: Equivalent photon numbers $n_{\pi\lambda}$ versus incident beam energy for the 2^+ state in ^{40}S (Ex = 0.89 MeV) in the ^{40}S+^{197}Au reaction, assuming a minimum impact parameter of $b_{min} = 16$ fm. Adapted from [86].

completely appropriate. The correct matching of the two approaches can be achieved considering the non relativistic limit of the semi-classical treatment expressed in the previous paragraph. In [76] it is shown that the development of equation 2.31 in the limit $v \ll c$ can reduce to the amplitude of a non-relativistic Coulomb excitation theory provided that one corrects the minimum impact parameter by:

$$b \rightarrow b + \frac{\pi a_0}{2\gamma} \tag{2.37}$$

that suggests also an improved expression for the adiabaticity parameter:

$$\xi(b) = \frac{\omega}{v\gamma}\left(b + \frac{\pi a_0}{2\gamma}\right) \tag{2.38}$$

It is important to say that at intermediate beam energies E2 excitations dominate and M1 excitations are very much suppressed as they scale with $n_{M1} \propto \beta^2 n_{E1}$ [73]. Excitation probabilities in intermediate-energy Coulomb excitation processes are small and the excitations are thus mainly one-step processes. A computer program which calculates multiple relativistic Coulomb excitation steps (and optionally nuclear excitations as well) has been developed [87] and illustrates the large suppression of multistep excitations. For example, in the ^{36}Ar +^{197}Au reaction at 50 AMeV the $(0^+ \rightarrow 2^+)$ E2 excitation is 1700 times more likely than the $(2^+ \rightarrow 4^+)$ E2 one.

2.3.4 Safe impact parameter selection

The choice of the minimum impact parameter to be considered "safe" for the disentanglement of Coulomb and nuclear interactions is not unique, several empirical "recipes" are given. One definition is the one of Wilcke et al in [88]:

$$R_{int} = C_t + C_p + 4.49 - \frac{C_p + C_t}{6.35}(\text{fm}) \tag{2.39}$$

where C_i ($i = t, p$ respectively target and projectile) is the nuclear radius for a diffuse Fermi mass distribution:

$$C_i = R_i(1 - \frac{1}{R_i^2}) \tag{2.40}$$

and R_i is the nuclear radius for a sharp mass distribution

$$R_i = 1.28A_i^{1/3} - 0.76 + 0.8A_i^{-1/3} \approx 1.21A^{1/3} \tag{2.41}$$

Thus b_{min} is required to be bigger than R_{int}. Just comparing the results, one can see that the common use of the approximation:

$$R_{int} = r_0(A_p^{1/3} + A_t^{1/3}) + 2 \text{ fm} \tag{2.42}$$

with $r_0 = 1.21$ fm is not so misleading. Considering the reaction partners of interest for this work - ^{74}Ni and ^{197}Au - the two methods give respectively the following results: 14.11 fm and 13.70 fm. According to these results, the rounded a value of 14.00 fm will be used in the experimental data analysis. Since the impact parameter is not an observable value, the selection on the experimental data is done converting b_{min} into the particle scattering angle using the relation:

$$b_{min} = \frac{a_0}{\gamma} \cot\left(\frac{\theta_{max}^{CM}}{2}\right) \tag{2.43}$$

2.4 Accuracy of Coulomb excitation at intermediate energies

Using Coulomb excitation as an experimental technique also at intermediate energy is common practice in contemporary nuclear physics [86, 89]. In particular with low intensity fast radioactive beams this is one of the few techniques that can be successfully applied to gain nuclear structure information.
Equations 2.32 and 2.34 show the direct relation connecting the observable excitation cross sections to the $B(\pi\lambda)$ values, meaning that the experimental measurement of the excitation cross section can be directly linked to important information about the structure of nuclei.
To validate the use of such a technique, Cook and collaborators [90] made a comparison between the adopted B(E2) values of several isotopes and the corresponding ones obtained in intermediate energy Coulomb excitation experiments. The main results are given in figure 2.5 (a), where the reference data set is the Raman compilation [91]. The average difference between measured and adopted values is 6% and only one data point exceeds 10%. Raman's data are given if four or more independent measures have been made for each nucleus and properly considering associated errors. It should be remarked that the reference compilation for ^{40}Ar and ^{36}Ar already contained relativistic Coulomb excitation data respectively for one out of eight and two out of eight independent measurements. Details and references to experimental data can be found in Cook's paper.
A specific analysis was carried on for ^{26}Mg where more than one data set was available for several different techniques (such as low-energy Coulomb excitation, NRF, DSAM, RDDS, and electron scattering) and where intermediate Coulomb excitation data were collected with good statistics. Results are shown in figure 2.5 (b), where the shaded area represents the uncertainty of the adopted value. The traditional transition rate measurements have an average difference of 23% from the adopted value for ^{26} Mg while the right-most data point which was obtained using intermediate-energy Coulomb excitation, deviates from the adopted value by only 3%.

From the theoretical point of view, the accuracy of the Alder-Winther formulation of the excitation cross section in the intermediate-energy domain has been questioned by Bertulani in [92]. He suggested that Coulomb distortion and retardation effects

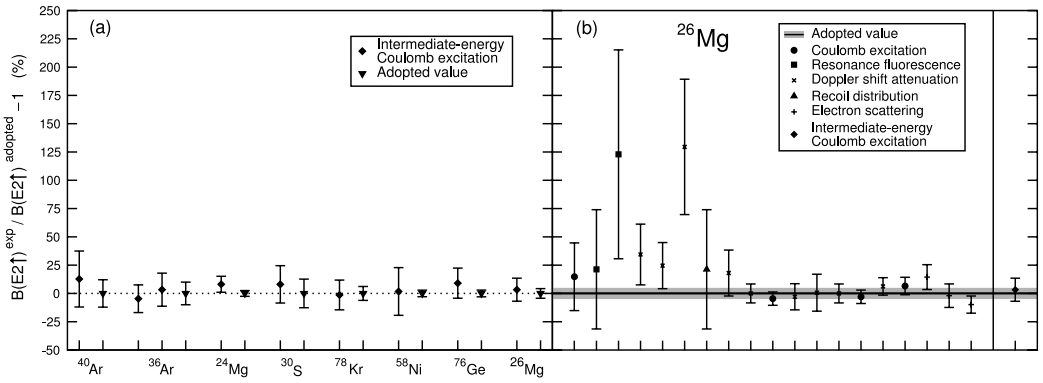

Figure 2.5: (a) Percent differences between adopted and measured $B(E2; 0^+ \rightarrow 2^+)$ transition rates for published test cases in intermediate-energy Coulomb excitation measurements. (b) Percent differences between adopted and measured $B(E2; 0^+ \rightarrow 2^+)$ transition rates for ^{26}Mg. The accuracy of several techniques is compared to the intermediate energy Coulomb excitation (right-most point). Adapted from [90].

cause discrepancies on the order of 30% between the Alder-Winther theory and a formulation in which these effects are considered. However, Scheit and collaborators [93] found that this discrepancy is due to a practical misunderstanding. Misleading factors are whether the scattering angle should be intended in the center of mass or laboratory frame and on the incident beam energy evaluation (half-target beam energy or out of target beam energy). When coherent values are used, Scheit founds excellent agreement between the Alder-Winther theory of Coulomb excitation and the formulation presented by Bertulani. Scheit and Bertulani agree that a fully relativistic approach to Coulomb excitation, which does not make the approximation of a straight-line trajectory, is most likely needed for high-precision Coulomb excitation experiments but they also suggest that uncertainties introduced by these approximations are not likely to affect the current ensemble of data from lower precision, statistics-limited Coulomb excitation experiments with exotic nuclei.

2.5 Cross sections calculation

From the excitation amplitudes derived in 2.32 one can calculate the total cross section for the excitation of the nuclear state $|f>$ starting from state $|i>$. To this purpose, two different codes have been used: the reaction code DWEIKO [94] and a specific code developed at NSCL [95]. The first one calculates nucleus-nucleus

scattering interaction cross sections at intermediate energy in the framework of the Distorted Wave Born Approximation (DWBA). The eikonal approximation is used to calculate elastic and inelastic scattering cross sections at relativistic energies (for details see [73, 94]). In case of intermediate energy collisions, the proper impact parameter scaling of equation (2.37) is used in order to account for the deflection of the particle trajectory. The second code has been developed for internal use at NSCL. Both codes have been used to calculate the cross section $\sigma_{0^+\rightarrow 2^+}$ for the first excited state of the nucleus ^{74}Ni ($E_2^+ = 1024$keV) in the reaction ^{74}Ni+^{197}Au. Half-target beam energy used is 81 AMeV and a conventional value of 100 e^{2}fm^4 has been considered for B(E2). This value will have to be scaled by the calculated/experimental cross sections ratio to extract the experimental B(E2) value. The output results are plotted in figure 2.6 as a function of the minimum impact parameter. The dash-dotted line of the figure indicates the safe impact parameter as calculated according to equation 2.39, which is the one that will be used in the data analysis.

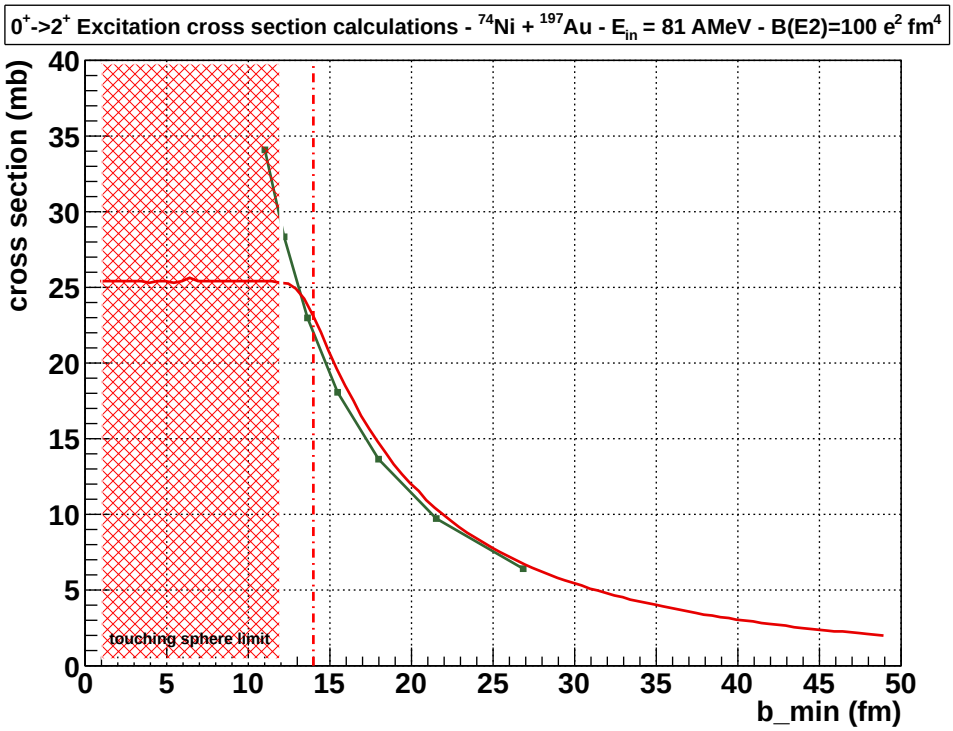

Figure 2.6: Comparison of the calculated Coulomb excitation cross sections as a function of the minimum impact parameter. The reaction is ^{74}Ni+^{197}Au at 81 AMeV, a B(E2) = 100 e^{2}fm^4 value was given. In red the results obtained with the DWEIKO code, in green the results from NSCL code. Dot-dashed red line indicates the safe impact parameter; below the touching sphere limits data are meaningless.

3

Experimental setup

This and the following chapters are dedicated to the ^{74}Ni relativistic Coulomb Excitation experiment performed at the National Superconducting Cyclotron Laboratory (*NSCL*) of the Michigan State University (*MSU*) - Experiment: *09031*, Feb 2011. In this chapter we will describe how the ^{74}Ni secondary beam is produced and focus on the experimental setup.

As already explained in paragraph 1.2, the most efficient way for producing short-lived medium-mass neutron-rich nuclei is by projectile fragmentation at relatively high energy. In the case we are considering, a primary beam of ^{86}Kr is accelerated from the Coupled Cyclotron Facility up to an energy of 140 AMeV and is directed towards a Liquid-Lithium cooled ^{9}Be primary target where fragmentation reactions produce a broad spectrum of stable and radioactive nuclei. The isotopes of interest, usually an ensemble of different species with similar mass-over-charge-state ratio, are then selected by the A1900 Fragment Separator and transported to the S3 experimental hall where the S800 spectrometer is placed. This mixture of isotopes (also called "cocktail beam") passes then through the S800 analysis line and hits the ^{197}Au secondary target (642 mg/cm^2 thick, 9 cm diameter). Here Coulomb excitation occurs

and de-excitation gamma rays are measured using the *CAESAR* 4π scintillator array. After the secondary target, forward traveling particles enter the S800 superconducting spectrometer and are measured by the S800 focal plane detectors. A sketch of the setup from the primary beam ion source to the S800 analysis line is given in figure 3.1 while the experimental setup at the secondary target position will be described in paragraph 3.4. Let us now follow the path of a sample ion describing step by step the process evolution and the main features of the setup used.

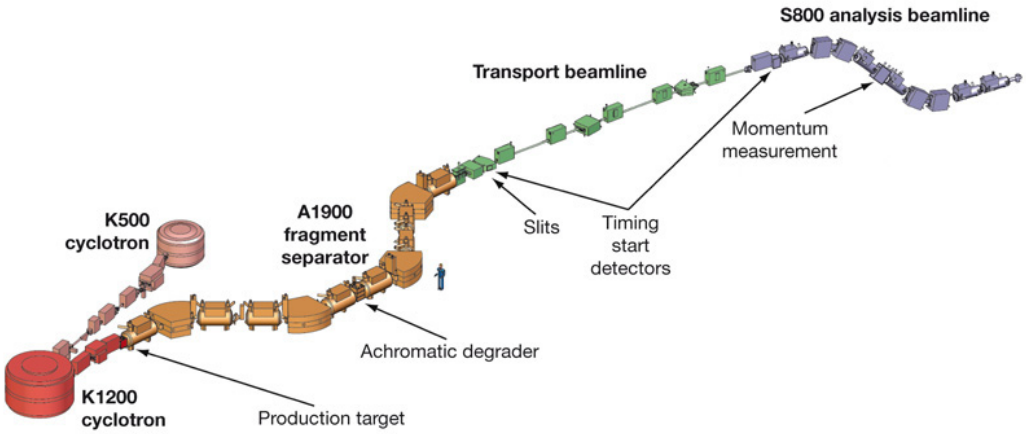

Figure 3.1: Schematic diagram of the complete NSCL facility. This overview diagram shows the major components used for the production, separation and identification of the radioactive ions. Adapted from [37].

3.1 Primary beam production and acceleration

The starting point is a ^{86}Kr neutral gas bottle. Since particle accelerators like cyclotrons use electromagnetic fields to accelerate nuclei, one has to provide an ionized atomic gas with low energy to be injected into the accelerator complex. For this purpose the NSCL facility is equipped with different types of Electron Cyclotron Resonance Ion Sources (ECR-IS) that provide charged ions with an extraction potential of about 30 kV depending on the following cyclotron injection requirement.
Due to the small production cross sections of the very exotic species, the primary beam intensity is the key feature for an efficient radioactive ion beam production. Since the acceleration process causes unavoidable beam losses, it is necessary to extract currents of the order of microamperes to obtain tens of particle nA currents at

the primary target. The SuSI ECR ion source is used ad NSCL since 2009 [96, 97]. It is a third generation fully superconducting ECR ion source and it is capable of producing high intensity beams of heavy ions like Kr^{14+}. To obtain high ionization of heavy elements with good efficiency, this device uses two 18 GHz amplifiers able to provide almost 3 kW of microwaves power. One important feature of the SuSI source is the low beam transverse emittance that allows to minimize losses at the K500 cyclotron entrance.
The K500 and K1200 are the two NSCL's superconducting cyclotrons and are used to accelerate stable beams. Since 2001 they run in coupled mode [98] mainly to provide high intensity intermediate-energy stable beams for the In-Flight radioactive ion beams production facility. Ions extracted from SuSI are accelerated to 8-15 AMeV by the K500 cyclotron that acts as an injector for the K1200 cyclotron booster. Before the injection into this last acceleration stage, ions are transported through the cyclotrons coupling line and stripped by a Carbon foil. This increases the average charge state by a factor 2.5. In our case, Kr^{14+} becomes Kr^{34+}. The higher charge state and the higher bending power of the K1200 allow to accelerate heavy ions up to 200 AMeV. The extraction/acceleration process for ^{86}Kr is summarized in table 3.1.

Step	Input	Output	Energy
ECR - Ion Source	^{86}Kr	$^{86}Kr^{14+}$	few AkeV
K500 cyclotron	$^{86}Kr^{14+}$	$^{86}Kr^{14+}$	14 AMeV
K1200 stripper	$^{86}Kr^{14+}$	$^{86}Kr^{34+}$	$<$ 14 AMeV
K1200 cyclotron	$^{86}Kr^{34+}$	$^{86}Kr^{34+}$	140 AMeV

Table 3.1: Primary beam evolution from the ECR source to the exit of the K1200 cyclotron.

3.2 Primary target

In the experiment we are considering, the primary $^{86}Kr^{34+}$ beam was accelerated to an energy of 140 AMeV with an intensity on the primary target of 25 pnA (38 pnA maximum). The 399 mg/cm^2 thick ^9Be production target is placed at the entrance of the A1900 fragment separator and a liquid Lithium cooling system provides power dissipation. This is one of the main issues when dealing with rare isotopes production:

the increase of the current, required by the low production rates, means an increase of the power that has to be dissipated by the target in order to avoid melting. Given the beam energy and intensity and the target thickness one can calculate that in our case a power of 300 W (450 W maximum) was deposited on the Be foil.
Using LISE++ [99], that implements an empirical parametrization of projectile-fragmentation cross sections (**EPAX** [100]), it is possible to calculate the expected cross sections for the setup of our interest. The results are shown in figure 3.2. This information serves as an input for the beam rate expectation in the A1900 fragment separator.

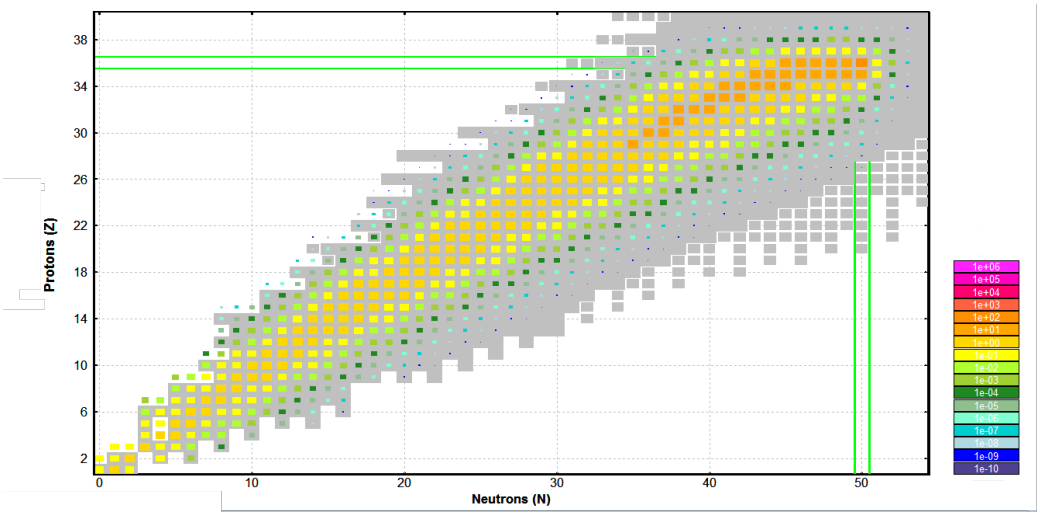

Figure 3.2: Projectile fragmentation cross sections according to EPAX parametrization. Figure was obtained using LISE++ [99].

3.3 A1900 Fragment Separator

The A1900 separator is placed between the production target and the transport line bringing selected beams to the experimental areas (see figure 3.3). The main purpose of this tool is to select the requested ions among the huge variety of stable and radioactive species produced by the fragmentation reactions in the primary

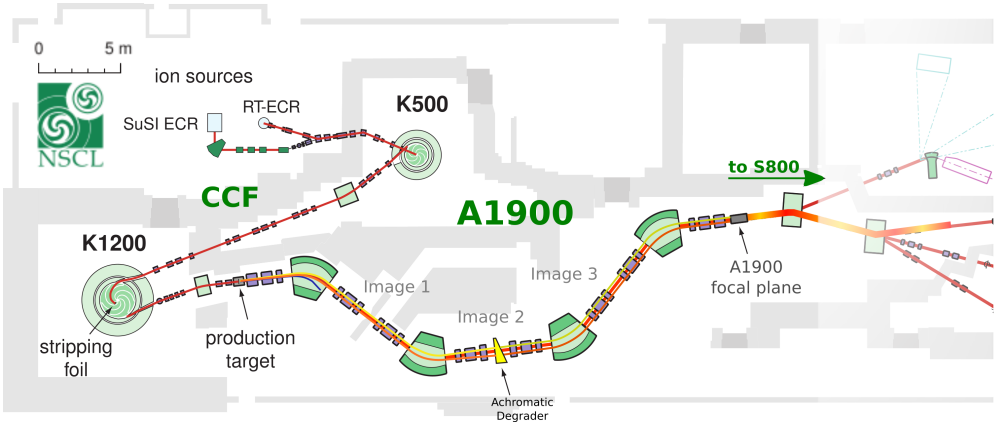

Figure 3.3: Schematic view of the Coupled Cyclotron Facility connected to the A1900 fragment separator. Adapted from [101].

target [101]. The A1900 fragment separator was commissioned in 2001 [102] and took the place of the previous A1200 device [103]. With respect to the older one, the new tool has higher angular and momentum acceptance and a better resolving power. Details can be found in table 2 of [102]. Moreover, the A1200 had collection efficiencies in the few percent range, while in selected cases efficiencies approaching 100% are possible with the new device. This can accept over 90% of a large range of projectile fragments produced at the NSCL.

The A1900 relies on superconducting iron-dominated quadrupole magnets working at the liquid Helium temperature. The setup is composed of 40 large-diameter superconducting multipole magnets and four 45° dipoles. The maximum magnetic rigidity is 6 Tm. From the optical point of view, the A1900 has three intermediate images. Access to the first image is limited by a thick steel shielding wall and contains a beam stopper. A degrader is placed at the second image along with high rate detectors and aperture plates to define the momentum acceptance. The third image occurs in a large vacuum box fitted with continuously adjustable slits to better define the beam acceptance. The focal plane of the machine is the injection point for the beam transport lines that bring the selected ensemble of beams to the experimental areas. At this position the scintillator called ”xfp“ is placed. This detector will be used in the data analysis for the incoming beam particle identification, as described later.

For fragments with relativistic velocities, a separation by mass and nuclear charge is not possible with the sole use of magnetic or electric fields. To achieve beam purification and isotopic selection, the A1900 uses a separation method based on

magnetic-rigidity analysis and energy loss degrader material.
The mixture of unreacted and fragmented ions are first filtered to select a single magnetic rigidity by the initial dispersive beam line in conjunction with an aperture at image 2. In this step also the momentum acceptance (dp/p) is defined acting on the slits aperture at image 1 and 2. Isotopic separation is then completed by passing the ions through an energy degrading "wedge", from which ions entering with a single $B\rho$ but with different atomic numbers emerge with different momenta. This is required to separate ions of different species but with similar velocities (that is quite the case of nuclear fragmentation products) and same A/q ratio. The following dispersive beam line then provides, in most cases, isotopic separation. The nature and thickness of the energy degrader, as well as the sizes of momentum apertures, are parameters that are adjusted to control the secondary beam intensity and purity. This technique has been used to provide secondary beams with E/A as low as 30 MeV. However, the best purities and yields have been obtained at significantly higher energies.
In most cases it is not possible to select one single isotopic species from the fragmentation products since these have similar masses, velocities and A/q ratio. For this reason, in several circumstances, an ensemble of secondary beams is transported to the experimental hall. This is the so-called "cocktail beam". From the point of view of the experiment, it might be necessary to tag the beam particles prior to their arrival on the secondary target measuring their mass and charge as well as their momentum.
For the experiment we are interested in, an Al wedge 240 mg/cm^2 thick was used. With this setup, the optimal beam momentum spread for the particles tagging is $dp/p = 0.5\%$ and this was used in the present experiment for the beam tuning. Due to the low production cross sections of strongly exotic ^{74}Ni, this parameter limits the beam current intensity, preventing the feasibility of a Coulomb excitation experiment in a reasonable time. For this reason the choice of running at $dp/p = 3.0\%$ was needed. However we shall see in the next chapter how this affects the incoming beam identification.
The ^{74}Ni rates predicted by the LISE++ calculation resulted a factor 6 higher than the measured one. During the experiment, an average rate of ≈ 0.7 pps was measured.

3.4 S800 spectrometer

The S800 [104] is a large acceptance, high-resolution spectrometer designed for experiments using radioactive beams produced by projectile fragmentation. It relies on superconducting magnets and it is composed of three main parts: the Analysis Line, the Spectrometer itself and the Focal Plane Detectors. A sketch of the complete device is shown in figure 3.4.

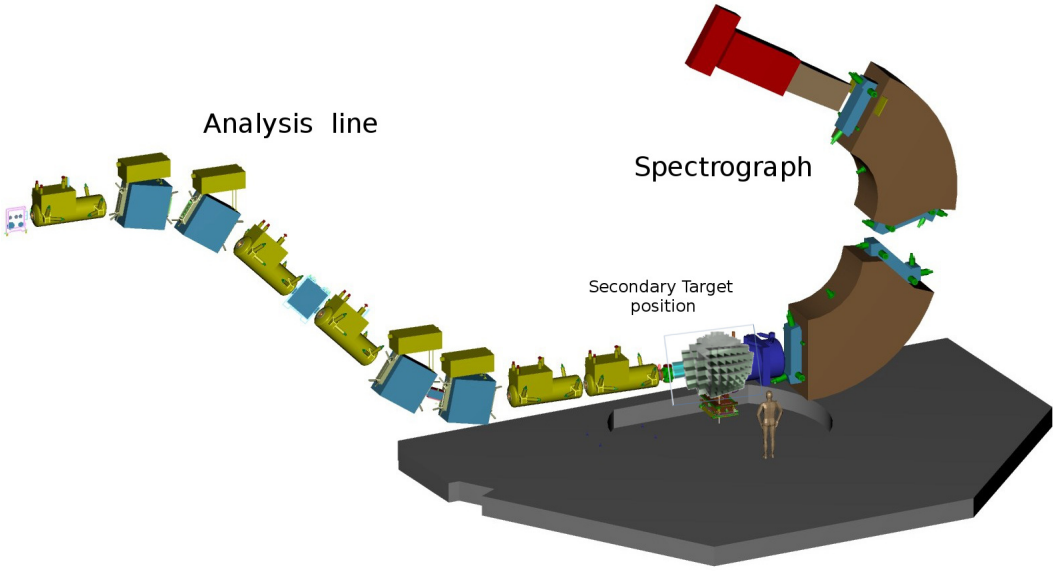

Figure 3.4: Schematic view of the S800 spectrometer: the three main components of the device are shown. The beam particles enter the analysis line on the left and hit the secondary target where the CAESAR array has been placed. Scattered particles are then analyzed by the actual S800 spectrometer and measured by the focal plane detectors. Adapted from [105].

The Analysis line is made of several optical elements used for different purposes: tuning the secondary beams on the reaction target, implementing different optical modes and, in some cases, measure the characteristics of the incoming particles. It is made of two couples of dipoles and 5 quadrupole triplets with a maximum rigidity of 4.9 Tm corresponding to 800 MeV protons. At the very beginning of the Analysis line, at the "Object" position, a 125 μm (or thicker) plastic scintillator is placed across the beam path. This is called the "Object scintillator" (obj) and timing information from this device will be used in the data analysis for the incoming particle identification.

The actual S800 spectrometer part consists of a high-resolution and high-acceptance spectrometer made of two superconducting dipoles spanning from the target position to the focal plane. It has an angular acceptance of ± 5 deg in the non dispersive and of ± 3.5 deg in the dispersive directions, totaling a solid angle of 20 msr. The maximum rigidity of the magnets is 4 Tm and the momentum acceptance is about $\pm 3\%$. Depending on the experimental setup, the performance can vary. Typical resolution for radioactive beams is 1 part in 2000 in energy and 10 mrad in scattering angle but the nominal resolution is much higher ($1/10^4$) and requires to use very small beam spots ($\approx$ 0.5 mm in diameter). As discussed in [106], from the optical point of view the S800 can be operated in three different modes:

- in the **dispersion matched mode** the momentum spread of the beam at the object position is canceled at the focal plane but this means that the beam momentum is dispersed at the target position. In this mode the whole S800 (analysis line and spectrometer) is achromatic.

- in the **focused mode** the beam is focused on the target and the momentum is spread at the focal plane. This mode allows large momentum acceptance.

- **monochromatic mode**. This mode requires the fabrication of a mono-energetic wedge to be placed at the intermediate image and is used to produce very low energy beams.

In the present experiment the focused mode was used since it has been necessary to run at large momentum acceptance. In this operating mode, the cocktail beam coming from the A1900 and running along all the transport line is focused at the object position. From here the beam is transported along the analysis line of the S800 and reaches the target in a position very close to the pivot point of the spectrometer. After the target a quadrupole focusing doublet is used to re-focus the scattered and non-scattered particles and inject them into the spectrometer dipoles. Here the ions are dispersed along one direction according to their A/q ratio. At the focal plane of this device a set of detectors is used for energy measurement and track reconstruction. The tuning of the magnetic field of the dipoles allows to center the reactions products of interest on the focal plane, thus selecting the desired reactions channels. In the experiment we are discussing, the main interest is to measure ^{74}Ni ions exiting the

target with a velocity $\beta \approx 0.36$, this means $B\rho \approx 3.2$ Tm. In the final measurement setting a $B\rho$ value of 3.19 Tm was used.

3.5 S800 Focal Plane Detectors

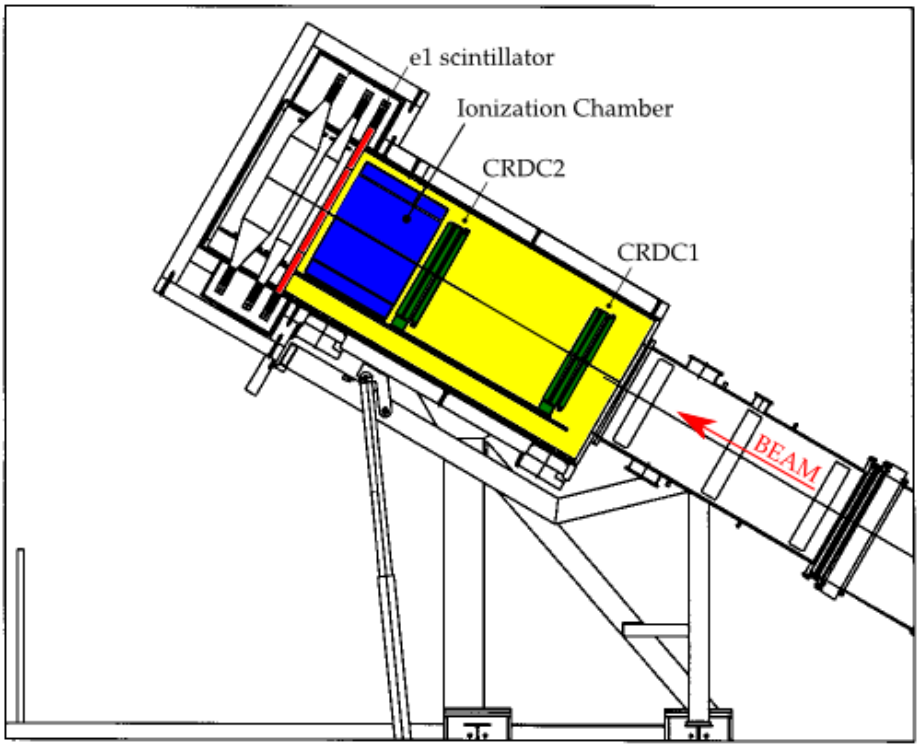

Figure 3.5: Schematic view of the S800 focal plane detectors arrangement. Particles dispersed by the S800 dipoles enter the gas volume (in yellow) from the right side of the plot. After passing through the 2 CRDC detectors, the ions encounter the Ionization Chamber (in blue) and the e1 scintillator (in red). Adapted from [107].

The S800 setup is equipped with three different types of detectors placed at the focal plane of the spectrometer [107]. These have to be properly optimized to achieve high-resolution performance exploiting the high optical resolution of the spectrometer itself. First of all, a couple of Cathode Readout Drift Chambers (CRDC) is used to measure the particle x-y position. Afterward, a segmented ionization chamber serves for the ions energy measurement acting as a ΔE detector. The last step is made of three thick plastic scintillators used for the residual energy measurement, timing

measurement and as the focal plane trigger. Figure 3.5 shows the arrangement of the detectors at the focal plane of the S800 setup.

3.5.1 The Cathode Readout Drift Chambers

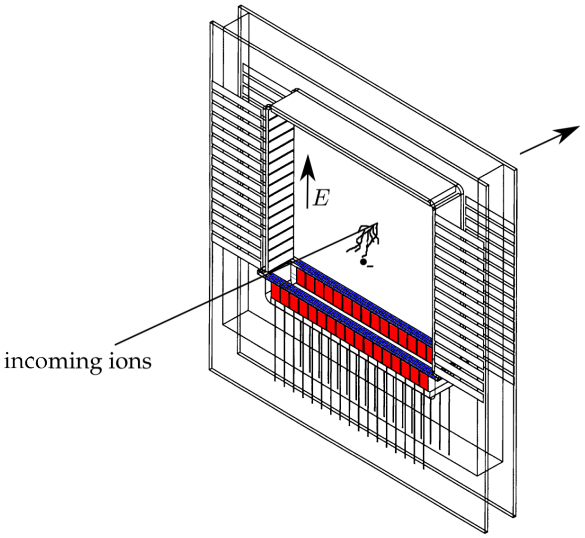

Figure 3.6: Schematic view of one CRDC detector. The particle approaches the gas volume along the perpendicular direction with respect to the Electric field. Blue color represents the anode wire, red squares are the cathode pads. Adapted from [107].

The working principle of the Cathode Readout Drift Chambers is similar to the one of a single wire drift detector. As shown if figure 3.6, each CRDC is a box surrounding a gas volume where a drift voltage is applied in the vertical direction. The gas used is a mixture of 80%CF_4 and 20%C_4H_{10} operated at a pressure of 40 Torr. On the bottom side of the detector the anode wire is surrounded by 224 segmented pads (inductive cathodes) used to get the position along the wire. Each pad is 2.54 mm wide along the horizontal direction. Each CRDC has an active area of 59 cm $\times$ 30 cm (x and y directions respectively) and an active pitch depth of 1.5 cm. The x coordinate corresponds to the dispersive direction of the spectrometer's magnetic field.

Charged ions approach the gas volume perpendicularly with respect to the box and ionize the gas. The freed electrons drift, due to the electric field, towards the anode wire and induce image charges on the close standing cathode pads. Signals from each

pad are properly amplified and recorded independently using LeCroy 2249 QDCs. Several methods for determining the x coordinate of the particle trajectory have been tested [107]: simple center of gravity of all the pads, the center of gravity of several pads around the peak and a Gaussian fit of the charge distribution were compared. The fit of the peak was found to be the best method, allowing to reach the 0.5 mm resolution required to fully exploit the resolving power of the spectrometer.
The y coordinate is obtained measuring the electrons drift time inside the CRDC: the start signal is given by the arrival of the particle in the e1 scintillator, while the stop is the signal induced at the anode by the drifted electrons. The calibration of the x and y coordinates will be discussed in the next chapter.

3.5.2 Particle trajectory reconstruction

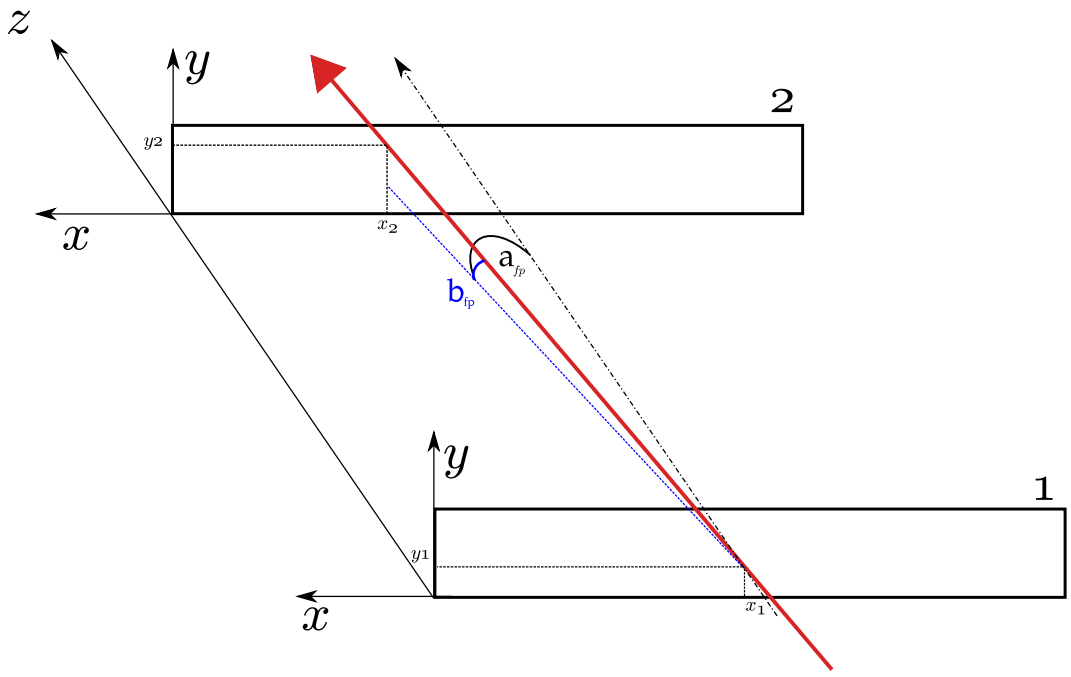

Figure 3.7: Trajectory reconstruction at the focal plane. The positions measured by the CRDCs allow to calculate the angles at the focal plane in the dispersive and non-dispersive directions of the spectrometer (a_{ta}, b_{ta} respectively).

Two CRDC detectors are housed in the same gas volume and placed 1 m apart in the beam direction (z) (see figure 3.5).
Combining the (x_1, y_1) and (x_2, y_2) position information measured by the two CRDCs

it is possible to reconstruct the particle trajectory at the focal plane. As shown in figure 3.7, one can define the dispersive and non-dispersive focal plane angles respectively as:

$$a_{fp} = \arctan\left[\frac{x_2 - x_1}{\Delta z}\right] \tag{3.1}$$

$$b_{fp} = \arctan\left[\frac{y_2 - y_1}{\Delta z}\right] \tag{3.2}$$

where Δz= 1000 mm is the gap between the two detectors and is fixed. Using as focal plane the "image" of CRDC1, the positions at the focal plane (x_{fp}, y_{fp}) coincide with the positions (x_1, y_1) measured by CRDC1 itself. Since the optics of the spectrometer is known, given the $B\rho$ parameters, Z and A of the particle and the measured trajectory at the focal plane, it is possible to reconstruct the particle trajectory at the target position using the inverse map $\mathcal{S}^{-1}$ of the S800. This can be obtained using the COSY-Infinity code as described in [108]:

$$\begin{pmatrix} a_{ta} \\ y_{ta} \\ b_{ta} \\ d_{ta} \end{pmatrix} = \mathcal{S}^{-1} \begin{pmatrix} x_{fp} \\ a_{fp} \\ y_{fp} \\ b_{fp} \end{pmatrix} \tag{3.3}$$

Here a_{ta} and b_{ta} are respectively the dispersive and non-dispersive angles reconstructed at the target, y_{ta} is the reconstructed y position at the target and d_{ta} is the fractional deviation in kinetic energy of the particle (E) from the kinetic energy of the same particle taking the central path through the spectrograph (E_0):

$$d_{ta} = \frac{E - E_0}{E_0} \tag{3.4}$$

Given the experimental parameters and the ion of interest, the inverse map can be automatically calculated and retrieved from [105]. The dispersive and non-dispersive angles reconstructed at the target can be used to calculate the laboratory scattering angles θ and ϕ:

$$\theta = \arcsin\sqrt{\sin^2(a_{ta}) + \sin^2(b_{ta})} \tag{3.5}$$

$$\phi = \begin{cases} \arctan\left[\frac{\sin(a_{ta})}{\sin(b_{ta})}\right] & \text{if } \sin(a_{ta}) > 0,\ \sin(b_{ta}) > 0 \\ \pi - \arctan\left[\frac{\sin(a_{ta})}{|\sin(b_{ta})|}\right] & \text{if } \sin(a_{ta}) < 0,\ \sin(b_{ta}) > 0 \\ 2\pi - \arctan\left[\frac{|\sin(a_{ta})|}{\sin(b_{ta})}\right] & \text{if } \sin(a_{ta}) > 0,\ \sin(b_{ta}) < 0 \\ 0 & \text{if } \sin(a_{ta}) = 0,\ \sin(b_{ta}) = 0 \end{cases} \tag{3.6}$$

3.5.3 Ionization chamber

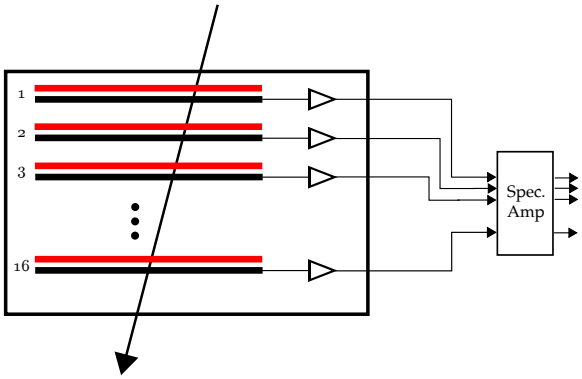

Figure 3.8: Schematic view of the Ionization Chamber: 16 anode-cathode pairs are placed in the same gas volume crossing the particle trajectory. Each pair has a dedicated electronic readout channel. Figure adapted from [107].

In an airtight gas volume with respect to the CRDCs one, the ionization chamber uses 500 Torr of P10 gas (90% Ar, 10% CH_4) to measure the ion energy. This detector is segmented into 16 anode/cathode pairs placed perpendicularly with respect to the ion path. Figure 3.8 schematically shows the geometry of this detector: the ionization electrons are collected by the anode foils and positively charged ions are collected by the corresponding cathodes. Each channel has a small size pre-amplifier placed inside the gas chamber and is read out independently. The sum of the 16 integrated signals gives the energy loss in the ionization chamber.

3.5.4 Focal plane scintillator

A large area (30 × 59cm), few millimeters thick (3 mm) plastic scintillator is closely coupled with the ionization chamber. This is called ”e1“ scintillator and provides two signals coming from two photomultipliers placed at its top and bottom. These signals

are used to obtain position, timing and energy information. Due to the fast response of this detector it is used for three different tasks:

- as a time reference for the electrons drift time in the CRDCs;
- it is the reference for time of flight measurement of the particles along the S800 analysis line (obj scintillator) and from the A1900 focal plane (xfp scintillator);
- it is the main trigger source of the S800 focal plane detectors.

3.6 CAESAR array

CAESAR [109] is an array of 192 CsI(Na) thick scintillators specifically designed for in beam γ-ray spectroscopy in the intermediate energy domain. This is comparable to the most common NaI(Tl) in terms of energy resolution, timing performances and costs but it has a 30% higher stopping power for γ-rays. In situations like the one of our interest, where the ^{74}Ni beam intensity is extremely low, the gamma detection efficiency becomes a crucial parameter for the feasibility of the experiment. Although High-Purity Germanium (HPGe) is still the material of choice for the construction of γ-ray spectrometers, the efficiency performance and angular coverage reachable with an array of scintillators triggered the development of the setup that we will describe in the following.
Due to the typical velocities of the reaction recoils ($\beta \geq 0.3$), the de-excitation gamma rays are Doppler-shifted with respect to their original energy. For this reason one has to perform Doppler correction in order to obtain the proper de-excitation spectrum. In the design of CAESAR the goals of more than 95% solid angle coverage and a total 40% efficiency for 1 MeV γ-rays were achieved. Intrinsic energy resolution is $\approx$ 7% FWHM for 1 MeV photons. Considering the solid angle subtended by each crystal, the effective energy resolution in an in-beam experiment, which includes the effects of Doppler broadening, reduces to $\approx$ 10%. Given these values, one could discuss where and how an appreciable gain in global detection efficiency and angular coverage is worth despite the energy resolution. For the present experiment the answer is obvious, given the extremely reduced number of measured ^{74}Ni de-excitation photons (less than 100) that would reduce by a factor ten using standard HPGe detectors. For the sake of completeness one has to say that the advent of the new generation of

gamma-ray tracking arrays like AGATA [110] and GRETINA [111] has completely altered the panorama offering extreme energy resolution combined with good efficiency. Costs and complexity are however orders of magnitude far from the setup we are describing.

Moreover, during the CAESAR design study the possibility to use $LaBr_3$:Ce scintillating materials was also investigated. This solution would have led to a higher detection efficiency and superior timing performances maintaining the same quality for in beam γ-ray energy resolution. The unavoidable drawback would have been the cost of such detectors to achieve the required CAESAR angular coverage and granularity.

The geometry of the array was decided according to several constraints that a GEANT4 simulation helped to define. First of all the γ-ray detection efficiency had to be maximized and particular care had to be put at the forward angles where, due to the Lorentz boost, the angular distribution is expected to peak. Moreover, geometrical space limitations, the required granularity and the possibility to couple the detectors to commercially available photomultiplier tubes have been taken into account.

The final choice was to arrange 192 rectangular shaped detectors in 10 rings (A..J) perpendicular to the beam axis. Two different sizes of detectors where used. Size 1 is 3.13 $\times$ 3.13 $\times$ 3 inches, while size two is 2.13 $\times$ 2.13 $\times$ 4 inches. Their arrangement in rings is reported in table 3.2, while a geometrical sketch is shown in figure 3.9.

Ring	Number of detectors	det. size type
A	10	1
B	14	1
C	24	2
D	24	2
E	24	2
F	24	2
G	24	2
H	24	2
I	14	1
J	10	1

Table 3.2: CAESAR detectors arrangement.

The hygroscopic CsI(Na) scintillation crystals are placed in an aluminum housing with a 1 mm wall thickness. A reflective material fills the 1.5 mm gap between the crystal and the wall of the aluminum housing. The latter is sealed with a borosilicate window through which the photomultiplier is coupled.
The spectroscopy photomultiplier tubes R1306 and R1307 from Hamamatsu are used for the two different crystal sizes. A passive voltage divider board distributes the externally applied high voltage to the dynodes. Since CAESAR has to operate close to the S800 spectrometer, in an area where the magnetic fringe fields of the S800 entrance quadrupole are not completely shielded, a proper shielding for magnetic fields had be implemented. This is done by covering the photomultiplier tubes, inside their housing, with multiple layers of μ-metal. It was verified that this shielding provides proper operation up to 2-3 Tm external field. It was also measured that already 0.5 Tm of unshielded magnetic fields affect the output pulse height.
The photomultiplier tube with magnetic shielding and Al housing fits within the

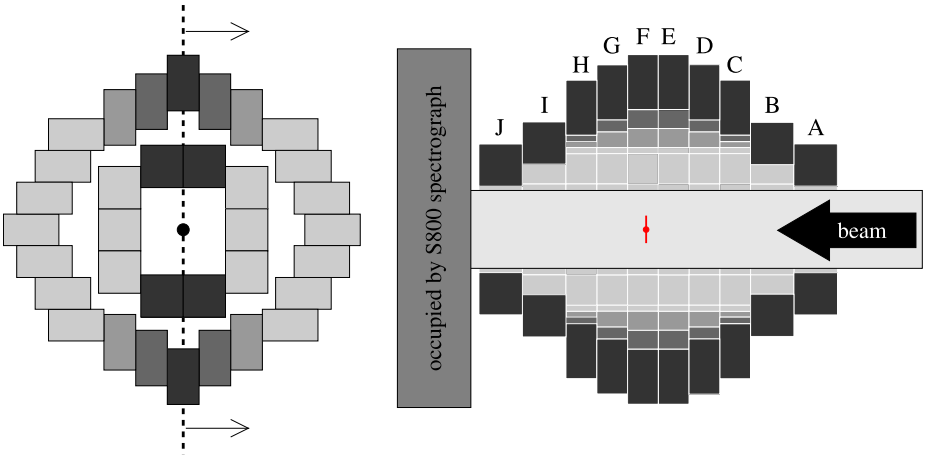

Figure 3.9: CAESAR geometry. Left panel shows the cross-sectional view of the CAESAR array along the beam direction for rings J and F. Right panel shows the cross-sectional view parallel to the beam axis of the entire setup. Adapted from [109].

shape of the crystal enclosure, thus detectors can be placed close to each other without any significant gap in between. Figure 3.10 shows a picture of the final assembly, while a picture of the complete CAESAR setup mounted at the secondary target position is shown in figure 3.11.
Each detector has a dedicated power supply line that provides positive high voltage to the respective photomultiplier. The high voltage tuning is used both to match the

output signals amplitude and to set the dynamic range of the setup. A broad interval can be spanned going from 1 to several tens of MeV of full scale energy. In Coulomb excitation experiments with fast beams, typically a dynamic range of 8 MeV is used.

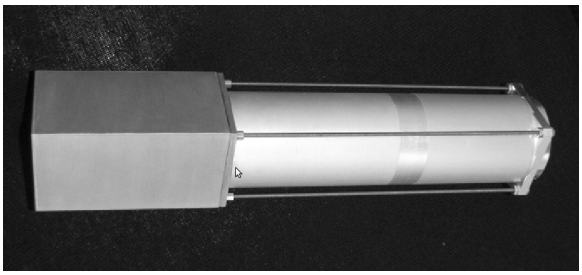

Figure 3.10: Picture of the final assembly of one CAESAR detector. Adapted from [109].

3.6.1 CAESAR Electronics

A specific high speed data acquisition system has been developed for the CAESAR signals readout. A scheme of the electronics is reported in figure 3.12. The core of the system are the LeCroy *Fast Encoding Readout ADCs* (FERA) 4300 CAMAC modules [112]. Raw signals coming from the detectors (PMTs output) are split into two branches: the **energy** and the **time** branch. This is done using a dedicated module (PicoSystem splitter-and-amplifier) that performs a fixed gain fast amplification and provides two outputs for each input.

The **energy branch** signals are sent to custom shaping amplifiers with variable gain and fixed shaping time (4 μs). The amplified signals are then delivered to the inputs of the 4300B FERA QDCs that are operated effectively as peak sensing ADCs. This is done integrating the long-tail-shaped-signals coming from the amplifiers in a 25 ns time gate applied at the maximum of the signal. The integration gate is handled in a common way by the FERA 4301 driver and depends on the S800 trigger logic.

The **time branch** signals are sent instead to 12 RIS 13080 Constant Fraction Discriminator modules. Each module handles 16 channels and is operated in the two-thresholds mode. The lower threshold of the CFD is used to decide whether to accept or not a signal, while the higher threshold is used to select higher energy events for

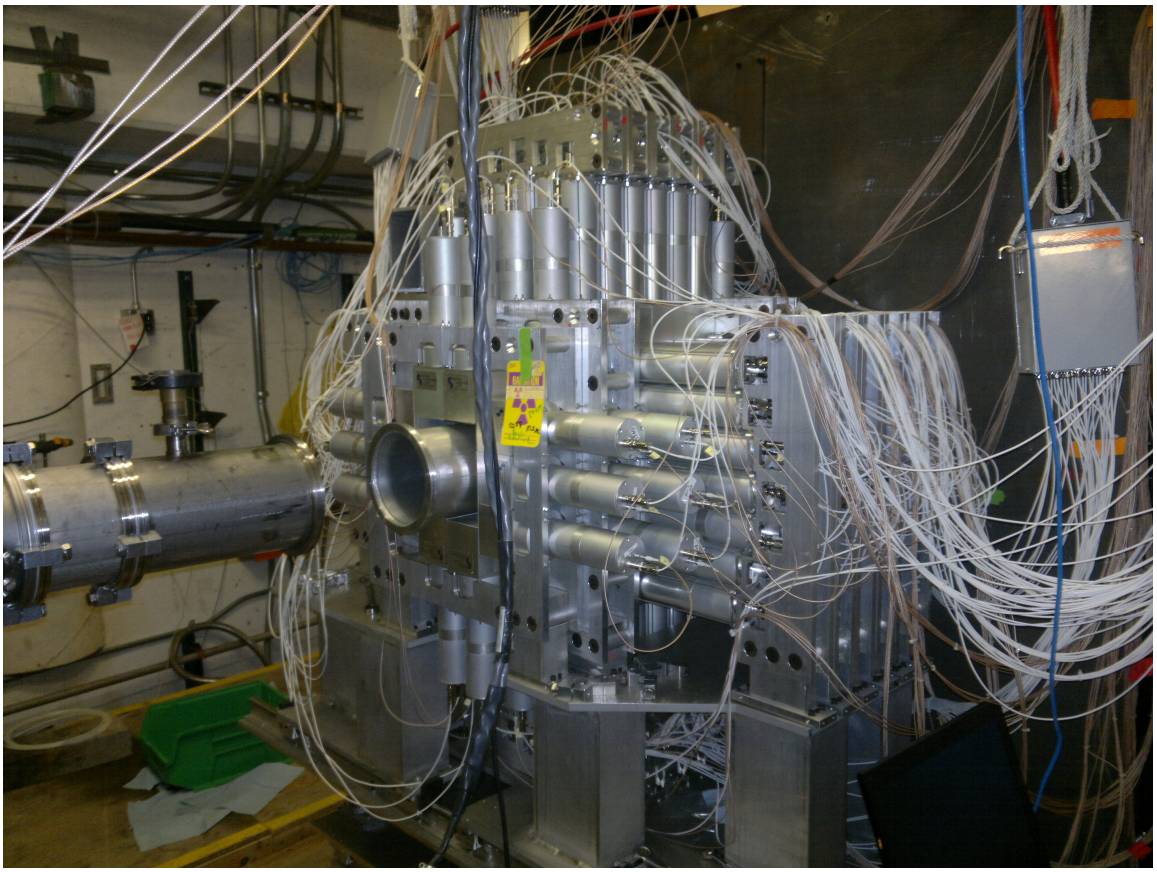

Figure 3.11: A photograph of the CAESAR array mounted at the pivot point of the S800 spectrometer.

the trigger request. The global CAESAR trigger is then the OR of the lower threshold CFD outputs validated by the OR of the higher ones. This means that each CAESAR event will contain at least one detector with a signal exceeding the higher threshold and all the signals exceeding the lower one. The single output of each CFD channel is then delayed by 500 ns using cable ribbons and, after, is acquired by the 4303 Time to FERA Converters (TFC). Those modules are operated in common start mode where the start is given by the master trigger and the stop is the individual discriminated signal. The output of the TFCs is a NIM signal, the width of which being proportional to the measured time. This is successively acquired using the 4300B FERA QDCs with a 500 ns fixed integration gate.

The data recorded by the energy-branch and time-branch QDCs are readout from the FERA drivers. This is done using two FPGA modules that provide the interface between the FERA world and a VME Crate where the NSCL standard acquisition

system has access. As already stated, the main CAESAR trigger is evaluated using the CFDs OR. Since this device is operated in conjunction with the S800, the real trigger for the FERA modules comes from the trigger module of that setup: the trigger request is sent from CAESAR to the S800 trigger logic and an evaluated master trigger is received back. The latter is the actual CAESAR trigger.

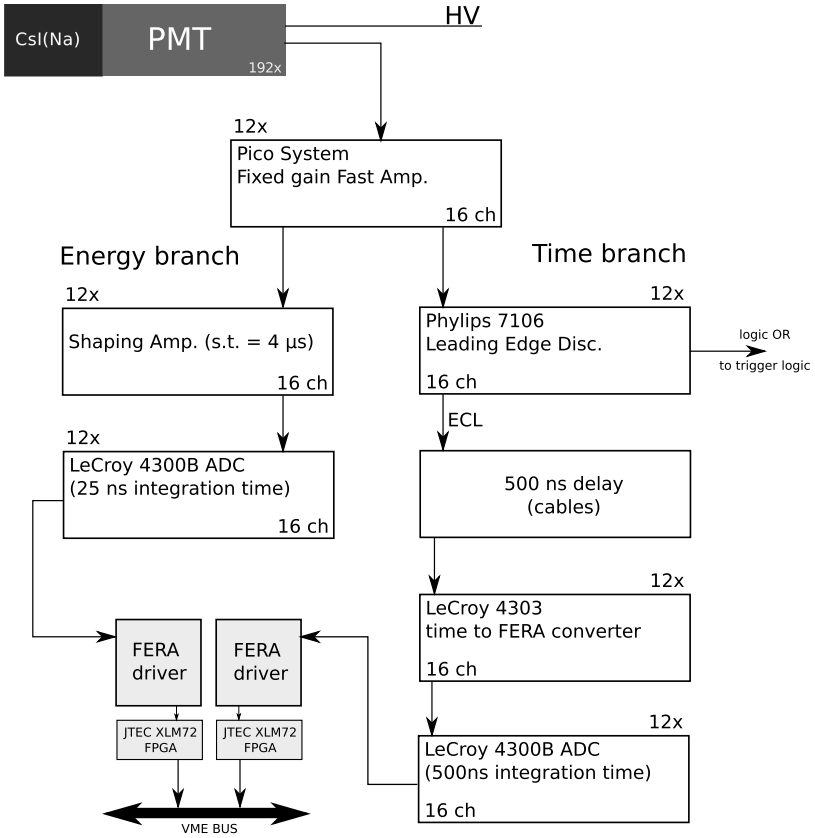

Figure 3.12: CAESAR readout electronics scheme.

3.6.2 Add-back procedure

At the γ-ray energies considered in the present work, Compton scattering is the dominant effect (for a detailed description of the interactions of photons with matter in this energy domain see [113–115]). Even using thick scintillation crystals, there is a non-zero probability that Compton scattered γ-rays escape the active volume of the detector, releasing only part of their initial energy. Looking at a single-detector energy spectrum, this effect produces the so-called "Compton Continuum". In the

limit of single Compton scattering, the Compton continuum extends from zero up to $\approx E_\gamma$-250 keV, which can be estimated considering a backward scattering in the well known Compton scattering formula:

$$E'_\gamma = \frac{E_\gamma}{1 + \frac{E_\gamma}{m_e c^2}(1 - \cos(\theta))} \tag{3.7}$$

where E_γ and E'_γ are respectively the incident and scattered photon energies, θ is the laboratory scattering angle and $m_e c^2$ is the rest mass of the electron (0.511 MeV/c^2). Multiple scatterings modify the shape of the continuum, which practically extends up to the full-energy peak. If the scattered photon escapes from the detector, the information about the total incoming energy is lost and the photo-peak efficiency is therefore affected.
One of the techniques that can be applied in order to recover part of these events is the *nearest neighbor add-back*. The idea is to see if the escaping photon has released energy in one of the detectors neighboring the one that was first hit, in order to reconstruct the initial total energy by summing the partial contributions. From the practical point of view, given the geometry of the array and the size of the scintillators, it is a reasonable approximation to limit the discussion to the case where no more than two neighboring detectors were hit. The add-back procedure is computed as follows:

- browse all the detectors and select those that have been hit;
- consider each selected hits and count how many of its neighbors were also hit. This can give three results different:

  n0: No neighbors were hit: the present hit is taken as it is;

  n1: One neighbor was hit: the energy from the two detectors is summed up and assigned to the detector with the higher energy deposit;

  ng: More than one neighbor was hit: discard the hits.

- The energy spectrum is filled with the n0 (raw) and n1 (reconstructed) hits.

The effect of the add-back procedure applied to a ^{88}Y calibration source is clearly visible in figure 3.13. The calibrated and integrated CAESAR spectrum shown are obtained with and without the use of the routine: the add-back is clearly reducing

the Compton background and increasing the photo-peak efficiency. The efficiency gain has been quantified using activity-calibrated sources and will be discussed in the next paragraph. It is important to underline that the experimental conditions of a calibration run are quite different with respect to the in-beam case where a huge atomic background can affect the quality of the events reconstruction. In the next chapter we will show how this contamination affects the data analysis of the present work.

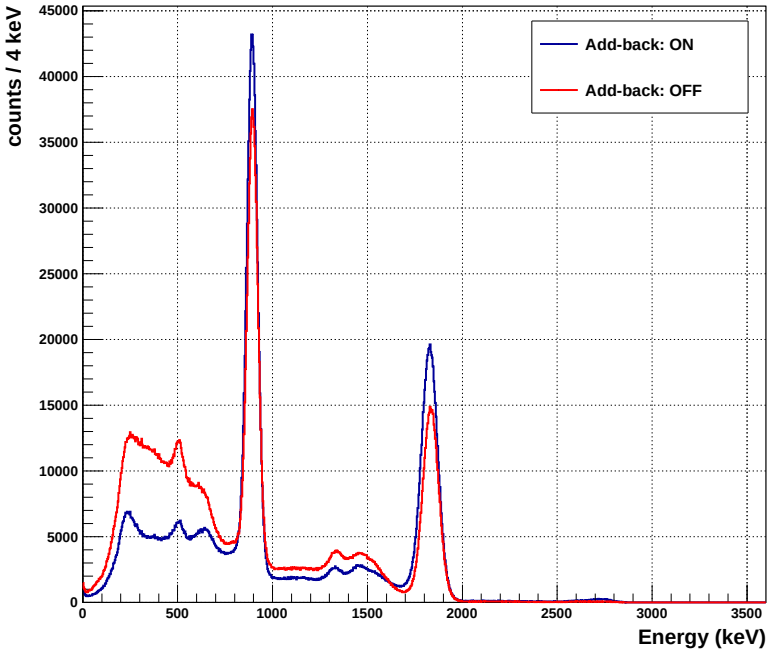

Figure 3.13: Measured γ-ray spectrum of a ^{88}Y source. The red line is the sum of the calibrated single-detector spectra for the 192 scintillators; the blue line shows the gain in photo-peak efficiency after the add-back procedure has been applied.

3.6.3 Performance of CAESAR

CAESAR was commissioned in 2009 and the performance obtained both with stationary sources and in a Coulomb excitation experiment are reported in [109]. Figure 3.14 shows the measured global resolution in terms of peak FWHM. Data obtained

from in-beam experiments and using stationary sources are compared to show how the Doppler reconstruction of the γ-rays emitted by a fast moving source (β=0.37) affects the effective resolution. In figure 3.15 one can see the gain in efficiency that can be achieved when applying the add-back procedure to the data measured with stationary sources. For the $\approx$ 1 MeV photons of interest in the present work, the expected full-energy peak efficiency is $\approx$ 30% if no add-back is performed and $\approx$ 35% using add-back. Since the velocity of the scattered ^{74}Ni will be close to the one of the reference ($\beta \approx 0.36$), the expected in-beam resolution is about 10% FWHM. These parameters have been re-measured while calibrating CAESAR for the experiment and while setting the energy thresholds. The latter have been kept quite high ($\approx$ 300 keV) since the energy region of interest is at 1 MeV and typical Coulomb excitation experiments are affected by a huge low energy background due to atomic processes and Bremsstrahlung radiation. Energy thresholds are strongly related to the actual detection efficiency, to quantify this effects a GEANT4 simulation was developed [116] and will be used for the data analysis.

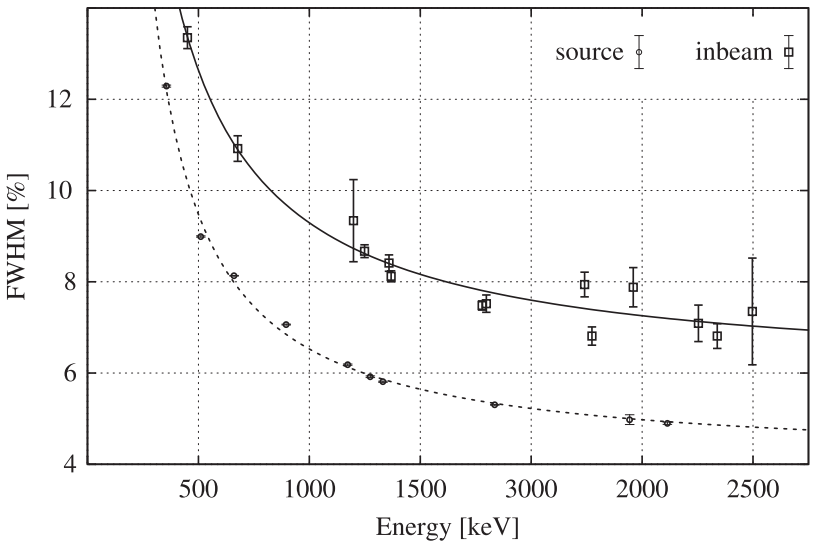

Figure 3.14: In-beam and intrinsic energy resolution (FWHM) as measured from standard calibration sources and in an intermediate-energy Coulomb excitation experiment. The in-beam part was obtained after Doppler reconstruction of the γ-rays emitted by sources with velocity $\beta = 0.35$. Adapted from [109].

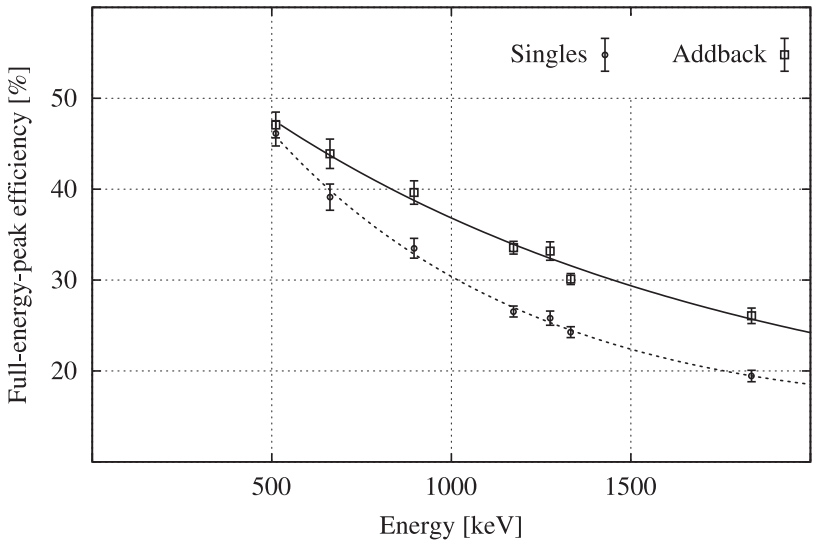

Figure 3.15: Absolute full-energy-peak efficiency of CAESAR measured with calibration sources. With and without add-back results are compared. Adapted from [109].

4

Data Analysis

In this chapter, the data analysis of experiment 09031 performed at NSCL is reported. The experimental setup was described in chapter 3, here we will focus on the detector calibration and on the following data analysis.
The final goal is to extract the Coulomb excitation cross section for the first 2^+ state of the ^{74}Ni nucleus using the secondary reaction ^{74}Ni + ^{197}Au at ≈ 90 AMeV.
The experimental cross section is given by:

$$\sigma_{0^+\rightarrow 2^+} = \frac{N^{\gamma}_{2^+\rightarrow 0^+}}{N_B \quad N_T} \tag{4.1}$$

where the main ingredients are:

- $N^{\gamma}_{2^+\rightarrow 0^+}$: number of de-excitation γ-rays;
- N_B: number of ^{74}Ni projectiles approaching the secondary target and reaching the S800 focal plane without undergoing nuclear reactions;
- N_T: areal density of the ^{197}Au target.

In the following we will show how these values have been obtained from the experimental data.
An important part of the work was performed using a custom NSCL software developed in the ROOT [117] framework by K. Wimmer [118]. This code provides three main tools. The first allows to unpack the raw data from the NSCL binary format to non-calibrated ROOT Trees. The second contains some automated or semi-automated calibration procedures and the third allows to apply the calibration factors, producing calibrated ROOT Trees. An event by event analysis was later performed on these data to obtain the required cross section.
We will first describe the calibration of the S800 focal plane detectors and of CAESAR detectors. After this, the particle identification process and the particles trajectory reconstruction will be discussed. Using these information, the γ-ray spectrum will be used to extract the cross section value.

4.1 Focal plane detectors calibration

The calibration of the Focal plane detectors has to be performed keeping in mind what kind of information is needed for the following analysis.
The **focal plane scintillator** will only be used as a time reference for the Time Of Flight of the ions, therefore no absolute calibration is needed.
The **ionization chamber** provides the ΔE information for the particle identification at the focal plane (see par. 4.5), this value is obtained summing the 16 signals coming from the different segments of the detector. Even if an absolute energy calibration of the ΔE is not needed, a proper gain match of the 16 channels has to be performed before the signals can be added. The left panel of figure 4.1 shows the raw energy-loss spectra as a function of the segment number. Segment 1 was arbitrary chosen as a reference and a linear function was used to shift the data of the other segments.

The calibration parameters for each segment are obtained selecting different isotopes on a roughly calibrated particle identification spectrum and fitting the particle gated energy projections. As it can be seen in figure 4.2, since the energy loss in the gas differs according to the atomic species, each particle-gate provides one calibration point. The linear regression of the measured centroids of the distributions with respect to the reference values gives the parameters for the linear segment matching.

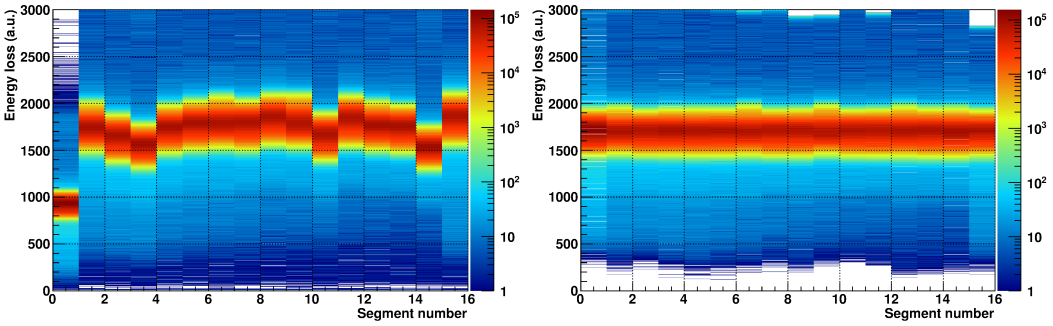

Figure 4.1: Gain matching procedure: the two panels show the energy loss measured by the Ion Chamber as a function of the segment number before (left) and after (right) the gain matching procedure.

This procedure is repeated for all the segments and the result is shown in the right panel of figure 4.1. At this point the corrected values can be summed up to obtain the total energy loss in the ionization chamber.

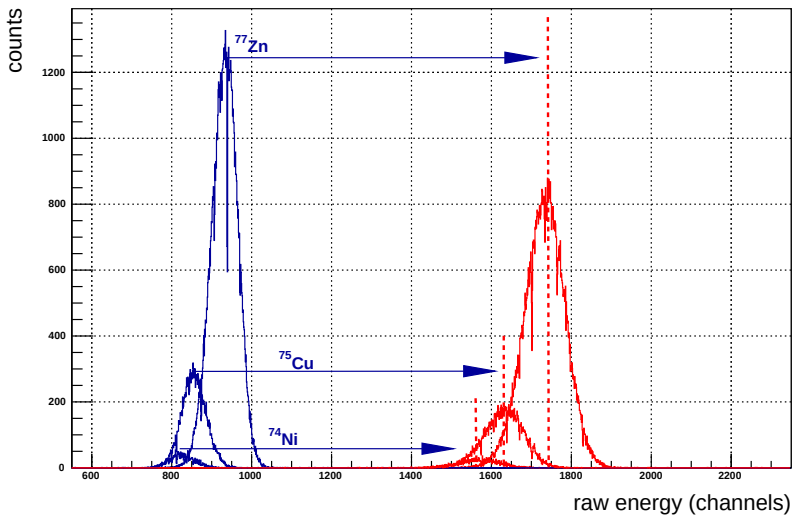

Figure 4.2: Ionization chamber equalization procedure. The energy loss peaks gated on different isotopes for the segment to be aligned (blue) are shifted on the reference one (red) according to a linear calibration.

The **CRDC** detectors are processed in two steps. First a gain matching of the single-pad signals is needed. The procedure is equivalent to what was shown for the Ionization Chamber. Once this is done, the absolute position calibration has to be

obtained. Since the CRDCs will be used for the particle trajectory reconstruction at the focal plane (see par. 3.5.2), an absolute calibration of the x and y variables of the two detectors is needed. This is done masking each CRDC with a thick Tungsten shielding with several holes at known (x, y) position. The geometry of the mask used is shown in figure 4.3. Few minutes of dedicated beam-runs have to be performed for each CRDC and this method is usually referred to as the *Mask Calibration*. The procedure has to be periodically repeated during the experiment to account for long-term drifts due to gas pressure or electric field fluctuations. A typical Mask Calibration spectrum is shown in figure 4.4.

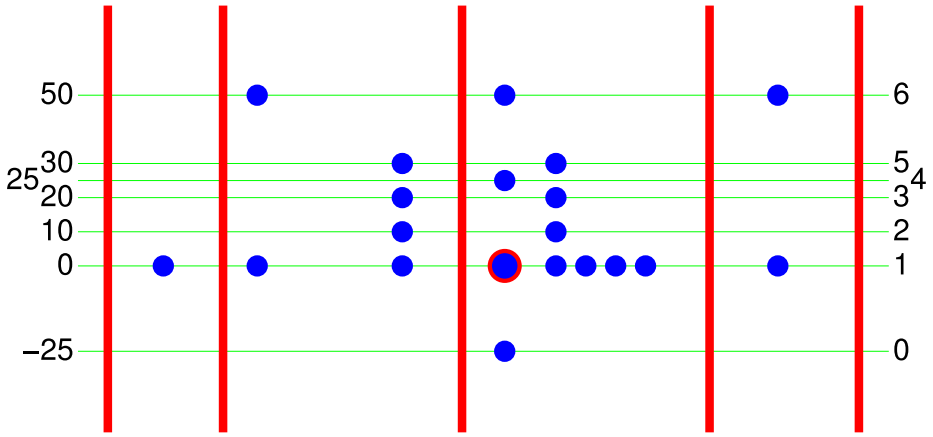

Figure 4.3: Schematic view of the mask used for the CRDC calibration. Adapted from [119].

The calibration factors for the y axis are extracted by a linear interpolation of the measured peaks with respect to the nominal holes positions. This allows to account for the variation of the parameters affecting the electrons velocity in the gas (i.e. gas pressure and temperature) and for the offset in the time measurement relative to the e1 scintillator. Since the readout of the x axis is performed using the cathode pads that are fixed in space, the gain of this axis (represented by the angular coefficient of the linear calibration) is fixed and is equal to the size of one pad (2.54 mm), for this axis only the offset has to be determined.
The calibration factors have been applied to the measured data using the closest Mask Calibration run available (in time).

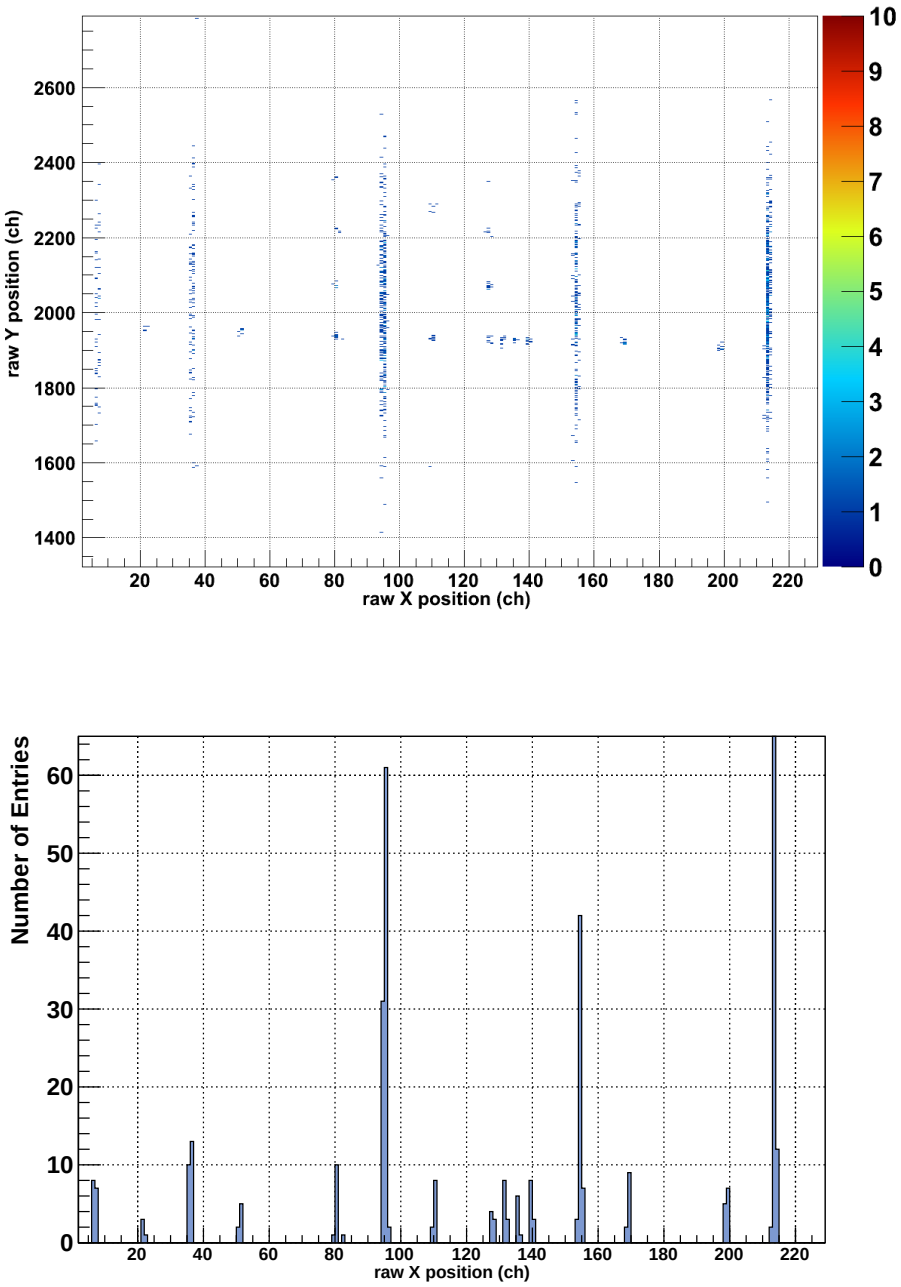

Figure 4.4: Top: measured data for the calibration of CRDC1. Bottom: x axis projection of the central holes line.

4.2 CAESAR calibration

The calibration of the 192 CsI(Na) CAESAR detectors was performed using standard calibration sources. Prior to the experiment, a gain matching of the signals coming from the detector was done optimizing for each channel the correspondent power supply voltage and the amplifier gain.

4.2.1 Energy and Time Calibration

For the energy calibration of the CAESAR detectors, runs with the sources ^{60}Co, ^{88}Y, ^{137}Cs and ^{22}Na were used. A dedicated tool was developed to automatically fit the calibration runs and manually check the results. Where the automatic procedure failed, the software allows to manually re-fit the peak. A second order polynomial was used to fit the calibration curves. Figure 4.5 shows a screen-shot of the software used while figure 4.6 displays the calibration curve for one detector. A global view of the calibration consistency for the whole CAESAR array is given in figure 4.7.
The time spectra used in the data analysis are given by the difference between the CAESAR time measured by the TFCs and a reference signal (i.e. the OBJ scintillator time). Although timing resolution is not a priority for the present experiment, the relative offset between the detectors has to be matched to obtain proper time-gate conditions. To do this, the offset of each channel was evaluated with respect to a channel chosen as a reference. The obtained values were used as the time calibration parameters.

4.2.2 Energy resolution

The energy-calibrated spectra have been also used to estimate the energy resolution of the CAESAR detectors. The measured Gaussian peaks widths (σ) as a function of the energy are shown in figure 4.8. The data refer to the CAESAR-summed spectrum with and without the use of the add-back routine. It can be seen that the add-back worsens the energy resolution by a factor close to 3% for 1 MeV γ-rays. The resolution of each detector has been used as an input parameter for the simulation that will be

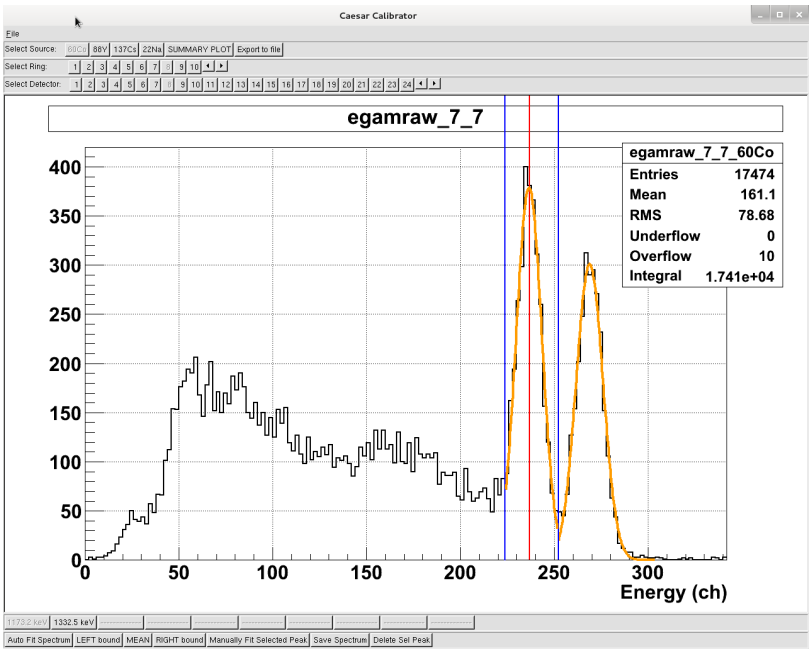

Figure 4.5: Screen-shot of the calibration software used to verify and correct the automatic fit results.

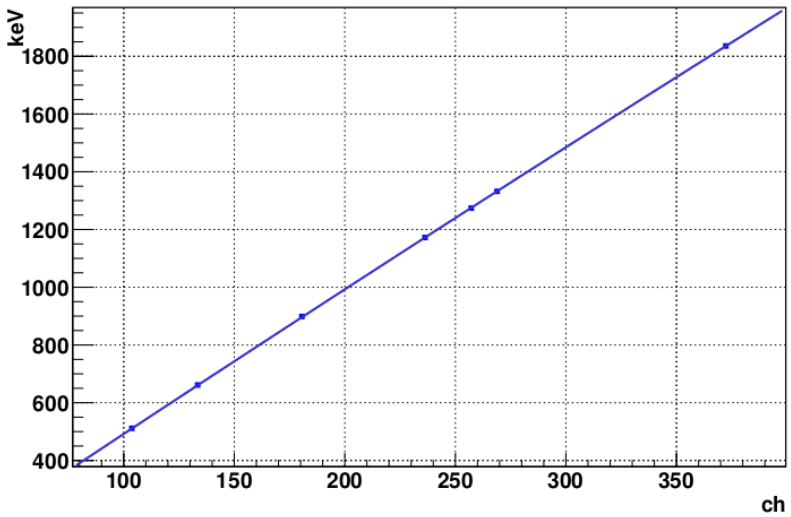

Figure 4.6: Calibration curve for a typical detector, the blue line is the fitted polynomial.

described in paragraph 4.3. According to the parametrization used by the simulation,

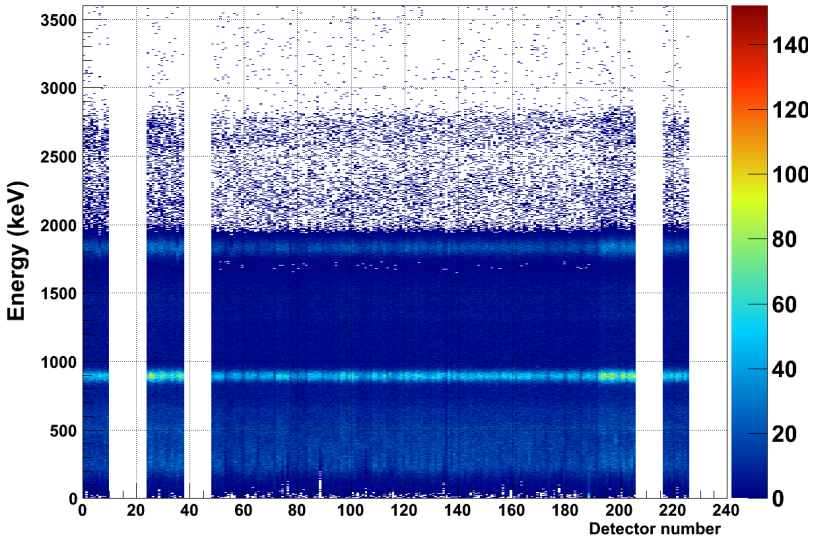

Figure 4.7: ^{88}Y source energy spectrum as a function of the detector number

the energy dependence of the peak width has been fit using the following formula:

$$\sigma(E) = \alpha \cdot E^{\beta} \tag{4.2}$$

Typical values of α and β are of the order of 0.60 and 0.55 respectively. In figure 4.9 the measured percentage resolution is shown as a function of the γ-ray energy. A good agreement is found with respect to the CAESAR published data [109] discussed in 3.6.3.

4.2.3 Energy thresholds

Another parameter that has to be taken into account is the energy threshold of the detectors. As already stated in the previous chapter, Coulomb excitation experiments with radioactive beams at intermediate energy are affected by a huge background due to atomic processes between the cocktail beam and the heavy thick target used. Since the excitation cross section depends on the square of the atomic number of the reaction partner ($\sigma^{ex}_{p,t} \propto Z^2_{t,p}$, cfr. eq. 2.34), the use of thick and high Z materials is useful to compensate for the low beam intensity and the low excitation cross sections

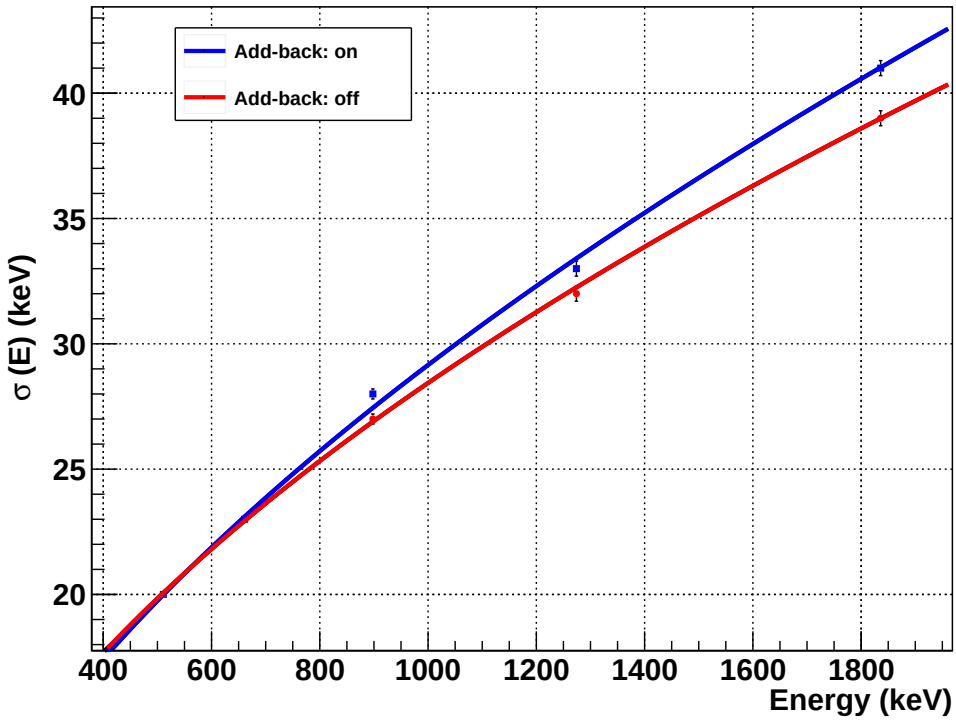

Figure 4.8: Measured resolution of the CAESAR array as a function of the γ-ray energy. Blue (red) dots are the measured data with (without) the use of the add-back routine. Corresponding lines are obtained using the function of eq. 4.2.

one has to deal with. The unavoidable drawback are the photons emitted by atomic processes that produce a continuum background up to several hundreds of keV. Since the energy of the transition of interest for the present measurement is of 1024 keV, to avoid an excessive count-rate due to the mentioned background, the trigger thresholds of the CAESAR detectors were set to a value of $\approx$ 300 keV. These thresholds affect the detection efficiency, especially when the add-back procedure is applied and have to be taken into account. To do this, ^{133}Ba source runs with lowered thresholds were compared to the experimental condition. Figure 4.10 shows this comparison for one of the CAESAR detectors. The measured thresholds were used as input for the simulation that we will describe in the following paragraph.

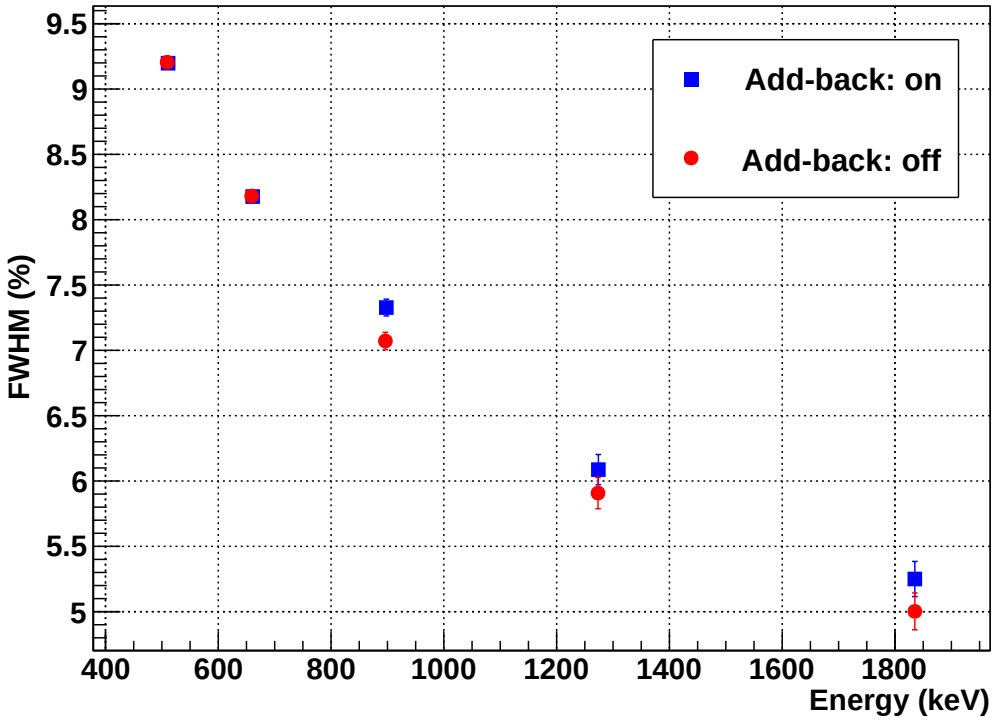

Figure 4.9: Intrinsic percentage energy resolution (FWHM %) as measured with standard calibration sources.

4.3 GEANT4 simulation

As anticipated in the previous paragraphs, a GEANT4 [120] simulation of the CAESAR array has been implemented at NSCL by T. Baugher [116] and will be used in the present analysis to fit the final γ-ray spectra. This code implements the geometry of the CAESAR array and has been used to simulate the energy release of the γ-rays in the active volume of the detectors. The use of a simulation allows for a proper detection efficiency estimation at the energy of interest. Moreover, it allows to disentangle the different contribution to the γ-ray spectrum coming from sources emitting at different velocities and to take into account the effect on the energy resolution due to the Doppler correction. Indeed, both stationary sources and in-beam conditions can be simulated. In the first case, a source of a given energy shoots γ-rays isotropically towards the detectors, while in the in-beam condition a projectile with given kinetic energy is shot towards the target. In this case, the interaction of

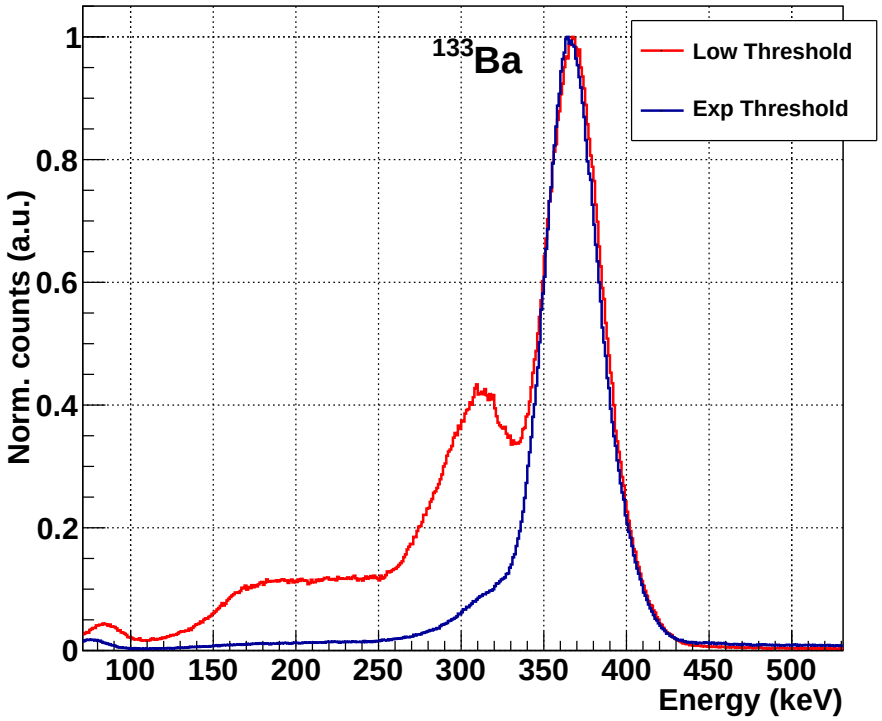

Figure 4.10: Energy threshold evaluation using the ^{133}Ba source. Blue line: experimental threshold condition. Red line: lower threshold condition. See text for details.

the particle with the target material is taken into account and the tracking of the incident particle is performed. If the target/projectile excitation option is turned on, a γ-ray of the selected energy is shot by the excited particle considering its momentum at the time of emission (causing the Doppler-shift of the photon).

In both cases (stationary source or in-beam condition), the simulation tracks the γ-ray path recording the energy release in the CAESAR detectors. For each simulated event the output file contains the list of detectors that were hit (ring and detector number) and the energy release information.

The simulated information are then filtered using a software-replica of the array considering actual energy thresholds and detector resolutions. These parameters must be given as an input and were obtained from the calibration runs described in the previous paragraph. Finally, the code performs the Doppler reconstruction (if needed) and implements the add-back procedure, providing the simulated and reconstructed γ-ray spectra for each of the CAESAR detectors. The final output

includes calibrated spectra with/without Doppler correction, with/without the use of the add-back routine as well as the integrated CAESAR spectra. As an example, the simulated ^{60}Co source spectrum is shown in figure 4.11 both for the add-back and non-add-back cases.
The proper use of the code is validated comparing the simulated CAESAR efficiency to the values measured with calibration sources. The results are discussed in the next paragraph.

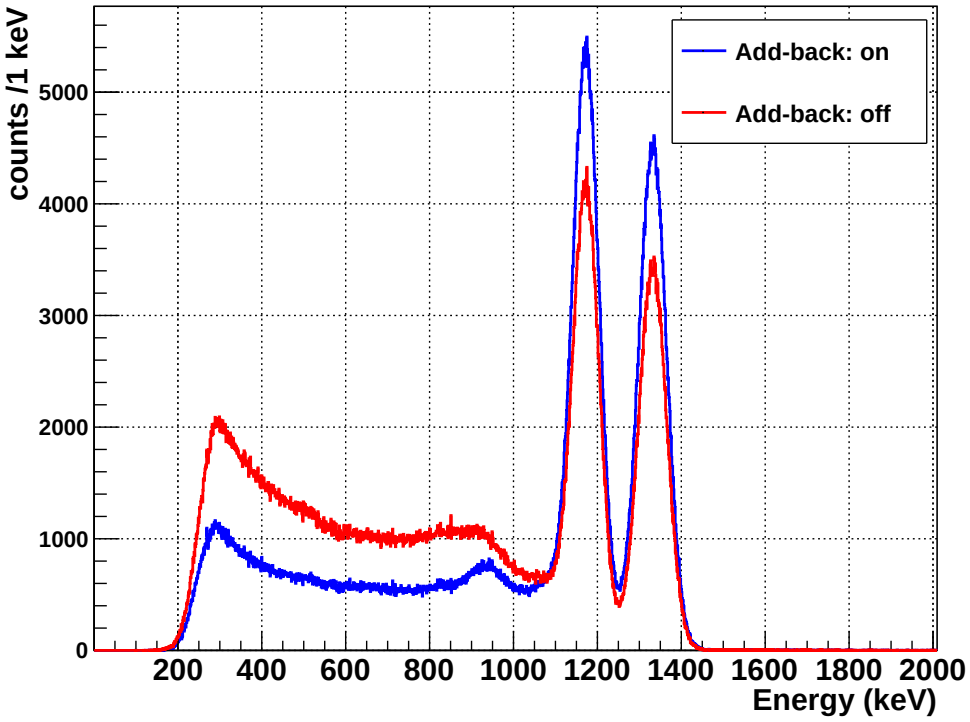

Figure 4.11: GEANT4-simulated ^{60}Co source spectrum. Blue (red) line corresponds to the add-back (non-add-back) simulated histograms.

4.4 Detection Efficiency

The detection efficiency of the CAESAR array has been measured with standard calibration sources. The background subtraction for the full-energy peak integration was done using the algorithms implemented in the TSpectrum class of the ROOT

package. Specific routines allow to model the Compton continuum and properly integrate the full-energy peak even in presence of more photon energies. Two examples are shown in figures 4.12 and 4.13 where the blue line represents the background subtracted spectrum that has been used for the integration. Acquisition live-time and the activity of the sources allowed to determine the CAESAR detection efficiency both when applying or not the add-back procedure. The same was done for the simulated spectra where the normalization factor is the number of generated events (that was fixed to 10^6 for all the simulations). The results obtained are shown in figure 4.14. As expected, the efficiency is increased using the add-back procedure with a larger effect ($\approx$ 15 %) for γ-rays energies higher than 800 keV. Moreover, the experimental data obtained in the present calibration are in good agreement with the published data reported in [109] and discussed in paragraph 3.6.3. Nevertheless it has to be underlined that the simulation shows a systematic overestimation ($\approx$ 10%) of the full-energy peak efficiency both in the case of singles and add-back spectra. This effect will be considered for the error estimation of the final experimental cross section.

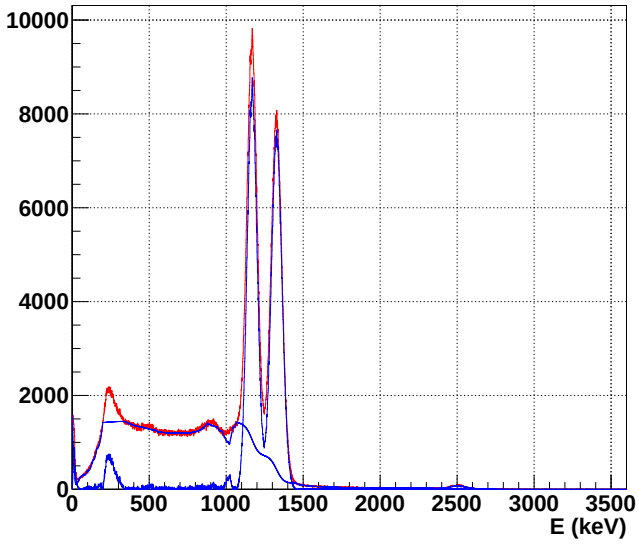

Figure 4.12: Measured ^{60}Co source spectrum obtained as a sum of all the CAESAR detectors (red histogram). Blue curve is obtained after Compton-continuum subtraction. See text for details.

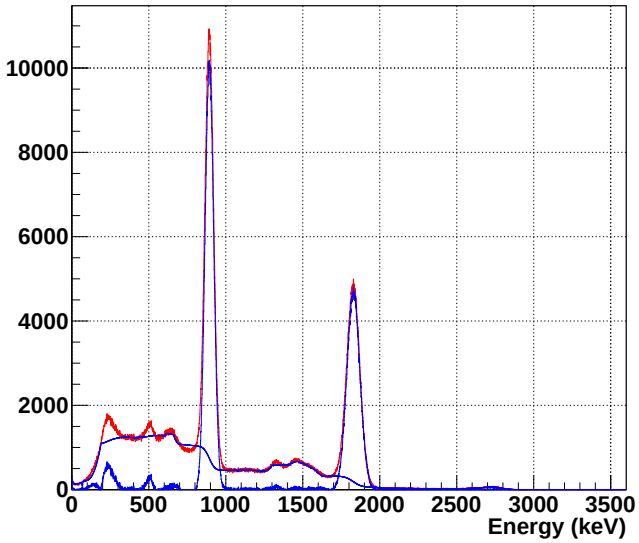

Figure 4.13: Measured ^{88}Y source spectrum obtained as a sum of all the CAESAR detectors (red histogram). Blue curve is obtained after Compton-continuum subtraction. See text for details.

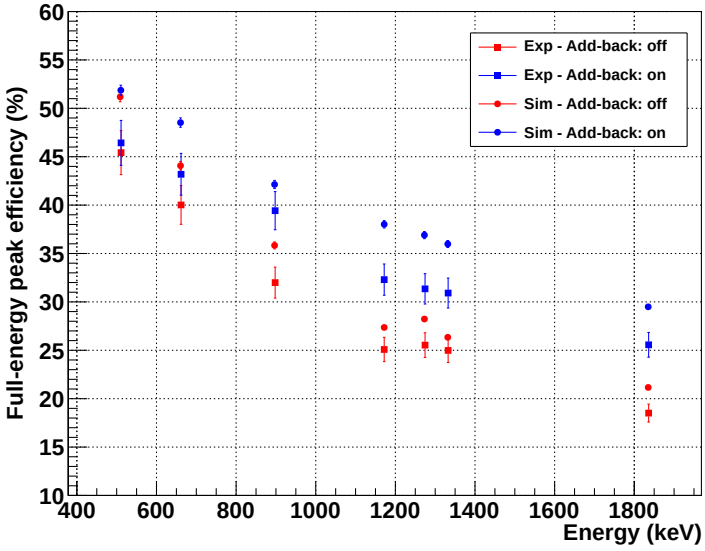

Figure 4.14: Measured (squares) and simulated (dots) absolute CAESAR efficiencies. Data in red (blue) are obtained without (with) the add-back routine.

4.5 Particle Identification

In order to measure the Coulomb excitation process it is necessary to select ^{74}Ni particles both from the cocktail beam approaching the secondary target and from the reaction products measured at the focal plane of the S800. This first step of data reduction is very important because, by definition, the Coulomb scattering does not involve the exchange of nuclear matter between projectile and target. Only events where a ^{74}Ni ion is identified in the "Incoming" Particle Identification matrix (Incoming PID) AND in the "Outgoing" one (Outgoing PID) have to be selected. To do this the energy loss in the ion chamber and the particles time of flight are used.
The *xfp_tac* measures the time of flight of the ions between the xfp scintillator and the e1 scintillator, the first being placed at the focal plane of the A1900 spectrometer and the second at the focal plane of the S800 (recall par. 3.4). This is the time it takes for a generic ion with a given $B\rho$ (where fixed $B\rho$ means a selected A/q ratio) to go from the A1900 fragment separator, along the switch-yard and the S800 analysis lines, through the target and the S800 dipoles to the S800 focal plane (see fig. 3.1). In the same way, the *obj_tac* variable measures the time of flight from the object scintillator to the e1.

4.5.1 Focal plane Particle Identification

For the Outgoing PID the $\Delta E - ToF$ technique is used. Ions emerging from the target are measured at the focal plane of the S800 and their identification is achieved plotting the energy loss in the ionization chamber (ΔE = sum over all the 16 segments of the calibrated ion chamber data) against the time of flight of the particles (using tac_xfp or tac_obj).
The energy deposited in the ion chamber (ΔE) is roughly proportional to the square of the nuclear charge (Z^2) according to the Bethe-Bloch formula [113]. As we will discuss in the next paragraph, the Time of Flight can be expressed as a function of the A/Z ratio (see eq. 4.7). As a result, isotopes of a particular element form tilted bands, while fragments with a constant neutron excess N-Z form vertical bands. This technique is widely used for the identification of new isotopes produced with very low intensity, see [121].

To improve the identification resolution it is necessary to correct the time of flight and energy loss values accounting for the trajectory of the particle in the S800 spectrometer.

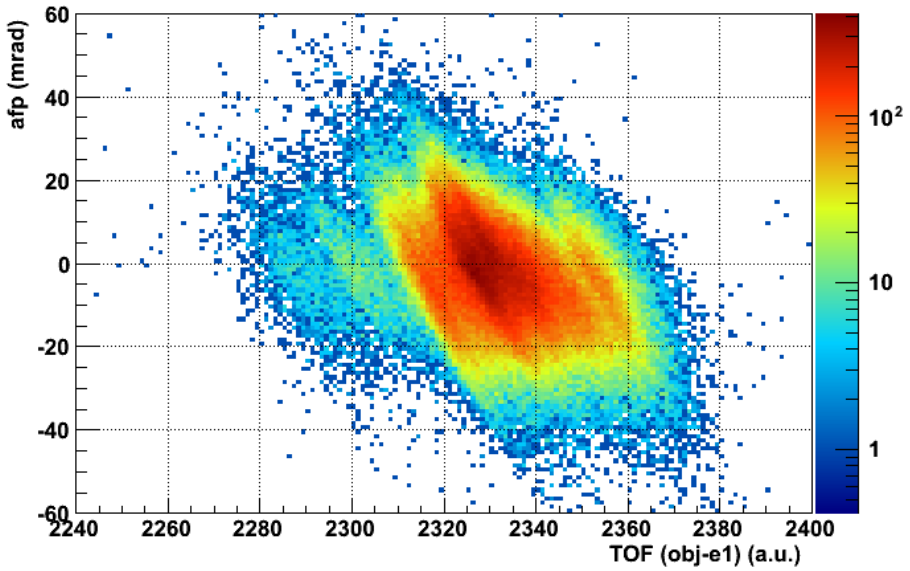

Figure 4.15: Example of measured non corrected focal plane angle - time of flight correlation.

Time of flight - trajectory correction The time of flight through the S800 spectrometer depends on the trajectory of the particle. This causes a smearing in the particle identification plot that has to be corrected. Since the trajectory is directly related to the measured focal plane angle, the Dispersive Focal Plane Angle - Time of flight matrix is used, see figure 4.15. Using a parametrization like:

$$TOF_{corr} = TOF_{meas} + \alpha \; a_{fp} \tag{4.3}$$

it is possible to compensate for the different path of the particles into the spectrometer. The best α value is determined by an iterative procedure and a_{fp} is the angle measured at the focal plane in the dispersive direction of the magnetic field (that is the most affected one). The final result is shown in figure 4.16 where the effect of the flight path correction is evident when compared to figure 4.15.

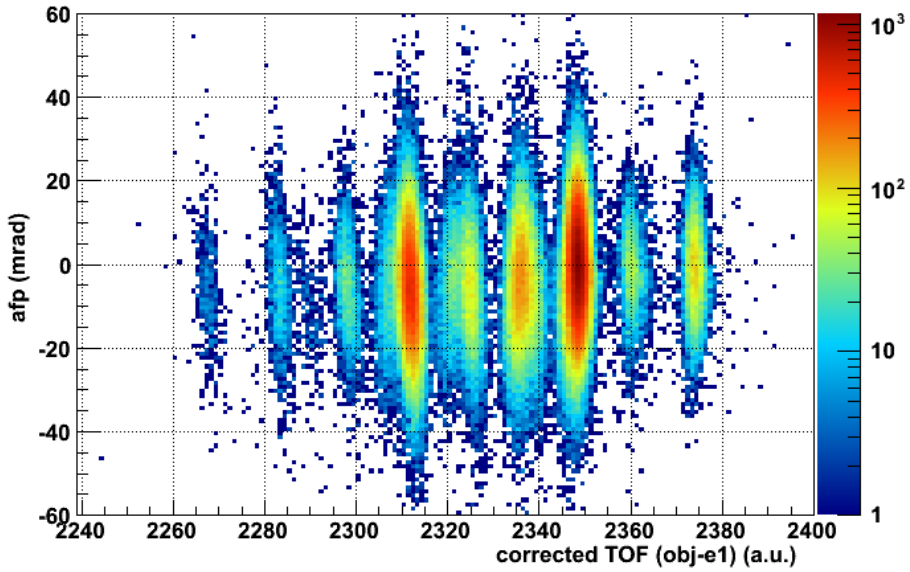

Figure 4.16: Example of measured corrected focal plane angle - time of flight correlation. The effect of the flight path correction term are evident.

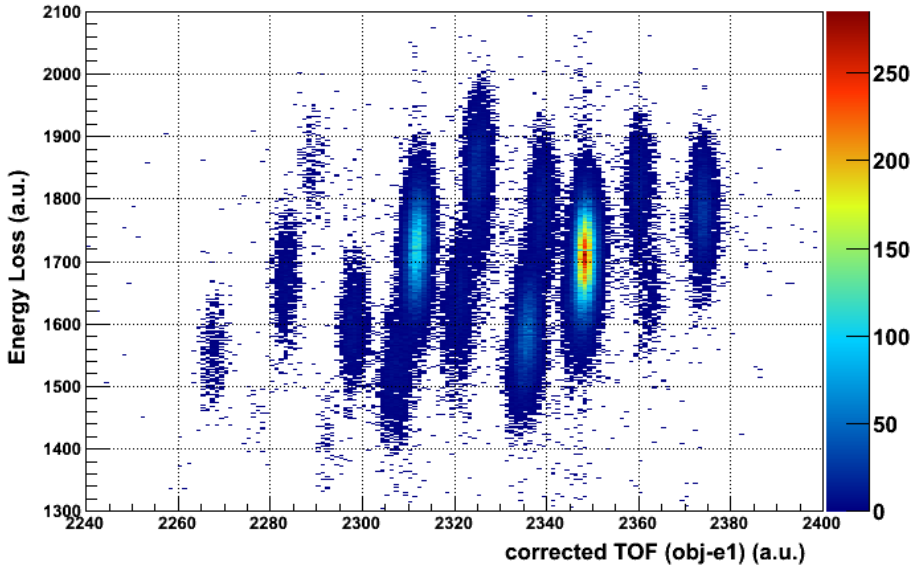

Figure 4.17: Example of measured non-corrected Energy loss vs corrected time of flight correlation.

Ionization chamber - trajectory correction The trajectory of the ions at the focal plane influences the path length into the ionization chamber and this has effects on the total energy loss. Figure 4.17 shows the outgoing particle identification spectra where the flight path correction is applied but without the Ionization Chamber trajectory correction.
To take this last effect into account, an exponential correction factor has to be applied:

$$E_{corr} = E_{meas}\ e^{p(x-x_0)} \tag{4.4}$$

The determination of the two parameters p and x_0 is done fitting the x profile of the Ion Chamber ΔE - Focal Plane x position correlation gated on one incoming/outgoing ion. The use of the correction parameters, allows to obtain a clean particle identification at the focal plane. The final Energy Loss - Time Of Flight matrix is shown in figure 4.18. Elemental species and isotope mass are assigned to the different regions relatively to the most intense beam (^{77}Zn) on the basis of the LISE++ simulation. In the following analysis, the data selection for the outgoing beam identification is performed using the shown corrected matrix.

4.5.2 Beam particles tagging

The incoming particles tagging is performed using the information about the time of flight of the ions along the transport beam-line.
The time difference between *xfp_tac* and *obj_tac* is simply the time it takes for the ion to go from the xfp to the obj points through the transport line (see fig. 3.1). This means that:

$$\text{xfp\_tac} = \text{obj\_tac} + \Delta\text{TOF} \tag{4.5}$$

if the transport line is long D and has a magnetic rigidity $B\rho$ and the particle has mass A, charge state q and velocity v, ΔTOF can be expressed as:

$$\Delta\text{TOF} = \frac{D}{v} = \frac{\gamma D}{B\rho}\ \frac{A}{q} \tag{4.6}$$

given a setup, D and $B\rho$ are constant. Making the hypothesis that the ions are

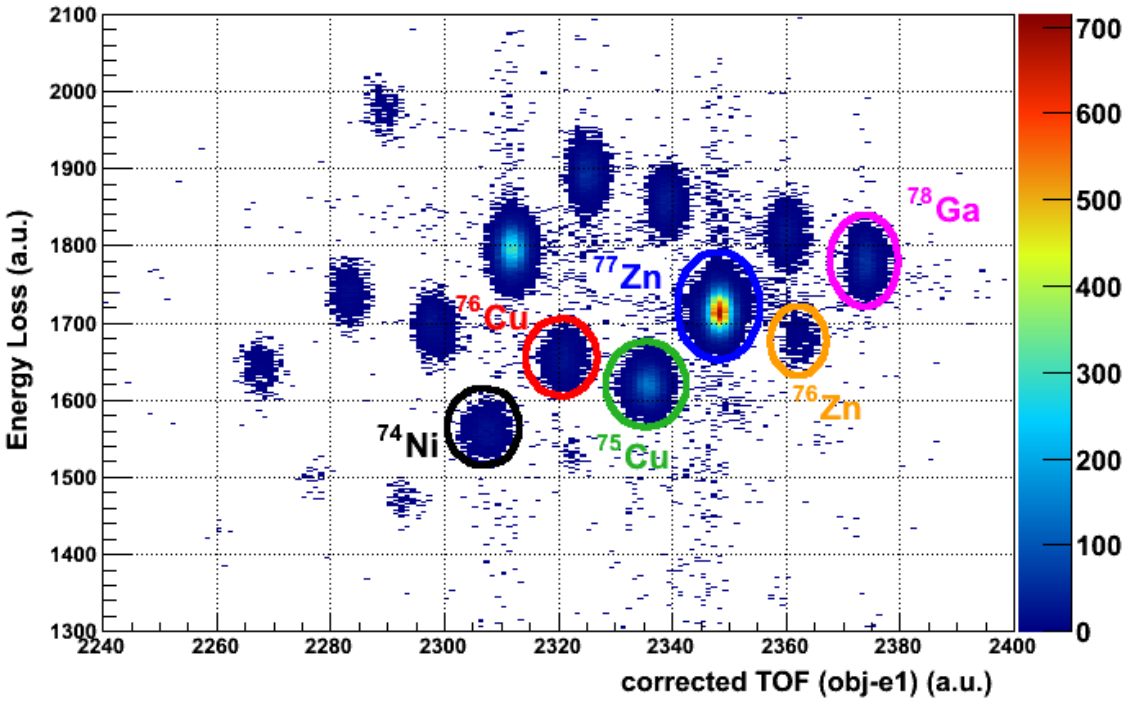

Figure 4.18: Final focal plane particle identification matrix. The full correction (flight path and ion chamber) has been applied. See text for details.

fully stripped ($q = Z$),

$$\text{xfp\_tac} = \text{obj\_tac} + K\,\frac{A}{q} \tag{4.7}$$

Therefore the plot of xfp_tac vs obj_tac is a straight line with angular coefficient 1 and intercept proportional to the particle A/q ratio. Since the time of flight is also related to the particle velocity and the momentum is selected by the $B\rho$ value, ions with similar A/q ratio but different mass will have different velocity and will arrange into islands along the same line. This can be clearly seen in runs without the secondary target where the A1900 momentum acceptance was set to 0.5%, as shown in figure 4.19. In this case, using the particle identification on the focal plane, it is possible to uniquely tag incoming ions and demonstrate the validity of the selection method. However, as already stated, the low ^{74}Ni production rate required to run at dp/p = 3% and this compromise strongly affects the incoming particle tagging performances. Figure 4.20 shows that, although it is still possible to isolate an area

uniquely assignable to incoming ^{74}Ni, the different ions overlap. Figure 4.21 shows, indeed, the actual experimental situation (with target an large momentum acceptance). It is clear that a clean identification is not possible and this represents the main limitation of the present experiment.

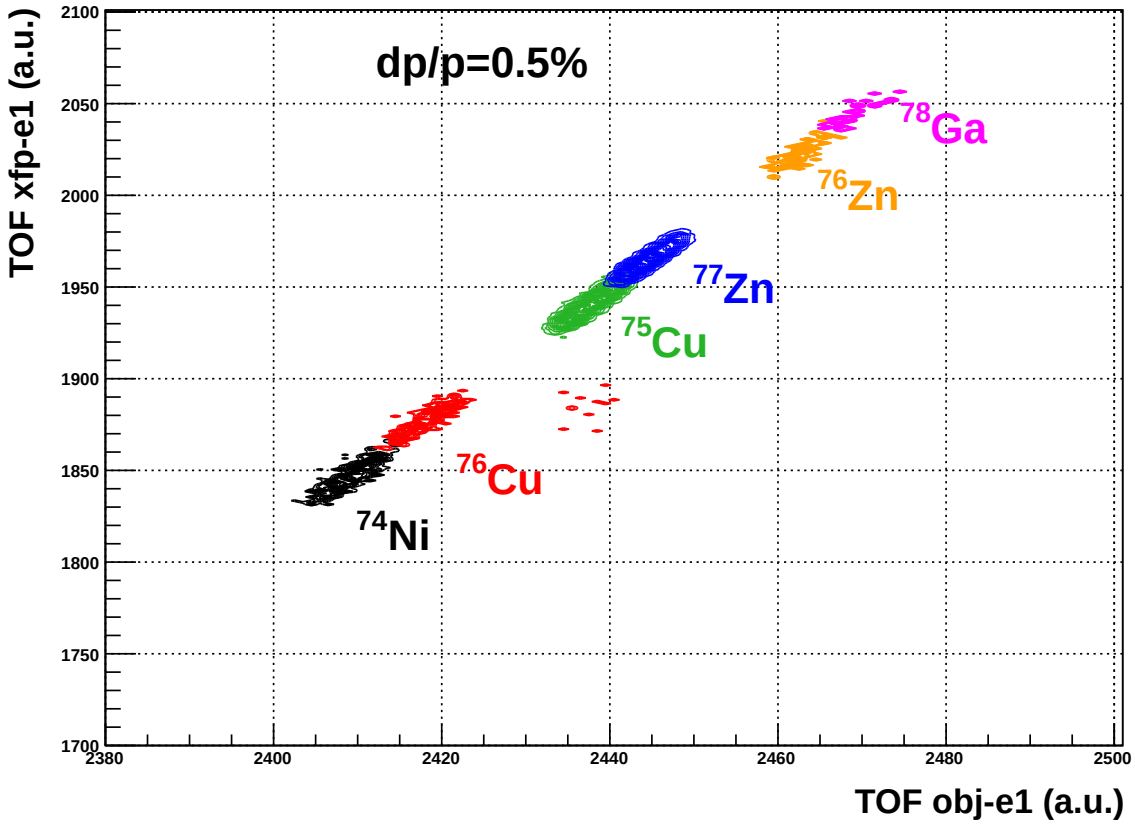

Figure 4.19: Incoming particle PID plot. Momentum acceptance is dp/p=0.5%, no target is present. The different species are tagged using the focal plane identification.

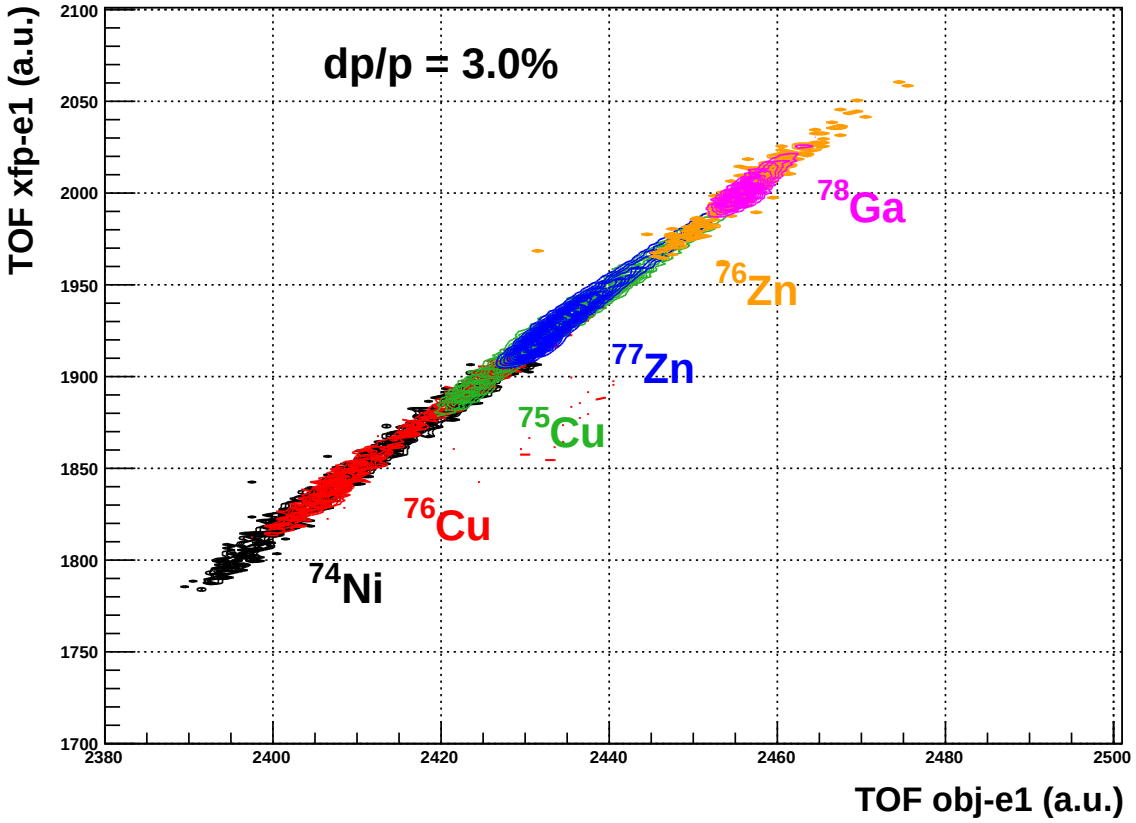

Figure 4.20: Incoming particle PID plot. Momentum acceptance is dp/p=3.0%, no target is present. The different species are tagged using the focal plane identification. Overlapping regions demonstrate the worsening of the PID resolving power.

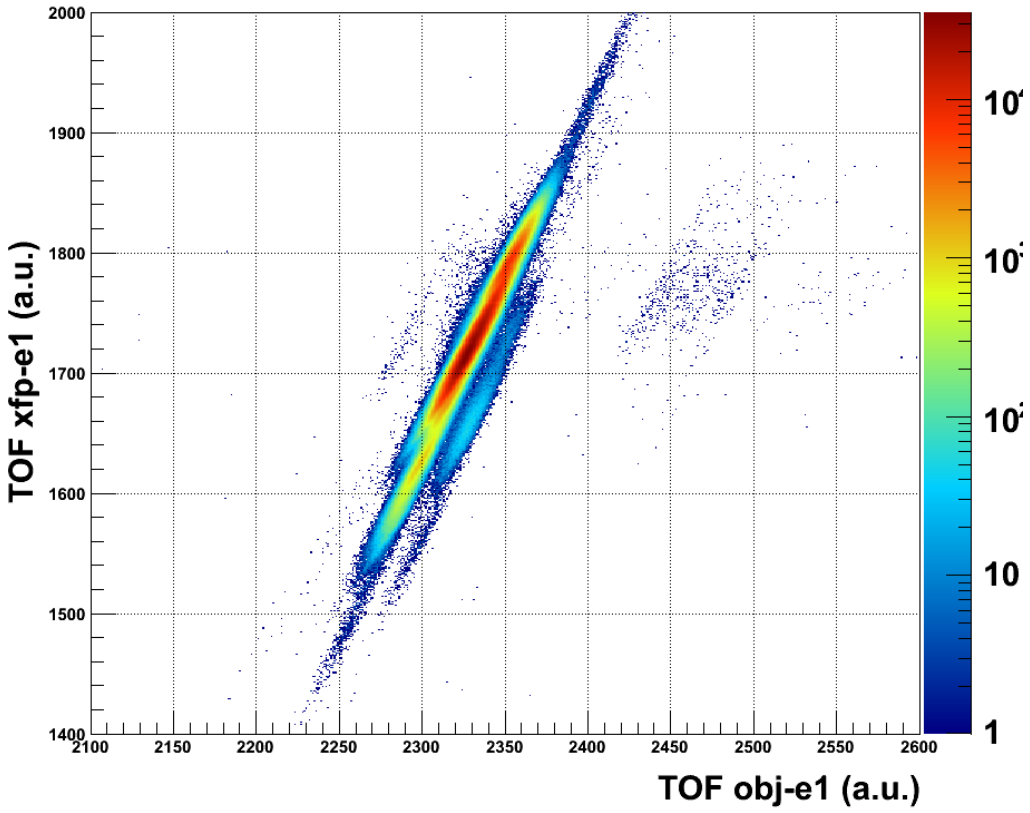

Figure 4.21: Incoming beam particle identification in the actual experimental condition.

4.6 Events selection

The particle identification spectra are used to reduce the data set to the events where a ^{74}Ni ion is tagged both in the incoming and outgoing beams. This is needed to select only the events where Rutherford scattering or Coulomb excitation occurred. Transfer reactions of one or more nucleons from the cocktail beam, populating ^{74}Ni in an excited state represent the main source of background for this type of experiment. Since the outgoing beam PID is the most clean, we start applying a gate condition the ^{74}Ni region on that correlation. This ensures the selections of particles emerging from the target as ^{74}Ni and reducing the incoming particle matrix (compare figures 4.21 and 4.22).

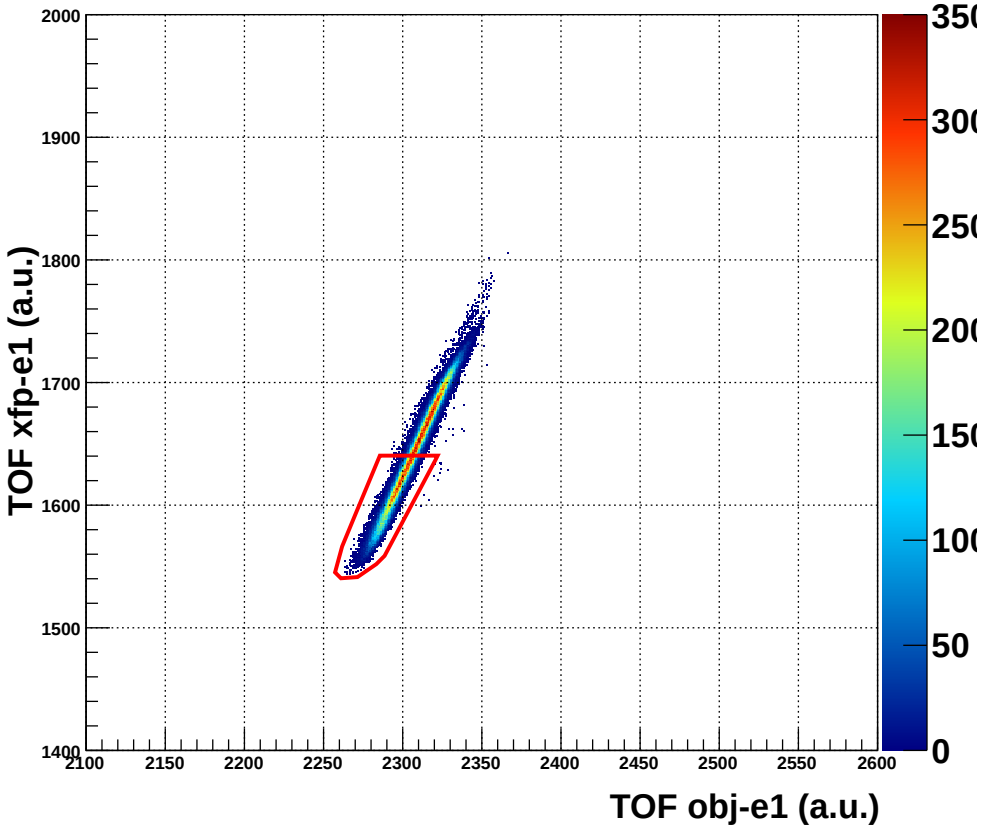

Figure 4.22: Incoming beam particle identification gated on the ^{74}Ni outgoing ions. The red line represents the cut applied in the following data analysis.

At this point a further cut has to be applied to select only the incoming ^{74}Ni ions. Taking into account the information gained from the no-target runs (figures 4.19 and 4.20), the region defined by the red curve of figure 4.22 was considered as the cleanest choice. This has been cross-checked applying different size cuts on matrix and looking at the correlated γ-ray spectra.
Once the events data set has been defined, two parameters have to be extracted: the particle velocities (β) needed for the Doppler Shift correction of the γ-ray energies and the particle scattering angles (θ) necessary for the safe impact parameter selection. The measured mean velocity of the particles has been reconstructed using both no-target runs (beam velocity) and measurement runs (velocity after target). Table 4.1 compares the experimental values with the results obtained from the LISE++ simulation.

	calculated β (%)	measured β (%)	E (AMeV) - LISE
Incoming	42.2	41.7 $\pm$ 0.4	95.8
Half target	39.5	-	81.1
After target	35.8	35.8 $\pm$ 0.2	66.0

Table 4.1: Kinematics parameter of the ^{74}Ni beam as calculated by LISE++ or measured by the S800.

As explained in paragraph 3.5.2, the particle scattering angles are obtained from the angles (a_{ta}, b_{ta}) at the target position reconstructed using the spectrometer inverse map. After centering the a_{ta} vs b_{ta} correlation, as shown in figure 4.23, the scattering angle is reconstructed using the equation 3.5. The resulting distribution is shown in figure 4.24 where the cut applied for the safe impact parameter condition is evidenced by the red line.

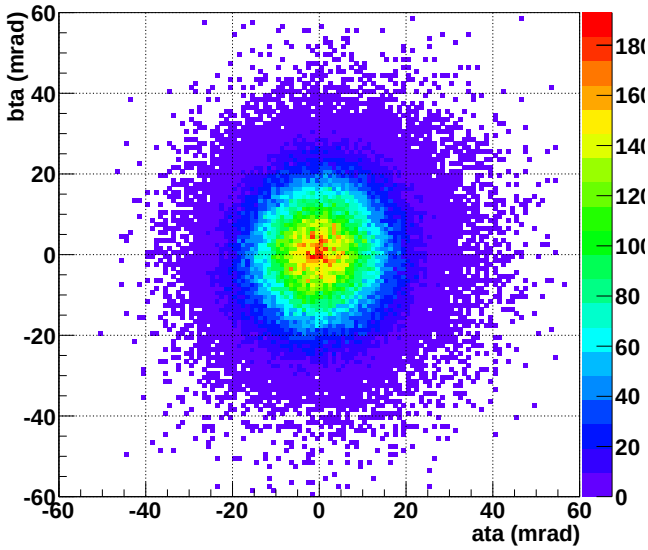

Figure 4.23: Correlation between the reconstructed dispersive and non-dispersive angles at the target position. The distribution has been shifted in order to be centered around the origin of the axis.

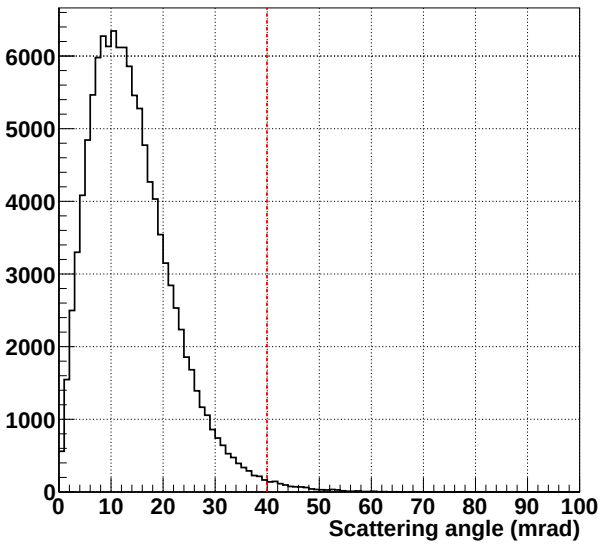

Figure 4.24: ^{74}Ni scattering angle distribution. The red line indicates the position of the cut used for the impact parameter selection.

4.6.1 Gamma ray spectra

Given all the previously described selections, the coincidence γ-ray spectrum can analyzed. A further time gate has to be applied in order to remove the uncorrelated γ-rays background. As shown in figure 4.25, in order to obtain a cleaner selection, the cut is performed on the time-energy correlated spectrum. The final energy spectrum is shown in figure 4.26: after the proper Doppler shift correction the expected 1024 keV peak relative to the ($2^+ \rightarrow 0^+$) transition, is clearly visible. The Doppler correction was performed on an event by event basis using the measured velocity of the emitting particle and its relative scattering angle with respect to the emitted γ-ray. As anticipated in paragraph 3.6.2, due to the large amount of Bremsstrahlung

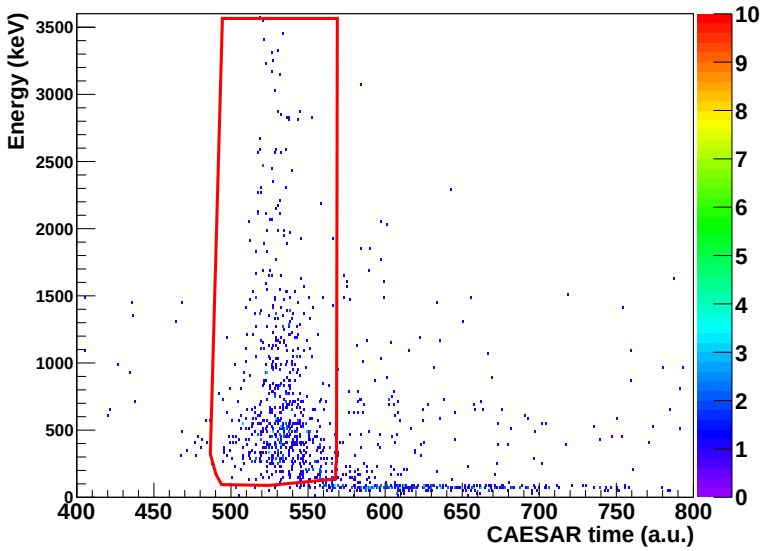

Figure 4.25: CAESAR Energy-time correlation used for the time cut.

background, the add-back procedure is strongly affected. As one can see comparing figures 4.26 and 4.27, the final result is a reduction of the global statistics that is not translated in a better peak to background ratio. This effect can be explained by a wrong reconstruction of the Compton scattering events to which a huge uncorrelated background sums up. This is confirmed also by the large number of high multiplicity events observed (see figure 4.28) which are not compatible with the selected reaction mechanism. Since the add-back procedure was expected to give a gain in the total

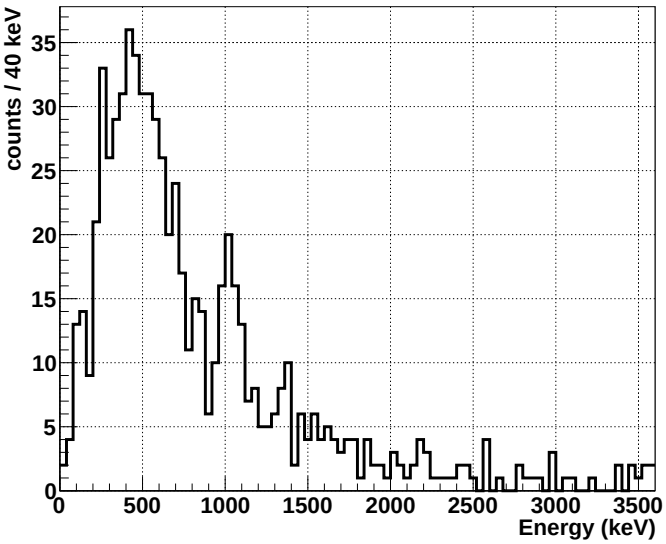

Figure 4.26: ^{7}4Ni γ-ray spectrum. Event by event Doppler correction and scattering angle cut are applied.

detection efficiency and it was observed the opposite behavior, it was neglected for the further analysis. The integral of the 1024 keV full-energy peak was evaluated

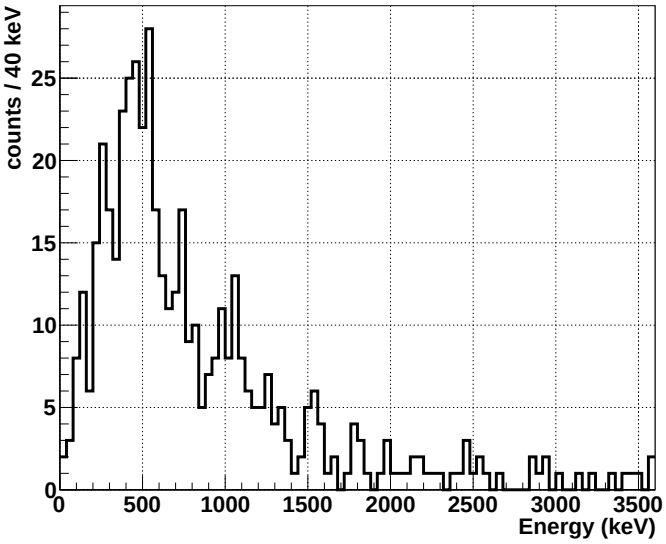

Figure 4.27: ^{7}4Ni γ-ray spectrum after the add-back procedure. Event by event Doppler correction and scattering angle cut are applied.

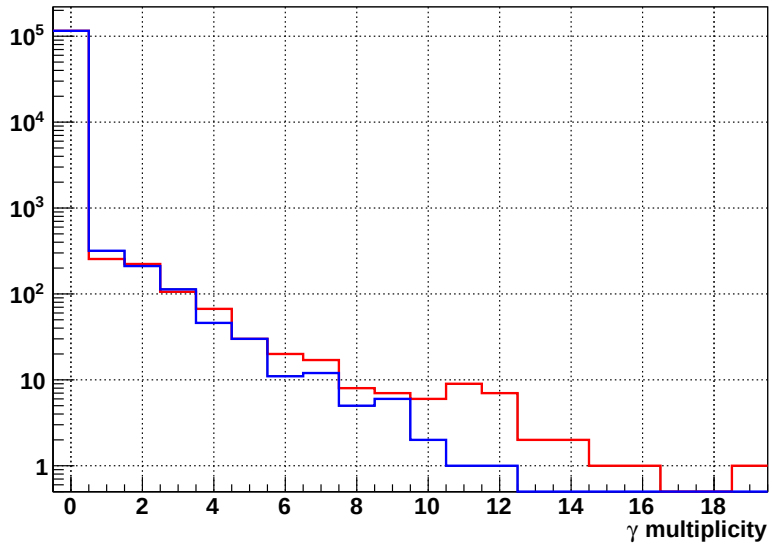

Figure 4.28: In-beam γ-rays multiplicity. The red (blue) histograms correspond to the data before (after) the use of the add-back procedure.

fitting the experimental data with the results of the GEANT4 simulation. A double exponential function was used to account for the background subtraction. The resulting fitting function used is:

$$f(f) = p_0 \cdot e^{-p_1 x} + p_2 \cdot e^{-p_3 x} + p_4 \cdot S_{Ni}(x) \tag{4.8}$$

The number of γ-rays emitted is extracted from the fit function by multiplying the number of GEANT4 simulated events by the fit function parameter corresponding to the full energy peak and accounts automatically for the efficiency of the setup. The following relation is used:

$$N_{\gamma}^{fit} = p_4 \cdot N_{sim} \tag{4.9}$$

Here $N_{sim} = 10^6$ is the number of simulated events. Figure 4.29 shows the final fit result, while in table 4.2 the numeric values are reported. The uncertainty of the final number of γ-rays, reported in the same table, is calculated through the error propagation of three components: δp_{Ni} is the relative uncertainty on the fit parameter p_4, δ_{sim} is estimated from the uncertainty on the efficiency of the GEANT4 simulation (see par. 4.4) and δ_{source} is the accuracy on the calibration source activity.

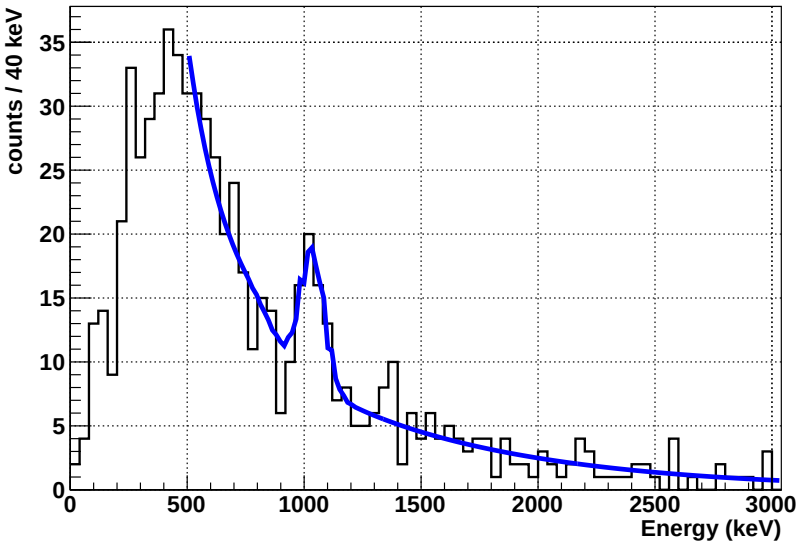

Figure 4.29: Final ^{74}Ni γ-ray spectrum. The blue line represents the result of the GEANT4 simulation fit.

p_4^{Ni}	δp_4^{Ni}	δ_{sim}	δ_{source}	N_γ^{fit}	δN_γ^{fit}
$104 \cdot 10^{-4}$	0.23	0.10	0.03	104	0.25

Table 4.2: Fit results and relative errors for the integral of the 1024 keV full-energy peak for the ^{74}Ni first excited state.

4.7 Excitation Cross Section

In order to calculate the excitation cross section, according to equation (4.1), it is necessary to correct the measured N_γ^{meas} and N_B^{meas} considering the live-time of the acquisition system and this is strongly related to the triggers used in the experiment. As explained in the previous chapter, the particles trigger request is given by the e1 scintillator at the focal plane of the S800. For the γ-rays part (CAESAR), the main trigger is the global OR of the 192 Constant Fraction Discriminators. As a consequence, three different triggers can be considered:

1. Particle trigger: **S800 Singles**;
2. Particle/γ coincidence: **Coincidence** = (S800 Singles) AND (CAESAR OR).
3. γ-ray single trigger: **CAESAR OR**;

Due to the high count rate at the focal plane of the S800, the first trigger has been downscaled by a factor **3**. Trigger requests are recorded on an event by event basis in the data stream and can be recovered in a "bit pattern" format. Figure 4.30 shows the integral values for the all measurement runs used in the analysis. The numerical values of the integrals are reported in table 4.3.

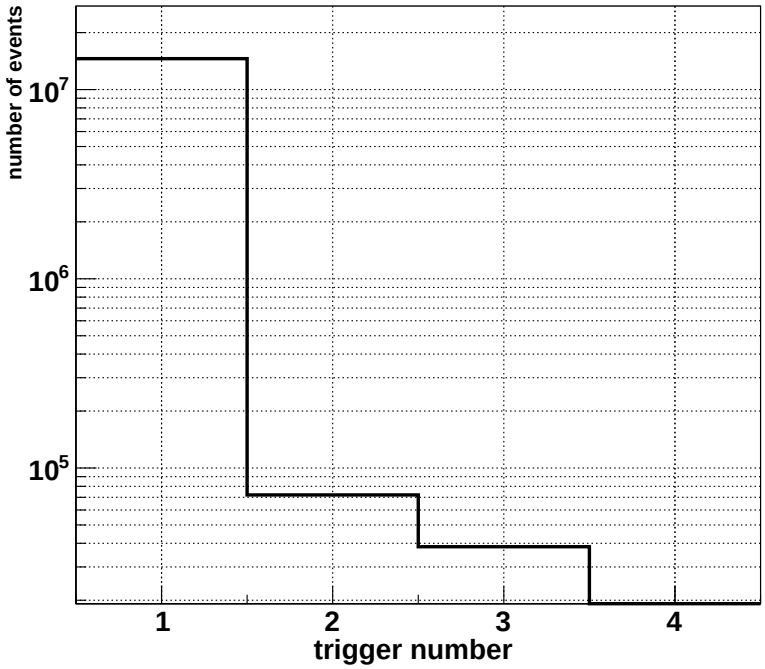

Figure 4.30: Bit pattern summed over the whole measurement data set. Bit 1 are the S800 singles, bit 2 are the

Trigger	Downscaling	Bit pattern integral (BI)
Particle trigger	3	14,563,797
Coincidence trigger	-	72,054
γ-ray singles	-	38,365

Table 4.3: Trigger bit integrals summed over all the statistics.

The bit pattern is affected by the same dead time as the data acquired. Scalers are used to measure the real number of trigger requests sent by the three different

channels. This device has to be considered as dead-timeless counter: the content of the scaler channels are read out and reset every 2 seconds and the data are recorded in the event file. The channels used for the dead time estimation are:

1. Raw.Clock: samples a 10 kHz frequency oscillator. Should give a good estimation of the real acquisition time;
2. Live.Clock: as Raw.Clock but vetoed by the global acquisition veto;
3. S800.Source: counts the raw number of S800 triggers (not downscaled);
4. S800.Trigger: as S800.Trigger but after the downscaling;
5. Coinc.Trigger: counts the number of coincidences between S800.Trigger and the CAESAR OR;

Trigger	Scaler Integral
Raw.Clock	3,473,904,072
Live.Clock	3,341,247,767
S800.Source	43,567,541
S800.Trigger	14,521,791
Coinc.Trigger	114,434

Table 4.4: Scalers integral values for the complete statistics.

The numerical values of the scalers integrals are reported in table 4.4.
If we indicate as BI_x the bit-pattern Integral for channel x and as SI_x the Scaler Integral for the same channel, the live-time correction for the γ-rays integral can be computed as follows:

$$LT_{coinc} = \frac{BI_{\gamma-raysingles} + BI_{Coincidence}}{SI_{Coinc.Trigger}} \tag{4.10}$$

since no downscaling has been applied to this trigger, the value has to be consistent with the global live-time computed as:

$$LT_{acq} = \frac{SI_{Live.Clock}}{SI_{Raw.Clock}} \tag{4.11}$$

The Live-time for particles counting in the S800 can be calculated only taking into account the downscaling factor, namely:

$$LT_{S800} = \frac{BI_{S800singles}}{SI_{S800.Source}} \tag{4.12}$$

A cross check of the downscaling factor value (DS_{S800}) can be obtained from:

$$DS_{S800} = \frac{SI_{S800.Source}}{SI_{S800.Trigger}} \tag{4.13}$$

At this point one can correct the measured values and obtain the final number of fragments:

$$N_B = \frac{N_B^{meas} DS_{S800}}{\epsilon_{S800} LT_{S800}} \tag{4.14}$$

Where the efficiency of the particle detectors (ϵ_{S800}) is one. The corrected number of γ-rays is:

$$N_\gamma = \frac{N_\gamma^{meas}}{\epsilon_{coinc} LT_{coinc}} \tag{4.15}$$

Given the Avogadro's number $N_A = 6.022 \times 10^{23}$ mol^{-1}, the areal density of the target ($\rho = 642$ mg/cm^2) and the atomic mass of the target nuclei ($A = 196.9665$g/mol), N_T is given by:

$$N_T = \frac{N_A\ \rho}{A} \tag{4.16}$$

N_B	$(34.8 \pm 0.1) \cdot 10^4$
$N^\gamma_{0^+ \to 2^+}$	108 ± 27
N_T	$(1.94 \pm 0.01) \cdot 10^{21}$

Table 4.5: Summary of the values used for the cross section calculation.

Measured values are reported in table 4.5, the result for the experimental cross section is $\sigma_{0^+ \to 2^+} = (159 \pm 40)$ mbarn.

5

Results and conclusion

Using the experimental cross section obtained in the previous chapter and normalizing to the DWEIKO calculation illustrated in paragraph 2.5, it is possible to extract the reduced transition matrix element for the first 2^+ state of the ^{74}Ni nucleus. Given the linear relationship between the excitation cross section and the B(E2) value expressed by eq.2.32, the results of the DWEIKO calculation are linearly scaled to extract the experimental B(E2). The result is:

$$B(E2; 0^+ \rightarrow 2^+) = (694 \pm 173)\ e^2 fm^4$$

The value obtained is affected by an uncertainty of 25%. This is mainly due to three experimental reasons. First of all there is a limit in the γ-ray peak statistics. This has to be ascribed to the low intensity of the produced ^{74}Ni radioactive beam and to the limited amount of time available for the experiment. To partially overcome this problem, the A1900 has to be operated at 3.0% momentum acceptance but this affected the beam particles tagging, severely restricting the clean particle identification

region of the incoming particle. The second problem is connected to the impossibility of using an experimental normalization point for the measured cross sections. Due to the large low energy background and the poor resolution of the high-efficiency CAESAR scintillators, it was not possible to extract the target excitation experimental cross section and to use it for the normalization of the ^{74}Ni data. Neither the cocktail beam composition helped in this direction since no evaluated excitation cross sections are available for any of the isotopes impinging on the target. The third source of uncertainty is connected to the CAESAR efficiency estimation error and to the high multiplicity events that make the add-back procedure not reliable.
Despite the quite large error bar, the present result is not compatible with the one obtained by Aoi and collaborators in [67]. However, it has to be underlined that the two values have been derived using two different techniques. By definition, the Coulomb excitation mechanism is only sensitive to the electromagnetic interaction between the reaction partners (nuclear interactions contributions have been explicitly removed by a cut on the impact parameter), while Aoi and co-workers performed a proton scattering experiment where the nuclear interaction is the only excitation process. If this difference is confirmed, it could be the indication of an important de-coupling of the neutron and proton shells in presence of a strong neutron excess.
Figure 5.1 shows the present result compared to the Evaluated data reported in [52] and the shell model calculation based on the GXPF1A and the JUN45 interactions. Some very recent results by L. Coraggio and collaborators [122] and by N. Shimizu and co-workers [123] are also shown. The latter is a large scale Monte Carlo shell model calculation. The results obtained in this recent work are capable to span a wide mass range. The B(E2) value obtained in the present thesis work is compatible with the theoretical expectations of the MonteCarlo shell model, while is slightly higher than the other calculated values. It is indubitable that new measurements in the same mass region are still needed to confirm and complete the present study. Moreover it is worth to notice that the N. Shimizu and co-workers model predicts an increase of the B(E2) value for the ^{78}Ni nucleus, opposite to what one could expect given the nominal double shell closure at Z=28 and N=50. This feature is very interesting and it underlines the importance of better determine the ingredients needed to describe the structure in this exotic mass region. This underlines once more the importance of the new generation facilities since they will allow the production of more intense

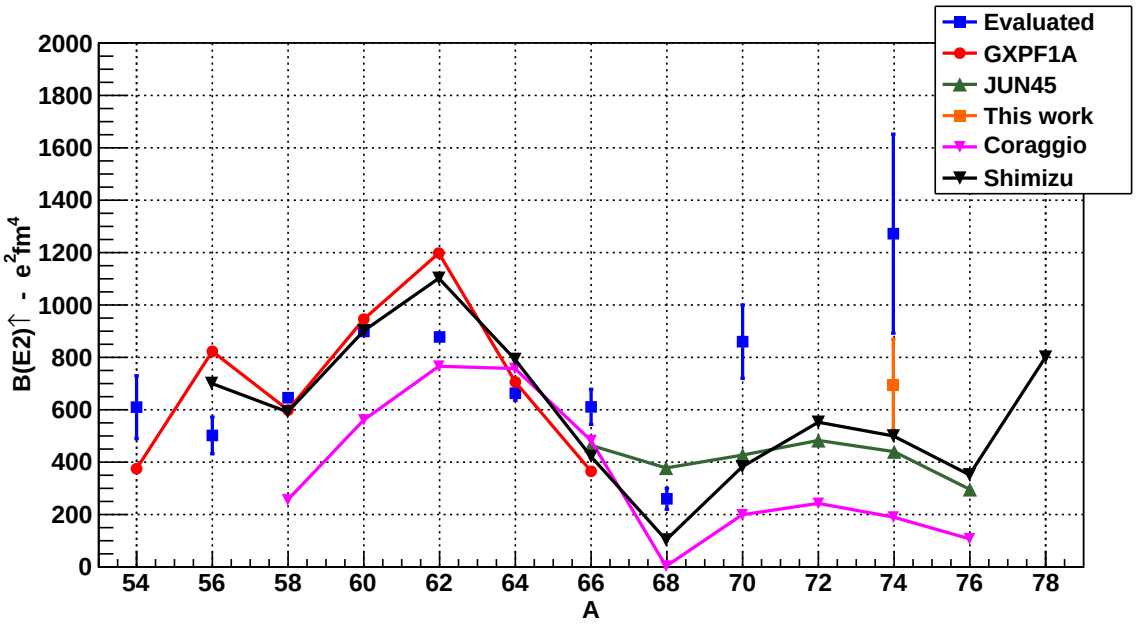

Figure 5.1: Experimental values and theoretical expectations for the $B(E2) \uparrow$ matrix element of the known even-even Ni isotopes. Data are from [52, 123] and completed with the result of the present analysis.

and exotic radioactive ion beams so that the experimental access of this region will be possible, bringing very important information on the actual shell evolution.

Bibliography

[1] G. F. Bertsch, D. J. Dean, and W. Nazarewicz, Scidac review: Subatomic discovery through advanced computing, http://www.scidacreview.org/0704/html/unedf.html.

[2] D. Bazin, Nature **486**, 330 (2012).

[3] J. Al-Khalili, An introduction to halo nuclei, in *The Euroschool Lectures on Physics with Exotic Beams, Vol. I*, edited by J. Al-Khalili and E. Roeckl, volume 651 of *Lecture Notes in Physics*, pp. 77–112, Springer Berlin Heidelberg, 2004.

[4] G. Audi, A. Wapstra, and C. Thibault, Nuclear Physics A **729**, 337 (2003).

[5] T. Otsuka, T. Matsuo, and D. Abe, Phys. Rev. Lett. **97**, 162501 (2006).

[6] D. Shetty and S. Yennello, arXiv:1002.0313v4 [nucl-ex] (2010).

[7] M. Baldo, *Nuclear Methods and the Nuclear Equation of State* (World Scientific, 1999).

[8] National nuclear data center, http://www.nndc.bnl.gov/.

[9] M. G. Mayer, Phys. Rev. **75**, 1969 (1949).

[10] O. Haxel, J. H. D. Jensen, and H. E. Suess, Phys. Rev. **75**, 1766 (1949).

[11] J. Al-Khalili and E. Roeckl, *The Euroschool Lectures on Physics with Exotic Beams*, Lecture Notes in Physics No. v. 3 (Springer, 2008).

[12] E. Gadioli and I. Università degli studi (Milan, *Proceedings of the 11th International Conference on Nuclear Reaction Mechanisms: Varenna, June 12-16, 2006* (Universita degli studi di Milano, 2006).

[13] J. Dobaczewski, I. Hamamoto, W. Nazarewicz, and J. A. Sheikh, Phys. Rev. Lett. **72**, 981 (1994).

[14] Website, The EURISOL design study, http://www.eurisol.org/site02/index.php.

[15] T. Otsuka and A. Schwenk, Nuclear Physics News International **22**, 12 (2012).

[16] T. Otsuka *et al.*, Phys. Rev. Lett. **104**, 012501 (2010).

[17] T. Otsuka, T. Suzuki, R. Fujimoto, H. Grawe, and Y. Akaishi, Phys. Rev. Lett. **95**, 232502 (2005).

[18] T. Otsuka, M. Honma, and D. Abe, Nuclear Physics A **788**, 3 (2007).

[19] M. Honma, T. Otsuka, B. A. Brown, and T. Mizusaki, Phys. Rev. C **69**, 034335 (2004).

[20] T. Otsuka, T. Suzuki, J. D. Holt, A. Schwenk, and Y. Akaishi, Phys. Rev. Lett. **105**, 032501 (2010).

[21] G. Hagen, M. Hjorth-Jensen, G. R. Jansen, R. Machleidt, and T. Papenbrock, Phys. Rev. Lett. **109**, 032502 (2012).

[22] H. Grawe *et al.*, The European Physical Journal A - Hadrons and Nuclei **25**, 357 (2005).

[23] B. Brown, (2005).

[24] H. Grawe, Acta Physica Polonica B **34**, 2267–2275 (2003).

[25] H. Grawe and M. Lewitowicz, Nuclear Physics A **693**, 116 (2001).

[26] A. Gadea *et al.*, Eur. Phys. J. A **20**, 193 (2004).

[27] A. Stefanini *et al.*, Nuclear Physics A **701**, 217 (2002), 5th International Conference on Radioactive Nuclear Beams.

[28] E. Farnea and D. Bazzacco, Nuclear Physics News International **22**, 27 (2012).

[29] D. Scarpa *et al.*, EUROPEAN PHYSICAL JOURNAL A **47** (2011).

[30] Website, EURISOL design study, task 3: direct target, http://www.eurisol.org/site02/direct_target/.

[31] Website, The ISOLDE facility at CERN, http://isolde.web.cern.ch/isolde/.

[32] Website, ISAC Facilities for Rare-Isotope Beams, http://www.triumf.ca/research/research-facilities/isac-facilities-for-rare-isotope-beams.

[33] Website, HRIBF Facilities for Rare-Isotope Beams (ORNL), http://www.phy.ornl.gov/hribf/.

[34] Website, SPES - Selective Ions For Exotic Species, http://web.infn.it/spes/.

[35] Website, GANIL - SPIRAL II facility, http://www.ganil-spiral2.eu/.

[36] A. Andrighetto *et al.*, NUCLEAR PHYSICS A **834**, 754C (2010).

[37] T. Baumann, A. Amthor, D. Bazin, and B. A. Brown, Nature **449**, 1022 (2007).

[38] Website, GANIL - SPIRAL In Flight facility, http://www.ganil-spiral2.eu/science-us/accelerator/spiral.

[39] Website, The GSI Fragment Separator, http://www-wnt.gsi.de/frs/index.asp.

[40] Website, RIKEN NiSHiNa center for Accelerator-based science, http://www.nishina.riken.jp/Eng/.

[41] Website, NSCL A1900 fragment separator, http://www.nscl.msu.edu/tech/devices/a1900.

[42] Website, FRIB - Facility for Rare Isotope Beams, http://www.frib.msu.edu/.

[43] Website, FAIR - An International Facility for Antiproton and Ion Research, http://www.fair-center.eu/.

[44] Website, GSI Helmholtzzentrum für Schwerionenforschung, http://www.gsi.de/.

[45] http://ie.lbl.gov/systematics/chart2000g.pdf.

[46] B. Blank *et al.*, Phys. Rev. Lett. **84**, 1116 (2000).

[47] C. Dossat *et al.*, Phys. Rev. C **72**, 054315 (2005).

[48] C. Engelmann *et al.*, Zeitschrift für Physik A Hadrons and Nuclei **352**, 351 (1995).

[49] P. T. Hosmer *et al.*, Phys. Rev. Lett. **94**, 112501 (2005).

[50] T. Ohnishi *et al.*, Journal of the Physical Society of Japan **79**, 073201 (2010).

[51] O. Sorlin and M.-G. Porquet, Progress in Particle and Nuclear Physics **61**, 602 (2008).

[52] B. Pritychenko, J. Choquette, M. Horoi, B. Karamy, and B. Singh, Atomic Data and Nuclear Data Tables **98**, 798 (2012).

[53] O. Kenn *et al.*, Phys. Rev. C **63**, 064306 (2001).

[54] T. Ishii *et al.*, Phys. Rev. Lett. **84**, 39 (2000).

[55] H. Grawe, M. Górska, and J. Döring, AIP Conf. Proc. **561**, 287 (2000).

[56] A. Oros-Peusquens and P. Mantica, Nuclear Physics A **669**, 81 (2000).

[57] O. Sorlin *et al.*, Phys. Rev. Lett. **88**, 092501 (2002).

[58] M. Sawicka *et al.*, Phys. Rev. C **68**, 044304 (2003).

[59] K. Langanke, J. Terasaki, F. Nowacki, D. J. Dean, and W. Nazarewicz, Phys. Rev. C **67**, 044314 (2003).

[60] C. Mazzocchi *et al.*, Physics Letters B **622**, 45 (2005).

[61] O. Perru *et al.*, Phys. Rev. Lett. **96**, 232501 (2006).

[62] K. L. Yurkewicz *et al.*, Phys. Rev. C **70**, 054319 (2004).

[63] A. Bohr, R. Broglia, and S. italiana di fisica, *Elementary modes of excitation in nuclei:*Proceedings of the International School of Physics "Enrico Fermi" (North-Holland Pub. Co., 1977).

[64] R. Casten, *Nuclear Structure from a Simple Perspective*Oxford Studies in Nuclear Physics (Oxford University Press, 2000).

[65] G. Kraus *et al.*, Phys. Rev. Lett. **73**, 1773 (1994).

[66] T. Otsuka, M. Honma, and T. Mizusaki, Phys. Rev. Lett. **81**, 1588 (1998).

[67] N. Aoi *et al.*, Physics Letters B **692**, 302 (2010).

[68] S. Franchoo *et al.*, Phys. Rev. C **64**, 054308 (2001).

[69] W. Hamilton, *The Electromagnetic interaction in nuclear spectroscopy* (North-Holland, 1975).

[70] K. Krane and D. Halliday, *Introductory nuclear physics* (Wiley, 1987).

[71] R. Bass, *Nuclear Reactions with Heavy Ions*Texts and monographs in physics (Springer, 1980).

[72] J. Jackson, *Classical Electrodynamics* (Wiley, 1998).

[73] C. Bertulani, arXiv (2009), 0908.4307.

[74] K. Alder, A. Bohr, T. Huus, B. Mottelson, and A. Winther, Rev. Mod. Phys. **28**, 432 (1956).

[75] K. Alder and A. Winther, *Electromagnetic excitation: theory of Coulomb excitation with heavy ions* (North-Holland Pub. Co., 1975).

[76] A. Winther and K. Alder, Nuclear Physics A **319**, 518 (1979).

[77] C. Bertulani and G. Baur, Nuclear Physics A **442**, 739 (1985).

[78] C. A. Bertulani and G. Baur, Physics Reports **163**, 299 (1988).

[79] C. von Weizsacker, Z.Phys. **88**, 612 (1934).

[80] E. J. Williams, Phys. Rev. **45**, 729 (1934).

[81] B. Hoffmann and G. Baur, Phys. Rev. C **30**, 247 (1984).

[82] A. Goldberg, Nuclear Physics A **420**, 636 (1984).

[83] C. A. Bertulani and G. Baur, Phys. Rev. C **33**, 910 (1986).

[84] G. Baur, C. Bertulani, and H. Rebel, Nuclear Physics A **458**, 188 (1986).

[85] A. Aleixo and C. Bertulani, Nuclear Physics A **505**, 448 (1989).

[86] T. Glasmacher, Nuclear Physics A **693**, 90 (2001).

[87] C. Bertulani, Computer Physics Communications **116**, 345 (1999).

[88] W. Wilcke *et al.*, Atomic Data and Nuclear Data Tables **25**, 389 (1980).

[89] F. Delaunay and F. Nunes, J.Phys. **G34**, 2207 (2007), 0708.3007.

[90] J. M. Cook, T. Glasmacher, and A. Gade, Phys. Rev. C **73**, 024315 (2006).

[91] S. RAMAN, C. N. JR., and P. TIKKANEN, Atomic Data and Nuclear Data Tables **78**, 1 (2001).

[92] C. Bertulani, G. Cardella, M. D. Napoli, G. Raciti, and E. Rapisarda, Physics Letters B **650**, 233 (2007).

[93] H. Scheit, A. Gade, T. Glasmacher, and T. Motobayashi, Physics Letters B **659**, 515 (2008).

[94] C. Bertulani, C. Campbell, and T. Glasmacher, Computer Physics Communications **152**, 317 (2003).

[95] D. Weisshaar, Private communication .

[96] P. Závodszky *et al.*, Proceedings of Cyclotrons and Their Applications 2007, Eighteenth International Conference .

[97] L. Sun *et al.*, Proceedings of ECRIS2010, Grenoble, France .

[98] X. Wu, H. Blosser, D. Johnson, F. Marti, and R. York, Proceedings of the 1999 Particle Accelerator Conference, New York, 1999 .

[99] LISE++ computer code, http://lise.nscl.msu.edu/lise.html.

[100] K. Sümmerer and B. Blank, Phys. Rev. C **61**, 034607 (2000).

[101] A. Stolz *et al.*, Nuclear Instruments and Methods in Physics Research Section B: Beam Interactions with Materials and Atoms **241**, 858 (2005).

[102] D. Morrissey, B. Sherrill, M. Steiner, A. Stolz, and I. Wiedenhoever, Nuclear Instruments and Methods in Physics Research Section B: Beam Interactions with Materials and Atoms **204**, 90 (2003).

[103] B. Sherrill, D. Morrissey, J. N. Jr., and J. Winger, Nuclear Instruments and Methods in Physics Research Section B: Beam Interactions with Materials and Atoms **56–57, Part 2**, 1106 (1991).

[104] D. Bazin, J. Caggiano, B. Sherrill, J. Yurkon, and A. Zeller, Nuclear Instruments and Methods in Physics Research Section B: Beam Interactions with Materials and Atoms **204**, 629 (2003).

[105] S800 spectrograph inverse map server.

[106] D. Bazin, S800 service level destription, nscl internal document.

[107] J. Yurkon *et al.*, Nuclear Instruments and Methods in Physics Research Section A: Accelerators, Spectrometers, Detectors and Associated Equipment **422**, 291 (1999).

[108] M. Berz, K. Joh, J. A. Nolen, B. M. Sherrill, and A. F. Zeller, Phys. Rev. C **47**, 537 (1993).

[109] D. Weisshaar *et al.*, Nuclear Instruments and Methods in Physics Research Section A: Accelerators, Spectrometers, Detectors and Associated Equipment **624**, 615 (2010).

[110] S. Akkoyun *et al.*, Nuclear Instruments and Methods in Physics Research Section A: Accelerators, Spectrometers, Detectors and Associated Equipment **668**, 26 (2012).

[111] S. Paschalis *et al.*, Nuclear Instruments and Methods in Physics Research Section A: Accelerators, Spectrometers, Detectors and Associated Equipment , (2013).

[112] T. L. website, http://teledynelecroy.com/lrs/dsheets/4300b.htm.

[113] G. Knoll, *Radiation detection and measurement* (Wiley, 2000).

[114] W. Leo, *Techniques for Nuclear and Particle Physics Experiments: A How-To Approach* (Springer, 1994).

[115] S. Ahmed, *Physics and Engineering of Radiation Detection* (Elsevier Science, 2007).

[116] T. Baugher, to be published .

[117] R. Brun and F. Rademakers, Nuclear Instruments and Methods in Physics Research Section A: Accelerators, Spectrometers, Detectors and Associated Equipment **389**, 81 (1997).

[118] K. Wimmer, NSCL S800 ROOT data analysis software, http://www.nscl.msu.edu/~wimmer.

[119] K. Wimmer, NSCL S800 ROOT data analysis software user manual, http://www.nscl.msu.edu/~wimmer/manual/NSCL_ROOT_usermanual.pdf.

[120] S. Agostinelli *et al.*, Nuclear Instruments and Methods in Physics Research Section A: Accelerators, Spectrometers, Detectors and Associated Equipment **506**, 250 (2003).

[121] A. Estrade, *Time-Of-Flight Mass Measurements of Neutron Rich Isotopes at the NSCL.* (PhD thesis, 2010).

[122] L. Coraggio, Private communication .

[123] N. Shimizu *et al.*, Progress of Theoretical and Experimental Physics **2012** (2012).

Acknowledgments

The last three years have certainly been one the most intense period of my life. Having the possibility to complement the PhD school studies with an intense research activity at the Legnaro National Laboratory (INFN), gave me the opportunity to grow and learn in one of the most lively scientific frameworks that the Italian research can offer. For this I have to thank my supervisor, prof. Giovanna Montagnoli, who followed my PhD with care and interest and let me free to pursue my research curiosity. I also would like to thank my co-supervisor dr. Giacomo De Angelis, who is the "father" of the experiment presented in this thesis, for allowing me to work on this data analysis and for introducing me into the world of nuclear spectroscopy with useful teachings and suggestions.

A special thank to dr. Fabiana Gramegna that, apart from co-supervising this work, is my tutor in several activities since almost five years. She is the driving force of my scientific growth and I will never thank her enough for what she has been doing for me.

The experiment described in this work was performed at NSCL and it would have never been possible without the support of the local group. Among the others, I would like to thank prof. Alexandra Gade and dr. Dirk Weisshaar for the precious contribution to the experiment and for their suggestions during the data analysis and dr. Trevis Baugher who provided the simulation code. I'm really grateful to dr. Kathrin Wimmer for her continuous support during the data analysis and for

providing an important part of the code I used.
This thesis would not have been written without the priceless help of dr. Enrico Farnea. Thanks for your help in the difficult task of writing and finalizing the analysis and for being the fastest and most efficient proofreader that I've ever seen!

I'd like also to thank the people of the LNL-PD INFN gamma group for several fruitful discussions and suggestions for the analysis. Among the others dr. Caterina Michelagnoli, dr. Andrea Gottardo and dr. Jose Javier Valiente Dobon.
Since my three-year thesis in 2006 I've been part of the NUCL-EX collaboration and I was involved in several activities at LNL. It is impossible to summarize in few words the incredible amount of experiences, shifts, and the hard work we did together... I'll simply say a big THANK YOU! to everyone.

A special thank to Caterina and Enrico, good friends and the best uncles ever. We spent very good times together, very crazy times also... but this makes life more interesting!

Finally I would like to dedicate this work to Daniela and Benedetta: *whenever, wherever with you I feel at home.*